Schweizerische Eidgenossenschaft
Confédération suisse
Confederazione Svizzera
Confederaziun svizra

Eidgenössisches Departement des Innern EDI
Bundesamt für Meteorologie und Klimatologie MeteoSchweiz

Veröffentlichung MeteoSchweiz Nr. 88

Spatio-temporal homogeneity of a satellite-derived global radiation climatology

Rebekka Schibli

Veröffentlichung MeteoSchweiz Nr. 88

ISSN: 1422-1381

Spatio-temporal homogeneity of a satellite-derived global radiation climatology

Rebekka Schibli

Bitte zitieren Sie diese Veröffentlichung folgendermassen
Schibli, R: 2011, Spatio-temporal homogeneity of a satellite-derived global radiation climatology, *Veröffentlichungen der MeteoSchweiz*, **88**, 110 pp.

Herausgeber
Bundesamt für Meteorologie und Klimatologie, MeteoSchweiz, © 2011

MeteoSchweiz
Krähbühlstrasse 58
CH-8044 Zürich
T +41 44 256 91 11
www.meteoschweiz.ch

Weitere Standorte
CH-8058 Zürich-Flughafen
CH-6605 Locarno Monti
CH-1211 Genève 2
CH-1530 Payerne

Abstract

In this master thesis a climate data record of global radiation (SIS) generated by MeteoSwiss in the framework of the Satellite Application Facility on Climate Monitoring (CM SAF) is investigated. The climate data record was derived from measurements taken by the Meteosat First Generation (MFG) satellite series between 1983 and 2005.

A detailed knowledge of global radiation is important because the solar irradiation is the main source of energy driving life on Earth. Seasonal and interannual variations of global radiation for instance modulate the terrestrial hydrological cycle and the plant photosynthesis. Global radiation is an integral part of the earth's radiative balance and therefore it is one of the essential climate variables (ECV's) defined by the Global Climate Observing System (GCOS). In recent years the precise knowledge of its spatio-temporal variability became important in the field of solar energy power generation. Satellite data can provide information about the absolute amount of global radiation and its variability with a high temporal and spatial resolution generally unmet by ground-based measurement methods.

The thesis contains two parts. Firstly, homogeneity analyses of the climate data record are conducted. Secondly, the relation between global radiation and climate variability is investigated.

Homogeneity analyses are crucial for climate data records, because non-homogeneous data give wrong or poor information about the data series. In order to test the homogeneity of the data set, the Standard Normal Homogeneity Test (SNHT) is used. Especially over Africa, South America and in the high latitudes many breaks were found. In contrast, the data record seemed to be quite homogenous over the Atlantic, the Sahara and Europe. In addition to the SNHT, a new spatial homogeneity test that includes the information of adjacent pixels is developed. For this new test, the theory of multivariate Gaussian Markov Random Fields is used and a region instead of single pixels is tested. The spatial homogeneity test was more appropriate than the SNHT, because the influence of a break in a single pixel was reduced and the focus was laid on breaks that were significant over the whole region. It was decided to not homogenize the climate data record, because the breaks couldn't be traced back to known periods with satellite replacements which would be the most probable reason for breaks in such a climate data record. In addition, climate trends were calculated for corrected and uncorrected data. The analysis showed that the climate trends were only marginally affected.

In the second part, investigations about the relation of two large-scale climate variability phenomena, namely El Niño Southern Oscillation (ENSO) and North Atlantic Oscillation (NAO), with both, the global radiation and the cloud index (a surrogate for cloudiness) are conducted. The use of correlation analysis and ANOVA reveal clear patterns and significant correlations with global radiation and cloud index for all three oscillations. For ENSO, significant positive correlations with the global radiation were found in the northeast of Brazil and in southern Africa and negative correlations in the Atlantic between 20°N and 40°N and between 10°S and 30°S, in the southeast of Brazil, in North Africa and the Middle East. Opposite correlations were detected for the cloud index. During the positive phase of the NAO, global radiation was increased over southern Europe and over the Atlantic between 30°N and 40°N and decreased in parts of Ireland, in the north of Great Britain and in southern Scandinavia. The opposite was true during negative phases.

Most of the patterns and correlations found here corresponded to results from similar studies. Many studies have only investigated the relation of temperature and precipitation with the mentioned oscillations. Nevertheless, these studies helped to explain some of the patterns and relationships, because the cloud index is highly related to precipitation and global radiation correlates negatively with the cloud index.

Acknowledgement

I would like to express my gratitude to all those who supported me during the time of my master thesis and helped me to complete this thesis.

Special thanks go to my supervisors Reto Stöckli, Mark Liniger and Reinhard Furrer.

Firstly, my thank goes to Reto Stöckli. He always spent his time for me, presented me new thoughts and provided helpful support. I would also like to thank Mark Liniger whose comments and advices were very helpful. They further looked closely at the final version of this thesis, offered suggestions for improvement and Reto Stöckli corrected the English style and grammar. I would also like to express my gratitude to Professor Furrer for his guidance, explanations and suggestions for improvement. I have appreciated this support. It was a pleasure to work with them, many thanks.

Further thanks go to all colleagues from MeteoSwiss who supported me in this thesis. I want to thank them for all their help, interest and valuable hints. Especially, I have to thank Rebekka Posselt who has prepared the data for me.

I would also like to give my special thanks to my boyfriend Michael Merki who read through my text, gave me advice and always supported me during my master thesis.

Contents

Figures

Tables

1 Introduction

1.1 Context and motivation

In this master thesis a climate data record of global radiation derived from measurements taken on board the Meteosat First Generation (MFG) satellites from 1983 to 2005 is investigated. This data record has been generated by MeteoSwiss in the framework of the Satellite Application Facility on Climate Monitoring (CM SAF) which is part of the European Organization for the Exploitation of Meteorological Satellites (EUMETSAT).

Global radiation is the solar radiation reaching the earth's surface and includes the direct beam from the sun and the diffuse component (reflected or scattered radiation) (Glickman, 2000). The average daily solar radiation at the top of the atmosphere amounts to 342 W/m^2. This energy from the sun makes life possible on Earth (Hartmann, 1994). Long-term variations in solar radiation can affect amongst others the climate, the hydrological cycle or the plant photosynthesis (Pinker et al., 2005). In recent years, the amount and the long-term variability of solar radiation became important also with regard to solar energy projects. If precise knowledge of the amount of global radiation and cloudiness is available, a large part of thermal energy can be derived by solar energy. This is important in solar building architecture where a correct dimensioning of storage and regulation devices is essential to use as much solar energy as possible (Cano et al., 1986). But long-term radiation measurements are rare because of sparse or even absent ground stations, especially in regions that would be interesting for the construction of solar energy power plants (Lohmann et al., 2006). In these regions (for instance Africa) satellites can provide important additional information with high spatial and temporal resolution (Beyer et al., 1996). But also in other regions satellite data are crucial, because ground stations can only measure global radiation at single locations. Hence, climate analyses with satellite data are very useful in several application areas.

1.2 Purposes of the study

Analysis of climate data is more reliable when homogenized data sets are used. A data set is homogeneous when all the fluctuations contained in its time series reflect the actual variability and change of the climate. Most of the statistical methods assume that the investigated data are free from any non-meteorological or non-climatological errors. Changes in climatological data sets may either cause sudden shifts in the mean level or introduce gradual biases. In both cases, the time series become inhomogeneous. These inhomogeneities can affect the correct assessment of climatic trends (WMO, 2011). For these reasons, a first topic of this master thesis is to conduct homogeneity analyses. Until now, it is not known whether the CM SAF climate data record of global radiation is homogeneous or not and no thorough homogeneity analysis has been conducted (Posselt et al., 2011). Especially in regions where ground stations are rare or even absent, it is important to have a satellite data record that is correct and free of artificial inhomogeneities (Alexandersson, 1986). The type of inhomogeneity evaluated in this study are sudden shifts in the mean level in a time series compared to a reference series. Sudden shifts in the mean level are also called breaks in the following. The most probable reason for a break in a satellite-based climate data record are replacements of satellite sensors with resulting breaks covering the full measurement area.

The Standard Normal Homogeneity Test (SNHT) that tests the homogeneity over time for every pixel separately is used for a first approach. As we have a data set over time and space, this test might not be appropriate. Therefore, this thesis has the aim to develop a new test that includes both, the temporal as well as the spatial structure of the data set. Both tests, the SNHT and the new spatial homogeneity test,

are based on the likelihood ratio test that compares the likelihood of the null (no break) and alternative (one break) hypothesis and either rejects or accepts the null hypothesis. The homogeneity analysis is done over the time period from 1990 to 2005.

Next, different climate analyses will be conducted. In particular, the relation of global radiation (surface solar irradiance, SIS) and cloud index (CI) with two large-scale climate variability phenomena, namely El Niño Southern Oscillation (ENSO) and North Atlantic Oscillation (NAO), is investigated. This is done over the time period of MFG satellites from 1983 to 2005. Most previous studies that explored ENSO and NAO have focussed on the influence of these oscillations on precipitation and temperature but not on cloudiness or global radiation. Additionally, the present satellite data allow gap-free investigations of climate phenomena covering land and ocean. Therefore, our climate data record can complement previous studies, and it may be specifically useful to study the link between global radiation, cloud index and the mentioned oscillations over areas with sparse ground measurements such as the oceans.

Hence, the purposes of this master thesis can be summarized as follows:

- Conducting a homogeneity analysis with help of the Standard Normal Homogeneity Test (SNHT)
- Developing a new spatial homogeneity test that includes the information of spatially adjacent pixels
- Comparison of these two tests and eventual evaluation of the detected breaks
- Investigation of the relation between large-scale climate variability phenomena and global radiation (and cloud index) by use of the satellite-based climate data record

1.3 Research questions

As this thesis contains two parts separate research questions are defined for each part. Here, the research questions are quickly mentioned and a more detailed derivation can be found in the corresponding chapters.

The questions that correspond to the homogeneity analyses are:

- Is it possible to detect inhomogeneities in the climate data record for individual pixels?
- Is it possible to use the information of spatially adjacent pixels to create a homogeneity test that is more powerful than the SNHT?
- Is it justified to homogenize the CM SAF climate data record?

The questions that correspond to the climate analyses are:

- Is it possible to detect statistically significant climate-related patterns in the satellite-based climate data record by use of correlation analysis and analysis of variance between large-scale climate variability indices and SIS (or CI)?
- What are the physical explanations for the patterns revealed by above analysis and how coherent are these patterns to what was found in similar studies for temperature and precipitation?

1.4 Structure

Chapter 2 presents the data that is used in this study. Thereby, a more detailed overview of the Meteosat satellite series is given and the heliosat method which is employed to determine the global radiation at earth's surface from meteorological satellites is described. Further, the data sets used in this study are introduced. Chapter 3 and 4 analyze the homogeneity of the data set. In chapter 3, the Standard Normal Homogeneity Test is presented and applied to the satellite data record. In chapter 4 a new spatial homogeneity test is developed and used. It is furthermore compared to the original SNHT. Each of these two chapters begins with an overview and the restatement of the research questions followed by subsections with methods, results and discussion. Chapter 5 contains an analysis of the relations between known large-scale climate variability phenomena with global radiation and cloud index. Specifically, the widely used climatic teleconnection indices ENSO and NAO are investigated. The concluding chapter finally contains the most important findings as well as an outlook of possible future work in the field of homogeneity testing and the climate analysis.

2 Background and Data

2.1 Data retrieval

This section gives a short overview on the Meteosat satellites and describes the methodology for deriving global radiation from satellite sensors.

2.1.1 Meteosat First Generation satellites

Meteosat satellites fly in a geostationary orbit. They are positioned over the equator at 0° longitude at a height of 36'000 km above the earth's surface. Meteosat First Generation (MFG) refers to a series of 7 satellites (Meteosat 1-7) which provide data of the full Earth disc. The first Meteosat of the first generation was launched in 1977 and Meteosat 7 was launched in 1997. The main mission of MFG was to provide high resolution imagery of the Indian Ocean and surrounding areas and to support the weather forecast.

In order to assure a long term continuity of Meteosat, a specialized operational organization was founded, called EUMETSAT, and the Meteosat Operational Programme could be handed over to them. Prior to that the Meteosat programme was operated by the European Space Agency (ESA); in 1995 the control of the Meteosat satellites was passed to EUMETSAT.

The satellite has a length of 3.195 meters and a diameter of 2.1 meters. Its instruments are shown in Figure 2.1.

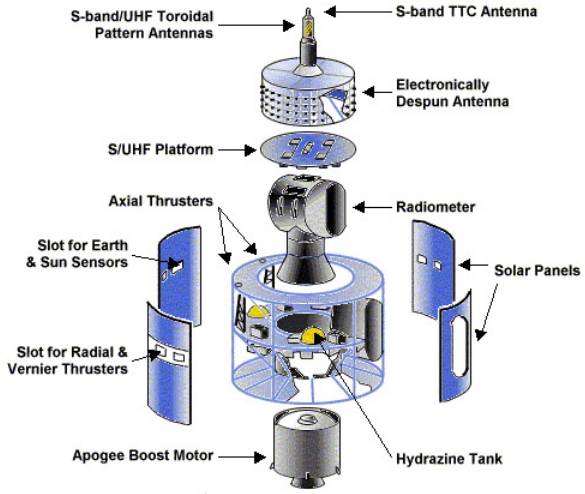

The most important instrument is the high resolution radiometer which allows continuous mapping of the Earth disc and has three spectral bands. The radiometer is also known as MVIRI, which stands for Meteosat Visible and Infrared Imager.

The visible band ranges from 0.45-1 µm and provides data for the visible spectrum during the day. The water vapor band (5.7-7.1 µm) can be used to determine the amount of water in the atmosphere. The thermal infrared band runs from 10.5-12.5 µm and can be used for thermal mapping during day and night.

Figure 2.1: Instruments of MFG (EUMETSAT, 2010)

The most important instrument is the Meteosat Visible and Infrared Imager (MVIRI).

The MVIRI provides a full scan of the earth disc every 30 minutes. Calibration information is needed in order to convert digital counts into radiances and temperatures (EUMETSAT, 2010).

The Meteosat series were replaced at the beginning of the 21th century. The first Meteosat of the Second Generation (MSG), Meteosat 8, was launched in 2002.

The MSG offers significantly enhanced products and services (Schmetz et al., 2002). It transmits more information at higher speed, which improved different applications for the user. Also, there are 12 spectral bands instead of only 3 and the spatial and temporal resolution is higher which provides more detailed maps and thus improved the weather forecast (EUMETSAT, 2010).

2.1.2 The heliosat method

Meteosat measures SIS indirectly through cloud cover information. SIS can be derived from the visible channel (VIS) by use of the Heliosat method (Beyer et al., 1996).

The heliosat method is a technique to determine the global radiation at ground level from meteorological satellites and was introduced by Cano et al. (1986). The method is based on the idea that the amount of cloud cover determines the top of the atmosphere reflectance, which is inversely related to the radiation incident on the surface. A surrogate for cloud cover, the so-called cloud index, is determined with the aid of the difference between the reflected radiation from the earth's surface and the clouds. This CI is in a second step used to estimate the incoming radiation at ground. The satellite measures the reflected radiation from the earth in the visible spectral range. The amount of this reflected radiation mainly depends on the cloudiness, but also on the incoming radiation at the surface. The incoming radiation is proportional to the irradiation intensity and thus depends on the sun elevation. With this knowledge a relative albedo can be calculated for all surfaces and clouds (Cano et al., 1986).

Usually, the albedo of the earth's surface or of the ocean is smaller than the albedo of clouds, except for snow and some desert soils. Because of this difference it is possible to determine the amount of cloudiness. With the aid of the cloud free and the cloudy albedo values a CI can be calculated. If ρ_c (relative albedo of complete cloudiness) and ρ_g (relative albedo of the unclouded ground) are known from previous measurements, and ρ is the actual relative albedo of a cloud pixel, then the CI can be calculated by the following formula:

$$n = (\rho - \rho_g)/(\rho_c - \rho_g)$$

The pixel value for ρ_c is derived by extracting the highest value of the albedo over a series of images; on the other hand the value for ρ_g is the minimum pixel value over the same time series. The time series should be long enough to get unclouded periods for each pixel and short enough to account for seasonal variations.

The CI ranges from 0 to 1 and can be interpreted as the percentage of cloud cover per pixel.

Over snowy areas this method doesn't work well, and an alternate CI would have to be calculated using the radiance in the thermal infrared band of the satellite.

In the analyzed data set a modified Heliosat method was applied. These modifications include both a self-calibration and a clear sky algorithm.

The original self-calibration algorithm has used the maximum normalized count ρ_c as parameter. Instead of using the maximum value for the determination of ρ_c, the modification uses the 95% percentile.

The clear sky algorithm is used to calculate ρ_g. Instead of using a monthly field of the clear sky counts, a mean over seven days is used. Thus, rapid changes in the albedo of the ground can be captured and represented and unrealistic steps between different months can be avoided (Posselt et al., 2011). With this CI it is now possible to determine the ground irradiance. The heliosat method is based on the assumption that there is a linear relationship between the CI and the atmospheric transmission. The atmospheric transmission is the ratio of global irradiance at ground (G) and extra-terrestrial irradiance (G_{ext}) and measured by the clearness index $k = G/G_{ext}$. The linear model is:

$$k = a \cdot n + b$$

The clearness index k is measured at ground from sampled stations. The CI is derived with the above-described method. A linear model is fitted to these data and the parameters a and b are determined. In

general the correlation coefficient is greater than 0.8 which demonstrates that satellite data can be used for mapping the global radiation at ground level (Cano et al., 1986).

2.2 Data sets

The next four sections describe the data sets used in this thesis, namely the CM SAF climate data record (CDR), the ECMWF Re-Analyses data set and data from the Global Precipitation Climatology Project (GPCP). For the homogeneity analyses, SIS from the CM SAF climate data record is tested against reference series from the Re-Analysis data set (ERA Interim) and ANETZ stations. In the climate analyses, SIS and CI from the CM SAF CDR, temperature from the ECMWF Re- Analyses data sets and precipitation from the GPCP data set is investigated. The last section of this chapter describes why and how the data are deseasonalized.

2.2.1 CM SAF climate data record

The Satellite Application Facility on Climate Monitoring (CM SAF) has recently generated a 23 year long (1983-2005) climate data record (CDR) of SIS, direct irradiance (SID) and effective cloud albedo (n) over Europe and Africa from the geostationary Meteosat First Generation Satellites (EUMETSAT, 2010). For the generation of the climate data record, Meteosat 2-7 were used (Posselt et al., 2011a, Posselt et al., 2011b). The operational periods for these satellites are listed in Table 2.1.

Satellite	from	To
Meteosat 2	16.08.1981	11.08.1988
Meteosat 3	11.08.1988	19.06.1989
Meteosat 4	19.06.1989	24.01.1990
Meteosat 3	24.01.1990	19.04.1990
Meteosat 4	19.04.1990	04.02.1994
Meteosat 5	04.02.1994	13.02.1997
Meteosat 6	13.02.1997	03.06.1998
Meteosat 7	03.06.1998	31.12.2005

Table 2.1: Operational periods for the Meteosat satellites (Posselt et al., 2011)

The exact dates of the satellite replacements are indicated. Usually, when a new satellite was employed, the one before was still in use. Thus, if a satellite encountered any problems or disruptions, the one before could be used as alternate. That's why Meteosat 3 and 4 appear twice.

MFG data has a high spatial (2.5 km for the visible and 5 km for the other channels) and temporal resolution (30 min) and the visible disc ranges from 80° N to 80° S and from 80° E to 80° W (Schmetz et al., 2002). For all analyses monthly means, a spatial resolution of 1°×1° and a geographical range from 70°N to 70°S and from 70°W to 70°E was used. Since the pixel size of the original data set was 0.1×0.1°, a weighted mean for every 1°×1° pixel according to the latitude was calculated. To be more precise, each pixel was weighted with the cosine of its latitude, and then all pixel values were summed up and divided by the sum of all weights for the considered pixel region.

2.2.2 ECMWF Re-Analyses data sets

The two ECMWF Re-Analyses data sets, ERA-40 (Uppala et al., 2005) and ERA-Interim (Dee et al., 2011) were used. Both data sets were interpolated to a spatial resolution of 1°×1° and the same geographical range as for the CM SAF CDR was taken. ERA-Interim only covers the period from

1989 to present. Therefore, ERA-40 data had to be used between 1983 and 1988. To account for the slight shift between the two datasets, a mean bias of their overlapping time period (between 1990 and 2001) was calculated in order to calibrate the ERA-40 data set towards the ERA-Interim data set. However, as reference series for the homogeneity analyses only the ERA-Interim data set was taken in order to diminish any impact that could make the reference series inhomogeneous. For the climate analyses, the ERA-Interim as well as the calibrated ERA-40 data set was used, because slight inhomogeneities don't smear climatological effects.

2.2.3 Global Precipitation Climatology Project

Precipitation data was derived from the Global Precipitation Climatology Project (GPCP). This data is globally complete and available at 2.5° latitude × 2.5° longitude resolution from January 1979 to present. The data was regridded in order to have it available on a 1°×1° resolution. Again, the same geographical range as in the two above described data sets was used. GPCP is a merged data set and includes precipitation estimates from microwave data from polar orbiting satellites, infrared data from geostationary satellites and surface rain gauge observations (Adler et al., 2003). The data used here is specified in mm/h (averaged over a month).

2.2.4 ANETZ

In Switzerland, global radiation measurements from 56 different ANETZ stations could be used as reference for the SNHT. The ANETZ has been renewed in the past few years and is now called SwissMetNet. The stations are distributed quite regularly over Switzerland and are available during the whole time period between 1983 and 2005. The time series of global radiation from all stations have been used as-is, since they were corrected and homogenized by MeteoSwiss (by use of a complementary method to the SNHT). The correction included the adjustment of the calibration level for each individual station (Moesch and Zelenka, 2004). In the work of Moesch and Zelenka (2004) the time series of each station was compared to the time series of at least three spatially adjacent stations. For each region within Switzerland the most homogenous stations were identified with the aid of several criteria (no entries in station history indicating measurement problems, no replacement of station location, no sensor change, etc.). Then, difference series for every month between two stations were calculated, summed up and plotted. One of the two time series was not homogenous if the slope of the accumulated differences showed a change. With 3 comparative time series and the prior knowledge of homogenous stations, it was possible to identify the erroneous stations. In Figure 2.2 for instance, Station 1 showed a change in the slope for the years 1992 and 1997 with respect to Stations 2, 3, and 4.

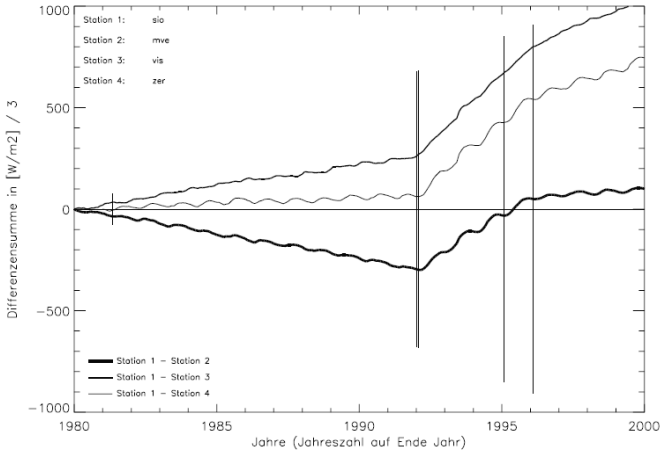

Figure 2.2: Accumulated difference series.

Vertical lines show the points in times of the change of the slope.

At points in time where all three accumulated difference series showed a change in the slope, a break was set and the corresponding time series was corrected.

2.2.5 Deseasonalization

In the homogeneity as well as in the climate analyses, deseasonalized values were used. The advantage of deseasonalization is that the annual cycle is masked in order to evaluate the climatological anomaly of each month. The deseasonalization is different for additive (CI and temperature) and multiplicative (SIS and precipitation) variables. This was done according to standards defined by WMO (2011). For additive variables, each monthly value was subtracted by the long-term mean of the corresponding month while for multiplicative variables the monthly mean was divided by the long term mean. $\overline{Y}$ is the mean value of each month over the time period and Y_i are the monthly values.

Hence, the deseasonalization for additive variables is: $Y_i - \overline{Y}$,

and for multiplicative variables: $\frac{Y_i}{\overline{Y}}$.

3 Homogeneity of selected pixels

3.1 Overview and research question

In order to use data from satellites for climate studies, they must be free from any non-climatological and non-meteorological errors. Data therefore have to be free from artificial breaks or temporal trends. Non-homogenous data series give poor or wrong information about the climate and further statistical analyses may not be meaningful (Posselt et al., 2011, Alexandersson, 1986). As mentioned earlier, inhomogeneities might affect the correct assessment of climatic trends (WMO, 2011). According to Moberg and Alexandersson (1997) homogenous time series are rare and the non-homogeneities can be abrupt (due to relocations or changes of instruments) or gradual (constant decrease of instruments). In the case of our climate data record the most probable reasons for breaks are replacements of the satellites (Posselt et al., 2011).

Although the CM SAF climate data record has been validated in order to guarantee that it fulfills the previously defined accuracy requirements, a thorough homogeneity analysis has not yet been conducted (Posselt et al., 2011). Hence, the topic of this chapter is the investigation of the satellite data record with regard to inhomogeneities. Thereby, the Standard Normal Homogeneity Test (SNHT) developed by Alexandersson (1986) is applied for Switzerland (over the time period from 1983 to 2005) and the whole visible disc of Meteosat (over the time period from 1990 to 2005). The reason for the shorter time period for the whole visible disc is that as reference series the ERA Interim data set was used that was only available as of 1990.

The research question that is treated in this chapter is:

- Is it possible to detect inhomogeneities in the climate data record for individual pixels?

As the SNHT searches for breaks in a time series, the SNHT is applied for each pixel separately.

3.2 Methods

3.2.1 Standard Normal Homogeneity Test

The SNHT was originally developed for precipitation and temperature data. The same procedure of the homogeneity test can however be applied to the global radiation data of this study.

An advantage of the SNHT is that it gives information on the most probable break and its magnitude. Many other homogeneity tests don't provide this information (Alexandersson, 1986). Peterson and Easterling (1994) compared different homogeneity tests and stated that the SNHT and another closely related test called bivariate test 'were by far the best tests for revealing and dating single and sudden shifts in artificial data'.

The following explanations are based on Alexandersson (1983). The SNHT uses a test series (Y_i), here the SIS from the satellite record, and compares it to one or more reference series (X_i). This ensures that only true breaks and not breaks that are due to climatic changes are found. Therefore it is important that homogenous reference series are available. Usually, the spatially closest stations are used as reference because their time series are highly correlated with the ones of the test series. If more than one reference stations are included, a weighted mean of the reference stations is used, and the weights are according to the correlation coefficients between the test series and the single reference series:

$$X_i^* = \frac{\sum_{j=1}^{k} X_{i,j}\rho_j^2}{\sum_{j=1}^{k} \rho_j^2}$$

$X_{i,j}$ is then the reference station j at time i and ρ_j the correlation coefficient of the successive differences between the reference station j and the test pixel.

After weighting, the test as well as the reference series are deseasonalized as described in Section 2.2.5. As we use SIS, the deseasonalization is based on ratios. Then, the ratio of the deseasonalized test and reference series is calculated. This ratio is known as Q_i -Series and fluctuates around one.

$Q_i = \frac{Y_i / \overline{Y}}{X_i / \overline{X}}$, if only one reference station is used and

$$Q_i = \frac{Y_i / \overline{Y}}{\left(\frac{\sum_{j=1}^{k} (X_{i,j} / \overline{X}_j)\rho_j^2}{\sum_{j=1}^{k} \rho_j^2} \right)}$$, if several reference stations are used.

X again denotes the reference series and Y the test series.

For the SNHT, this Q-Series are in a further step standardized according to:

$$Z_i = \frac{(Q_i - \overline{Q})}{\sigma_Q}$$

This Z_i -series has a mean value of 0 and a standard deviation of 1. Now the null hypothesis of no break and the alternative hypothesis of one break can be formulated:

$$H_0 : Z_i \in \mathrm{N}(0,1), i \in \{1,...,n\}$$

$$H_1 : \begin{cases} \text{for some } 1 \le a < n \text{ and } \mu_1 \ne \mu_2 : \\ Z_i \in \mathrm{N}(\mu_1,1), i \in \{1,...,a\} \\ Z_i \in \mathrm{N}(\mu_2,1), i \in \{a+1,...,n\} \end{cases}$$

Thus, a break is a significant shift in the mean level within a time series. By forming a likelihood ratio a test quantity can be derived. The likelihood ratio is the ratio of the probability that H_1 is true to the probability that H_0 is true. The likelihood function of H_1 is $(2\pi)^{-n/2} e^{-1/2(\sum_{i=1}^{a}(z_i-\mu_1)^2+\sum_{i=a+1}^{n}(z_i-\mu_2)^2)}$ and of H_0 is $(2\pi)^{-n/2} e^{-1/2\sum_{a=1}^{n} z_i^2}$ and thus the ratio to maximize is:

$$\underset{\mu_1,\mu_2,a}{Max} \frac{(2\pi)^{-n/2} e^{-1/2(\sum_{i=1}^{a}(z_i-\mu_1)^2+\sum_{i=a+1}^{n}(z_i-\mu_2)^2)}}{(2\pi)^{-n/2} e^{-1/2(\sum_{a=1}^{n} z_i^2)}} > C$$

By calculating the log of this ratio with $\mu_1 = \overline{z_1}$ and $\mu_2 = \overline{z_2}$ where

$\overline{z_1} = \frac{1}{a}\sum_{i=1}^{a} z_i$ and $\overline{z_2} = \frac{1}{n-a}\sum_{i=a+1}^{n} z_i$

gives

$$T_0 = \max_{1\le a<n}\{T_a\} = \max_{1\le a<n}\left[a\overline{z_1}^2 + (n-a)\overline{z_2}^2\right]$$

$\overline{z_1}$ and $\overline{z_2}$ are the arithmetic means before and after the break and a is the month and year of a break. For every a (for every month in every year) T_a is calculated and the a with highest T_a is the month and year of the most probable break. If T_a *max* exceeds a certain critical value, then the break is significant and the null hypothesis of no break can be rejected (Alexandersson, 1986). In the following, T_a with a=1,…,n is denoted as T-Series.

The 95% significance levels for 200 <n ≤ 300 are listed in the Appendix 9.1.

The test can be expanded for many breaks. Subsequently the series before and after the break are investigated. Exactly the same test is used for these two smaller time series. This procedure is repeated until no significant break is found anymore.

The SNHT answers the question, whether and at what time a possible break occurs, how certain it is and how much the mean level before and after the break has changed. Idealized Q- and T-Series are illustrated in Figure 3.1. It is well visible from these figures, that the test assigns the break to the month with the maximal T-value.

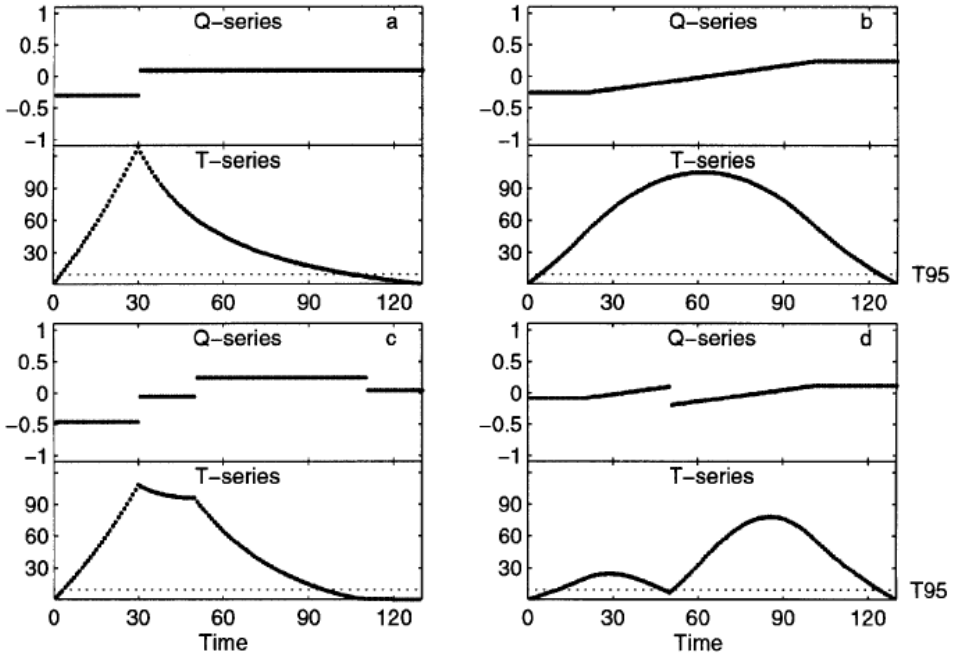

Figure 3.1: Idealized Q- and T-Series (Moberg and Alexandersson, 1997)

The 95% significance levels are indicated by the dotted lines.
a) single break, b) a trend, c) three different break, d) a trend interrupted by a single break.

An important disadvantage of the SNHT is that it tends to find breaks more easily at the beginning and the end of the time series (Alexandersson, 1984). Many studies have been conducted on this topic, see for instance Toretti et al. (2011) or Ducré-Robitaille (2003). All of them concluded that the false break detection increases at the beginning or at the end of the time series.

3.2.2 Accuracy of the SNHT

In order to test the accuracy of the SNHT, artificial time series with similar correlation structure, mean and standard deviation as one representative original time series which contained a significant break were generated. The original series was taken from one pixel over Switzerland where the SNHT was already applied and thus the height of the break was known. Therefore, 100 AR(2)-models were simulated and a break of the same height and at the same point in time as the original one was inserted. The AR(2) model is: $X_t-\mu=\alpha_1(X_{t-1}-\mu)+\alpha_2(X_{t-2}-\mu)+E_t$ with the assumptions $E_t=N(0, \sigma^2)$. $\hat{\sigma}^2$ was 0.018. The SNHT detected 18 breaks at the exactly correct location, the standard deviation amounted 33.81 month or 2.8 years (see Figure 3.2). With the significance level of 95% and 100 simulation 5 wrongly detected breaks are expected (null hypothesis is being rejected although it is true) which explains the breaks at the beginning of the time series.

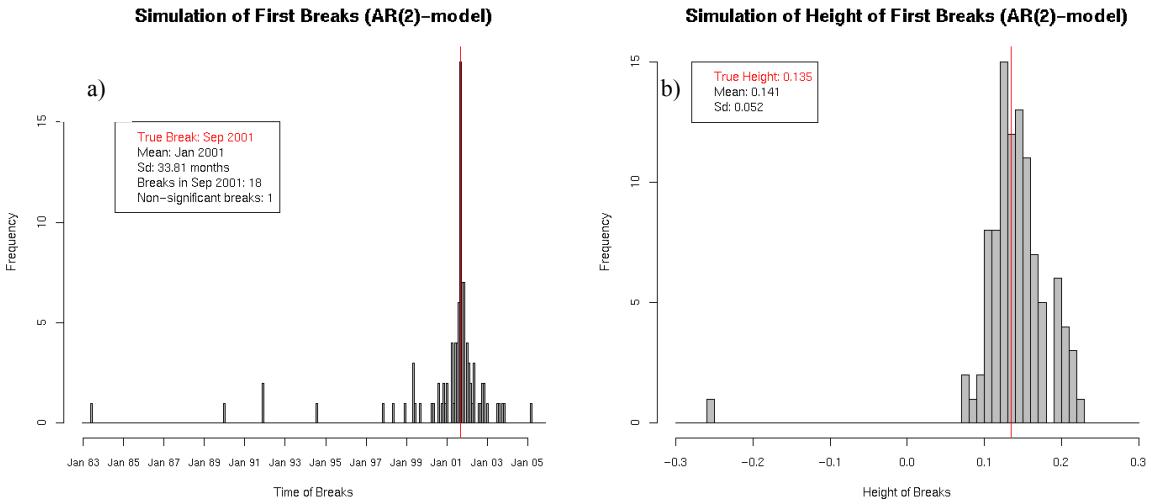

Figure 3.2: Simulation of First Breaks

a) Distribution of months of the first breaks from the simulated data.
b) Distribution of heights of the first breaks from the simulated data.
The red lines correspond to the true month and height of the break, respectively. On the y-axis the absolute counts of the 100 simulations per month or per height of break of 0.01 are displayed.

Figure 3.2 gives a good idea about the accuracy of the test and about the time spread of a break. The heights of the breaks were fairly well estimated, there was in this example only one break with a false direction, probably belonging to a wrongly detected break.

This first experiment with the SNHT shows that the test detected breaks in the correct time period, but that a spread of several months has to be included with the given height of the breaks. Of course, if the break was higher, the error of the test would be much smaller, e.g. with a double height of the breaks, the distribution was much narrower and the standard deviation only about 3 months.

The conclusion of this paragraph is that the test works correctly but we shouldn't identify breaks on a monthly scale, but rather summarize clustered breaks in similar months to one single break.

3.2.3 SNHT for CM SAF satellite data

This section describes how the SNHT was applied to the CM SAF climate data record. The test series were the individual pixels (with 1°×1° spatial resolution) of the CM SAF CDR about SIS over the 23 years or the 276 months of the time period from January 1983 to December 2005. Reference series were on the one hand the 56 ANETZ stations (over Switzerland only), in the following simply called ground stations. For the reference series, two different combinations were used: the closest station and

a weighted mean of the 5 closest stations. On the other hand, the ERA-Interim data set available since 1990 was used. The SNHT was applied to every pixel separately and in every pixel the most probable break was determined. The T-Series were also plotted, as they gave a better overview of the magnitude and uncertainty of the break. For instance, it was visible whether the T-Series reached a clear maximum at a single point in time or whether it rose and declined steadily.

Because the most probable break tends to occur near the beginning or the end of a time series, breaks in the first and last 10 months were not considered as suggested by Moberg and Alexandersson (1997).

3.3 Results

3.3.1 Homogeneity test over Switzerland

Three different reference series were used in order to evaluate the homogeneity of the data over Switzerland. Figure 3.3 shows all breaks that were found with ERA-Interim as reference (a), and breaks at similar points in time (within 2 years) that were found with ground stations as reference (b and c). In Figure 3.3 b) the result with one ground station as reference and at the right the result with 5 ground stations as reference can be seen. With ERA-Interim as reference, four significant pixels were detected while with ground stations as reference much more pixels with breaks were found and also multiple breaks per pixels occurred often.

In Figure 3.3 d) the two pixels that had the same break points for all three reference series are shown. This was in September 2001.

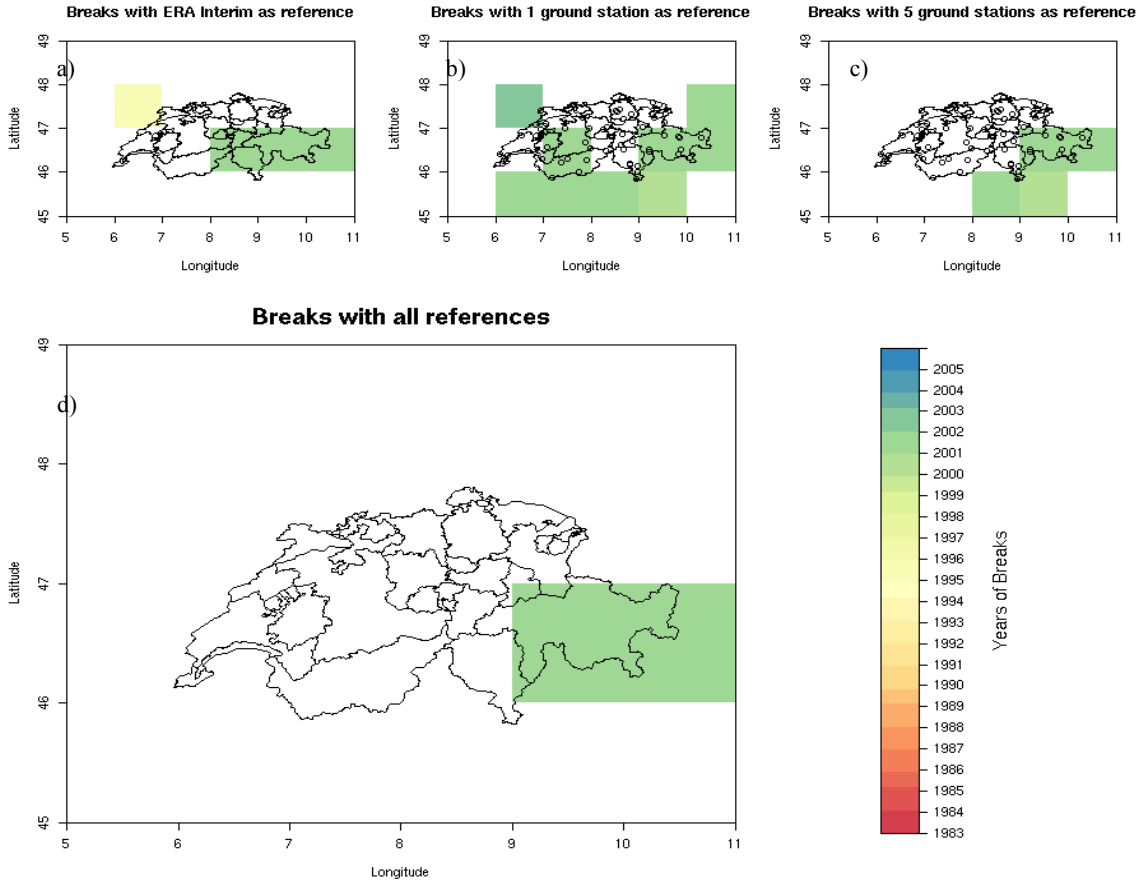

Figure 3.3: Breakpoints over Switzerland

a) All pixels with significant breaks and ERA-Interim as reference. b, c) All pixels with a break at similar points in time as in the Figure a) and with one or five ground stations, respectively. d) Pixels with same break point for all three reference series.

In the following, the characteristics of these breaks are presented in more detail. First, the T-Series for each pixel individually are shown in Figure 3.4. As the results of the SNHT with one and with five ground stations as reference are quite similar, in the following only the results from the test with one ground station and with ERA-Interim as reference are compared. In Figure 3.4 a) the T-Series with one ground station as reference are plotted. For no pixel a break was detected until 1987. Most of the pixels had a break between 1993 and 2002 approximately.

The four significant pixels with the reference ERA-Interim are well detectable in Figure 3.4 b). The one in 1995 is only just above the significance level, whereas the other three in September 2001 are of higher magnitude. As ERA-Interim was used from 1990 only the time period between 1990 and 2005 is covered.

Both plots show more or less the same course: few inhomogeneities at the beginning of the time period and a maximum around 1998 until 2002. Nevertheless, there was no clear peak, especially for the SNHT with the ground stations as reference.

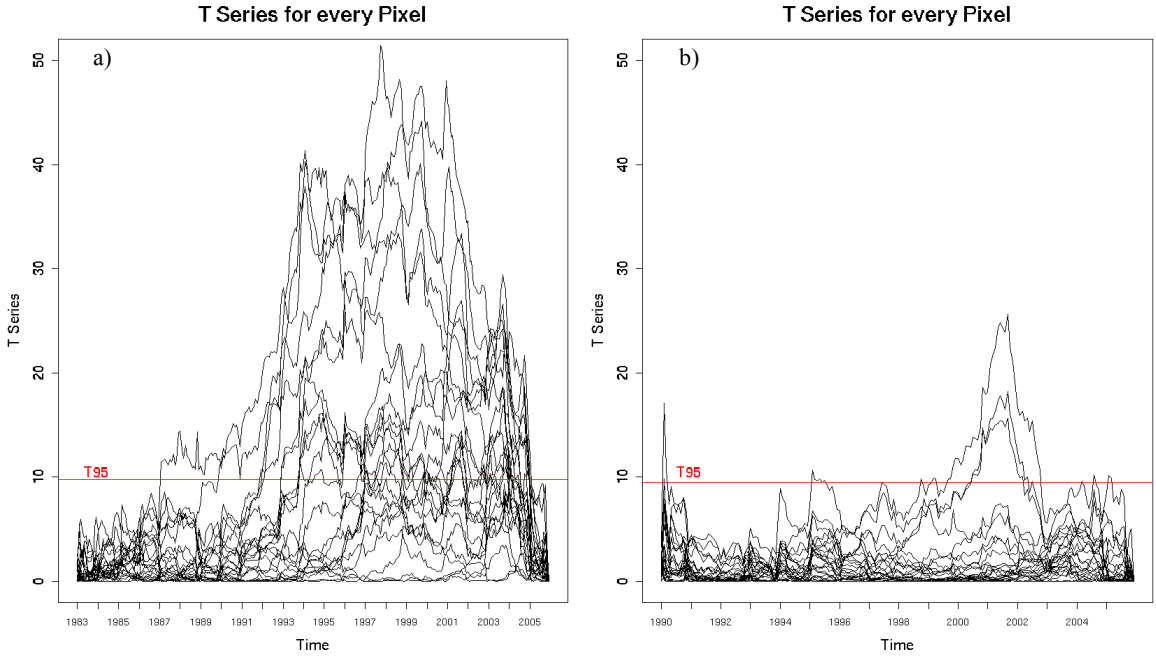

Figure 3.4: T Series of SNHT

a) One ground station as reference.
b) ERA-Interim as reference.
The red lines represent the critical T-value (on the 95% level).

In Figure 3.5 a more detailed overview of the detected breakpoints with one reference ground station is given. Many pixels had more than one significant break. In several pixels, more than half of the T-values were significant. Even for adjacent pixels the points in time of the breaks differed to some extent strongly.

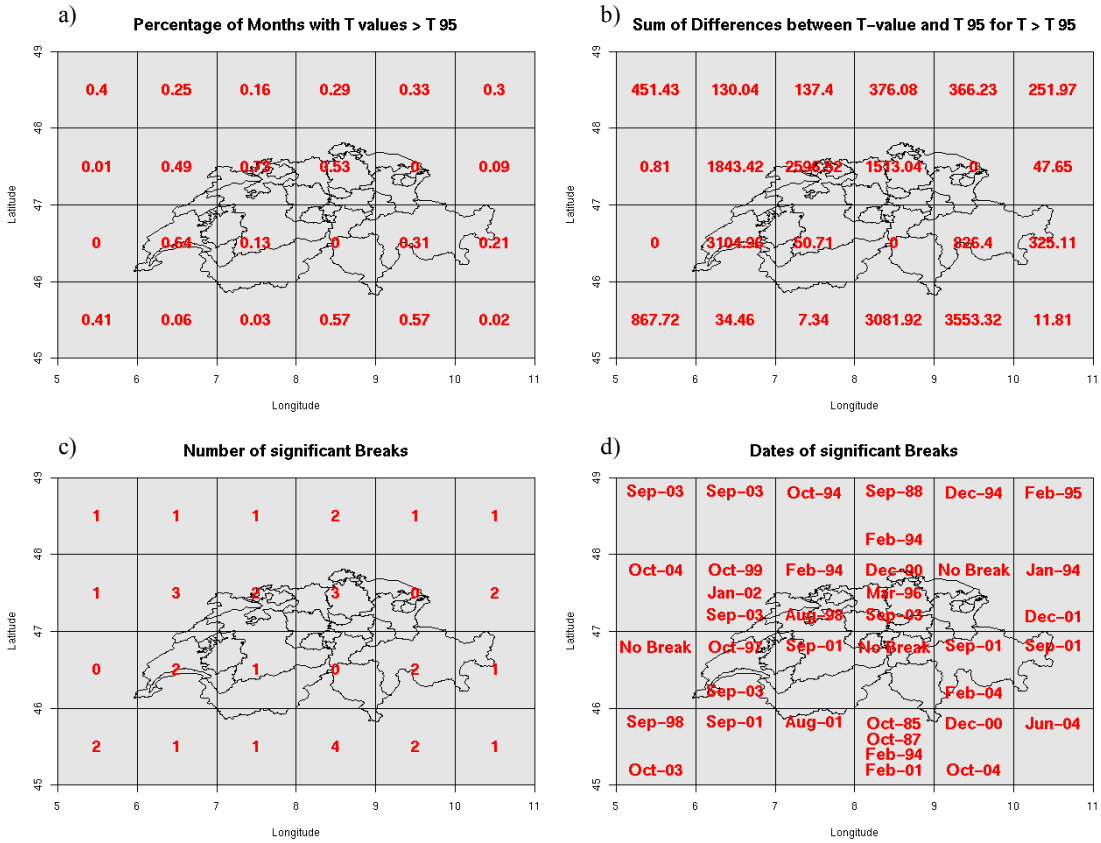

Figure 3.5: Detailed analysis of breaks over Switzerland with one ground station as reference

a) Proportion of months that had a T-value larger than the critical T-value.
b) Sum of the differences between the actual and the critical T-value for all significant T-values.
c) Number of significant breaks.
d) Dates of significant breaks.

The same analyses were done with ERA-Interim as reference and are shown in Figure 3.6. A much more homogenous image of the breakpoints was visible. As seen above, only four pixels had a break and none of them had more than one significant break. Three of them occurred in exactly the same month.

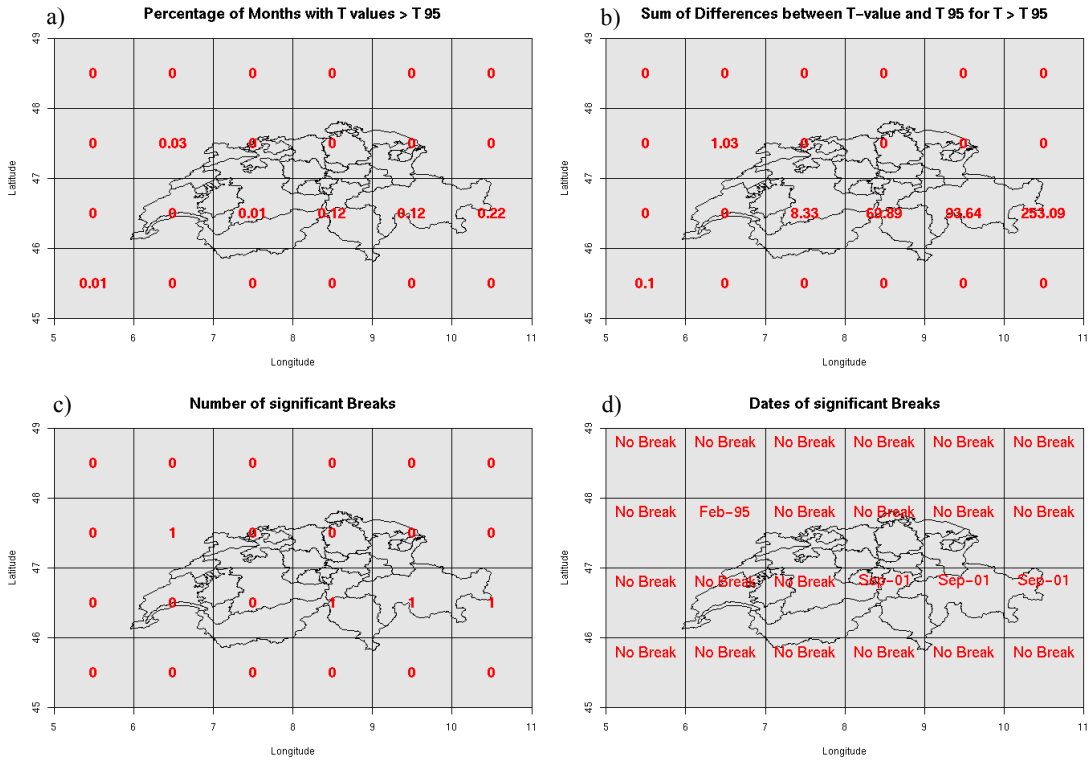

Figure 3.6: Detailed analysis of break over Switzerland with ERA-Interim as reference

a) Proportion of months that had a T value larger than the critical T value.
b) Sum of the differences between the actual and the critical T value for all significant T values.
c) Number of significant breaks.
d) Date of significant breaks.

In summary, no clear pattern of the breaks was detected. Neither could the breaks be allocated to satellite replacements. There were only two pixels for which homogenous time series could be assumed. The other pixels showed up to 4 breaks.

Thus, no consistent result with the three different reference series was found. The ERA-Interim time series seem to be much more similar to the satellite time series as the ground stations. Nevertheless, for two pixels, with all three reference series the same break was detected.

3.3.2 Homogeneity test over the whole visible disc

In a next step, the SNHT was applied on the whole visible disc of Meteosat. Because of the lack of the integral and homogenous spatial coverage of worldwide ground stations, only ERA-Interim was used as reference.

The result of the SNHT over the whole visible disc is shown in Figure 3.7. Many different breaks were found; presented is only the most significant break for each pixel. The single pixels had partly up to 6 significant breaks. In general, over oceans, the time series were more homogenous than over continents. Over Africa, most breaks were found around 1997. In contrast, in large parts of the Sahara, no break was detected. The same was true for Europe. Single breaks were found in France and Switzerland. A quite inhomogeneous image occurred in South America and in the subtropical South Atlantic. Also in high latitudes, many breaks were detected.

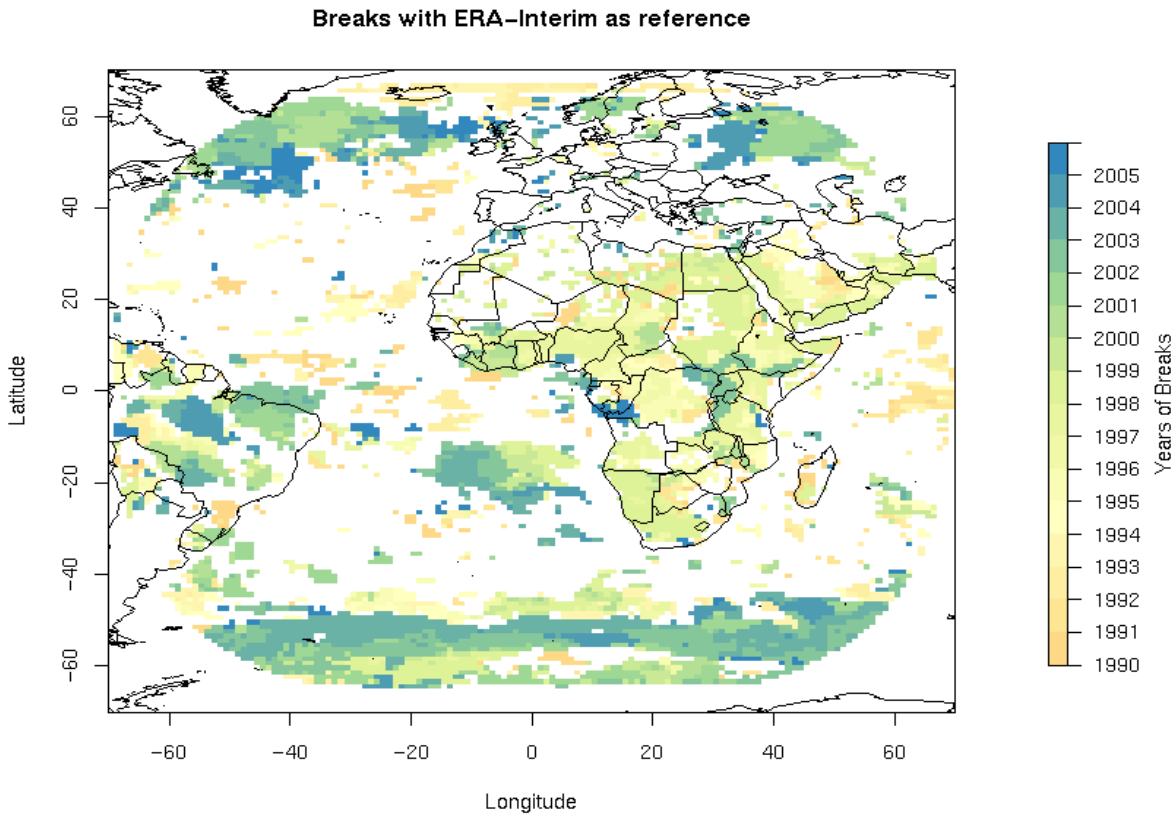

Figure 3.7: Most significant break point for each pixel over the whole visible disc of Meteosat

For each pixel the point in time of the most significant break is shown. In white pixels no break occurred.

3.4 Discussion

The question that was investigated in this chapter was whether it is possible to detect temporal inhomogeneities for individual pixels of a spatio-temporal climate data record. Therefore, the SNHT was applied over Switzerland and over the whole visible disc of Meteosat. Different references series were included in the analyses. Over the whole disc only ERA-Interim was available because of the lack of reliable reference series.

The SNHT detected breaks that could be justified when the corresponding T-Series were examined. For many pixels, multiple breaks were detected. This is not simply a feature of our satellite-based climate data record. For instance, Heino (1994) stated that long time series without artificial changes are rare. Also Moberg and Alexandersson (1997) found very large inhomogeneities when they investigated grid box temperature series in Sweden. Additionally, WMO (2011) pointed out that meteorological or climatological data are generally not homogenous and free from errors.

It must also be considered that the breaks can occur due to inhomogeneous reference series. The ERA-Interim data set as well as the ground stations could contain breaks. For instance, as mentioned in section 2.2.4, for ground stations the change in the slope of the difference series was used as a criterion for the correction of inhomogeneous data series. When testing single ground stations against each other with the SNHT (one as reference and one as test series), still several breaks were found. Additionally, if a certain station had a change in the slope with only one adjacent station and not with all three stations simultaneously, no correction was made. This is another reason, why the SNHT found breaks between two close-by ground stations. Therefore it is not surprising that the SNHT also found many breaks by comparing the satellite data record to ground stations. Some of them may be due to still existing inhomogeneities (when the criterion of the SNHT is used) of the ground stations.

However, the data that comes from ground stations is certainly more reliable than the data that comes from a remote and unattended instrument located 36’000 km out in space.

Breaks at very high latitudes are less problematic and can be explained, because the satellite has at these locations difficulties to scan the Earth correctly. This is on the one hand due to the skewed view of the satellite to the surface and on the other hand the high incidence angle of solar irradiation at high latitudes.

The aim was to find area-wide break points that can occur at periods of satellite replacements. However, the application of the SNHT over both Switzerland and over the full disc demonstrates that breaks occur with a complex spatio-temporal pattern that cannot be used for a generalized homogenization exercise over the full area in question. Therefore, a new test that allows to search for break points occurring consistently over a whole region is presented in the next chapter.

4 Spatial Homogeneity Test

4.1 Overview and research questions

The previous section described and applied an approach for the detection of breaks in a climatological time series. This test searched for breaks of individual pixels without including the information of adjacent pixels. However, the correlation structure of space and time is important and should thus be included in such a break point test.

In this section, a spatial test is presented where each pixel is conditionally dependent on its spatially adjacent pixels. Instead of testing a single pixel the break of an entire region is evaluated. The spatial homogeneity test is searching for one coherent break in a region. Therefore, the likelihood of H_0 (no break) and of H_1 (one break at a certain point in time) are compared with help of the likelihood ratio test statistic. It is then decided whether H_0 can or cannot be rejected. The ratio between the deseasonalized test and reference series (also called Q-Series) is used. The spatial test further employs the theory of Gaussian Markov Random Fields (GMRF) and its algorithm can be summarized by the following steps:

1. Formulation of H_0 and H_1 and definition of the mean vector and precision matrix of the pixels of a region
2. Searching for the best set of parameters for a certain region under H_0 and H_1. This is done by use of the maximum likelihood estimation method.
3. Calculation of the likelihood with the best set of parameters under H_0 and H_1
4. Decision whether H_0 should or shouldn't be rejected by use of the likelihood ratio test

The likelihood of H_1 can be determined for every time index and compared to the likelihood of H_0. Hence, the likelihood ratio statistic can be determined for every point in time and it is predicable at what point in time H_0 is most likely rejected.

Research questions

Here, the research questions of this chapter are quickly resumed. The results of the SNHT showed a very inconsistent image of breaks. Often, adjacent pixels had different points in time for the breaks. Therefore, a new homogeneity test, which includes the information of spatially adjacent pixels, is presented here. The focus in this chapter is laid on the following two research questions:

- Is it possible to use the information of spatially adjacent pixels to create a homogeneity test that is more powerful than the SNHT?
- Is it justified to homogenize the CM SAF climate data record?

The remaining chapter is organized in a methods, results and discussion part. The first section of the methods part describes the theory of Gaussian Markov Random Fields (GMRF), which is used for the definition of the mean vector and the precision matrix. In a next step, the mean vector and precision matrix for our specific climate data record are defined and then the model and model assumptions are presented. Thereafter, the maximum likelihood estimation and the function optim() in R as well as the

procedure of the likelihood ratio test are explained. In the last section of the methods part, idealized time series with known mean vector and precision matrix are simulated in order to test the accuracy of the spatial homogeneity test.

The results part contains the investigation of different regions of the real data set. In the last part, the above research questions are discussed.

4.2 Methods

4.2.1 Gaussian Markov Random Fields

This section is based on Rue and Held (2005). A Gaussian Markov Random Field GMRF is a random vector $\vec{y} = (y_1, ..., y_n)^T$ following a normal distribution with mean $\vec{\mu}$ and precision matrix $\boldsymbol{Q} = \boldsymbol{\Sigma}^{-1}$. The term Markov implies that assumptions about conditional independence are used. It is assumed that conditional dependence only occurs on a few neighbour sites. The conditional independence structure in a GMRF is usually represented by an undirected graph. An undirected graph is a tuple $G = (\nu, \varepsilon)$, where ν is the set of nodes in the graph and ε is the set of edges $\{i, j\}$ with $i \neq j \in \nu$. If $\{i, j\} \in \varepsilon$, there is an undirected edge from node i to node j. We assume that $\nu = \{1, 2, ..., n\}$, which means that the graph is labelled. As an example, Figure 4.1 a) shows 9 pixels of a regular grid ($\nu = \{1, 2, ..., 9\}$) and the neighbour structure ($\varepsilon = \{\{2,5\}, \{4,5\}, \{5,6\}, \{5,8\}\}$). In Figure 4.1 b), the adjacency matrix $\boldsymbol{A}$ is shown with $a_{ij} = a_{ji} = 1$ if $\{i, j\} \in \varepsilon, \forall i \neq j \in \nu$ and $a_{ij} = a_{ji} = 0$ otherwise.

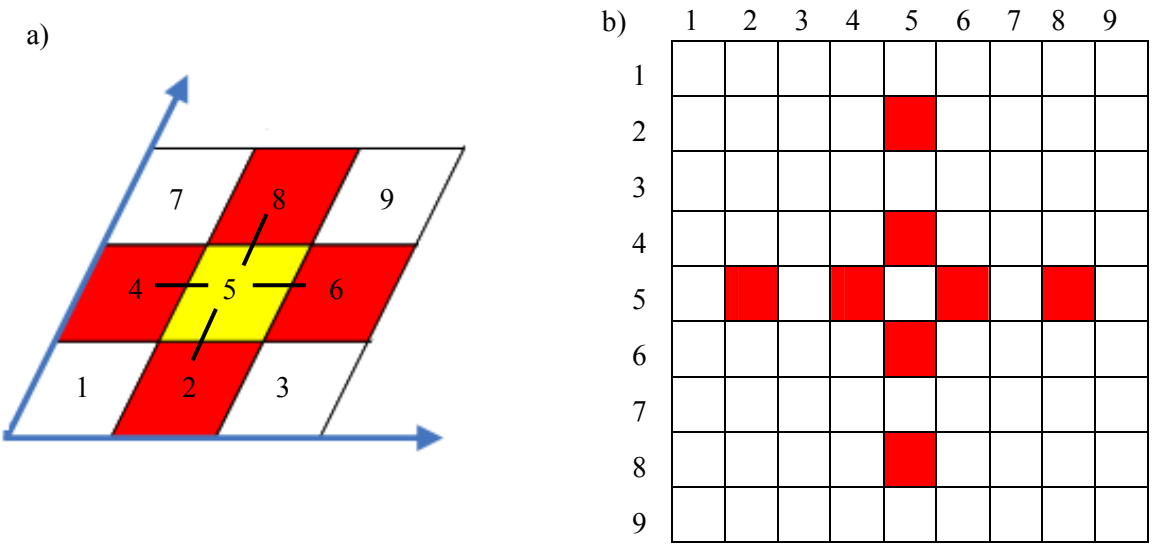

Figure 4.1: Example of a regular grid (a) and the associated adjacency matrix *A* (b)

There are n=9 nodes with $\nu = \{1, 2, ..., 9\}$ and $\varepsilon = \{\{2,5\}, \{4,5\}, \{5,6\}, \{5,8\}\}$.

We write *i*~*j* if node *i* and *j* are neighbors in graph *G*. This relation is symmetric which means that if *i*~*j* then *j*~*i*.

If there is no edge between node *i* and *j*, then y_i and y_j are conditionally independent given $\vec{y}_{-ij}$: $y_i \perp y_j \,|\, \vec{y}_{-ij}$.

In Figure 4.1, for instance, pixel 1 and 5 are conditionally independent given all other pixels except pixel 1 and 5.

The information about the conditional independence properties is given solely by the precision matrix $\boldsymbol{Q}$, the mean $\vec{\mu}$ has no influence. Let $\vec{y}$ be normal distributed with mean $\vec{\mu}$ and precision matrix $\boldsymbol{Q} > 0$ (meaning that $\boldsymbol{Q}$ is a positive definite matrix), then for $i \neq j$:

$$y_i \perp y_j \left| \vec{y}_{-ij} \Leftrightarrow Q_{ij} = 0 \right.$$

This result says that the nonzero pattern of $\boldsymbol{Q}$ determines G and that we know from $\boldsymbol{Q}$ whether y_i and y_j are conditionally independent or not. Next, the formal definition of a univariate GMRF is stated.

Definition of a univariate GMRF

A random vector $\vec{y} = (y_1, ..., y_n)^{\mathsf{T}}$ is called a GMRF with respect to a labelled graph $G = (\nu, \varepsilon)$ with mean $\vec{\mu}$ and precision matrix $\boldsymbol{Q} = \boldsymbol{\Sigma}^{-1}$ if its density has the form:

$$f(\vec{y}) = \left(\frac{1}{2\pi}\right)^{\frac{n}{2}} |\boldsymbol{Q}|^{1/2} \exp\left(-\frac{1}{2}(\vec{y} - \vec{\mu})^{\mathsf{T}} \boldsymbol{Q} (\vec{y} - \vec{\mu})\right)$$

where $Q_{ij} = 0$, if the pixels are not neighbors and thus conditionally independent and $Q_{ij} \neq 0$, if the pixels are neighbors and conditionally dependent.

If $\vec{y}$ is a GMRF with respect to $G = (\nu, \varepsilon)$, then the conditional expectation and precision are:

$$\mathrm{E}\left[y_i \left| \vec{y}_{-i} \right. \right] = \mu_i - \frac{1}{Q_{ii}} \sum_{j:j\sim i} Q_{ij} (y_j - \mu_j)$$

$$\mathrm{Prec}(y_i \left| \vec{y}_{-i} \right.) = Q_{ii}$$

$$\text{with } \vec{y}_{-i} = (y_1, ..., y_{i-1}, y_{i+1}, ... y_n)$$

The diagonal elements of $\boldsymbol{Q}$ represent the conditional precisions of y_i given $\vec{y}_{-i}$ and the off-diagonal elements describe (after a proper scaling) the conditional correlation between y_i and y_j given $\vec{y}_{-ij}$.

A second specification of a GMRF is given through its full conditionals. The full conditionals can be specified as normals with:

$$\mathrm{E}\left[y_i \left| \vec{y}_{-i} \right. \right] = \mu_i + \sum_{j:j\sim i} \beta_{ij} (y_j - \mu_j)$$

$$\mathrm{Prec}(y_i \left| \vec{y}_{-i} \right.) = \kappa_i > 0$$

for i=1,…,n and for some $\beta_{ij}, i \neq j$.

These n full conditionals must satisfy some consistency conditions so that a joint normal density exists. By choosing $Q_{ij} = \kappa_i$ for $i = j$ and $Q_{ij} = -\kappa_i \beta_{ij}$ for $i \neq j$ we have a candidate for a joint density giving the above specified full conditionals. We further require that $\boldsymbol{Q}$ is symmetric ($-\kappa_i \beta_{ij} = -\kappa_j \beta_{ji}$) and positive definite ($\boldsymbol{Q} > 0$).

The above is the definition for univariate (i.e. spatial) GMRFs. As two dimensions (time and space) are present in our climate data record the next section outlines multivariate GMRFs as a multivariate extension of a GMRF.

Definition of a multivariate GMRF

We have a random vector $\vec{y} = (\vec{y}_1^{\mathsf{T}}, ..., \vec{y}_T^{\mathsf{T}})^{\mathsf{T}}$ with T nodes where $t = 1,\ldots,T$ is the time index. We now associate a vector with dimension n (n = number of pixels) with each of these T nodes. This random vector $\vec{y} = (\vec{y}_1^{\mathsf{T}}, ..., \vec{y}_T^{\mathsf{T}})^{\mathsf{T}}$ is then called a multivariate GMRF (MGMRF) with respect to a graph $G = (\nu = \{1,...,T\}, \varepsilon)$ with mean $\vec{\mu} = (\vec{\mu}_1^{\mathsf{T}}, ..., \vec{\mu}_T^{\mathsf{T}})^{\mathsf{T}}$ and precision matrix $\tilde{\boldsymbol{Q}} = (\tilde{\boldsymbol{Q}}_{tu})$, $\tilde{\boldsymbol{Q}} > 0$. The matrix $\tilde{\boldsymbol{Q}}$ is of size $Tn \times Tn$ and $\tilde{\boldsymbol{Q}}_{tu}$ of size $n \times n$. To point out that $\tilde{\boldsymbol{Q}}_{tu}$ is a temporal block matrix, in the multivariate case the indices t and u are used instead of i and j.

$$\vec{y} = \begin{pmatrix} \vec{y}_1 \\ \vdots \\ \vec{y}_T \end{pmatrix} \sim N_{\mathrm{nT}} \left(\begin{pmatrix} \vec{\mu}_1 \\ \vdots \\ \vec{\mu}_T \end{pmatrix}, \tilde{\boldsymbol{Q}} \right)$$

The density of a MGMRF has the form: $f(\vec{y}) = \left(\frac{1}{2\pi}\right)^{\frac{Tn}{2}} \left|\tilde{\boldsymbol{Q}}\right|^{1/2} \exp\left(-\frac{1}{2} \sum_{tu} (\vec{y}_t - \vec{\mu}_t)^{\mathsf{T}} \tilde{\boldsymbol{Q}}_{tu} (\vec{y}_u - \vec{\mu}_u) \right)$

and whole blocks of $\tilde{\boldsymbol{Q}}_{tu}$ are 0 if $\vec{y}_t$ and $\vec{y}_u$ are conditionally independent given $\vec{y}_{-tu}$.

At each time index t, n pixels are investigated. In comparison to the univariate GMRF every entry $\vec{y}_t$ consists of a n-dimensional vector (n = number of pixels). There is one μ_{it} for every pixel and time index. Figure 4.2 visually outlines the differences between a univariate and a multivariate GMRF.

Univariate GMRF	$\vec{\mu} = \begin{pmatrix} \mu_1 \\ \mu_2 \\ \vdots \\ \mu_n \end{pmatrix}_{n \times 1}$	$\boldsymbol{Q} = \begin{bmatrix} q_{11} & q_{21} & q_{31} & \cdots & q_{n1} \\ q_{12} & q_{22} & q_{32} & \cdots & q_{n2} \\ q_{13} & q_{23} & q_{33} & \cdots & q_{n3} \\ \vdots & \vdots & \vdots & \ddots & \vdots \\ q_{1n} & q_{2n} & q_{3n} & \cdots & q_{nn} \end{bmatrix}_{n \times n}$
Multivariate GMRF	$\vec{\mu} = \begin{pmatrix} \vec{\mu}_1 \\ \vdots \\ \vec{\mu}_T \end{pmatrix}_{Tn \times 1}$	$\tilde{\boldsymbol{Q}} = \begin{bmatrix} \tilde{\boldsymbol{Q}}_{11} & \tilde{\boldsymbol{Q}}_{12} & \cdots & \tilde{\boldsymbol{Q}}_{1t} & \cdots & \tilde{\boldsymbol{Q}}_{1T} \\ \tilde{\boldsymbol{Q}}_{21} & \tilde{\boldsymbol{Q}}_{22} & \cdots & \tilde{\boldsymbol{Q}}_{2t} & \cdots & \tilde{\boldsymbol{Q}}_{2T} \\ \vdots & \vdots & \ddots & \vdots & & \vdots \\ \tilde{\boldsymbol{Q}}_{t1} & \tilde{\boldsymbol{Q}}_{t2} & \cdots & \tilde{\boldsymbol{Q}}_{tt} & \cdots & \tilde{\boldsymbol{Q}}_{tT} \\ \vdots & \vdots & & \vdots & \ddots & \vdots \\ \tilde{\boldsymbol{Q}}_{T1} & \tilde{\boldsymbol{Q}}_{T2} & \cdots & \tilde{\boldsymbol{Q}}_{Tt} & \cdots & \tilde{\boldsymbol{Q}}_{TT} \end{bmatrix}_{Tn \times Tn}$

Figure 4.2: Mean vector and precision matrix of a univariate and multivariate GMRF

In the multivariate case, $\vec{\mu}$ consists of vector of dimension $Tn \times 1$ and the precision matrix has $T \times T$ block matrices of size $n \times n$.

Similarly to the univariate case, conditional expectation and precision can be defined:

$$\mathrm{E}\left[\vec{y}_t \,|\, \vec{y}_{-t}\right] = \vec{\mu}_t - \tilde{\boldsymbol{Q}}_{tt}^{-1} \sum_{u:u\sim t} \tilde{\boldsymbol{Q}}_{tu} (\vec{y}_u - \vec{\mu}_u)$$

$$\mathrm{Prec}(\vec{y}_t \,|\, \vec{y}_{-t}) = \tilde{\boldsymbol{Q}}_{tt}$$

If $\vec{y}_t$ and $\vec{y}_u$ are conditionally independent given $\vec{y}_{-tu}$, then the whole block $\tilde{\boldsymbol{Q}}_{tu}$ is zero. The above specification can again be expressed through the full conditionals as normals:

$$\mathrm{E}\left[\vec{y}_t \middle| \vec{y}_{-t}\right] = \vec{\mu}_t + \sum_{u:u\sim t} \boldsymbol{\beta}_{tu}\left(\vec{y}_u - \vec{\mu}_u\right)$$

$$\mathrm{Prec}\left(\vec{y}_t \middle| \vec{y}_{-t}\right) = \boldsymbol{\kappa}_t > 0$$

for $t = 1,\ldots,T$ and for some $n \times n$ matrices $\boldsymbol{\beta}_{tu}, t \neq u$ and $\boldsymbol{\kappa}_t$.

For all $\vec{y}_t$ and $\vec{y}_u$ that are conditionally dependent given $\vec{y}_{-tu}$, $n \times n$ matrices $\boldsymbol{\kappa}_t$ and $\boldsymbol{\kappa}_t\boldsymbol{\beta}_{tu}$ exist:

$$\tilde{\boldsymbol{Q}}_{tu} = \begin{cases} -\boldsymbol{\kappa}_t\boldsymbol{\beta}_{tu} & \text{for } t \neq u \\ \boldsymbol{\kappa}_t & \text{for } t = u \end{cases}$$

where $\boldsymbol{\kappa}_t\boldsymbol{\beta}_{tu}$ and $\boldsymbol{\kappa}_t$ are both $n \times n$ matrices.

4.2.2 Description of the mean vector and precision matrix

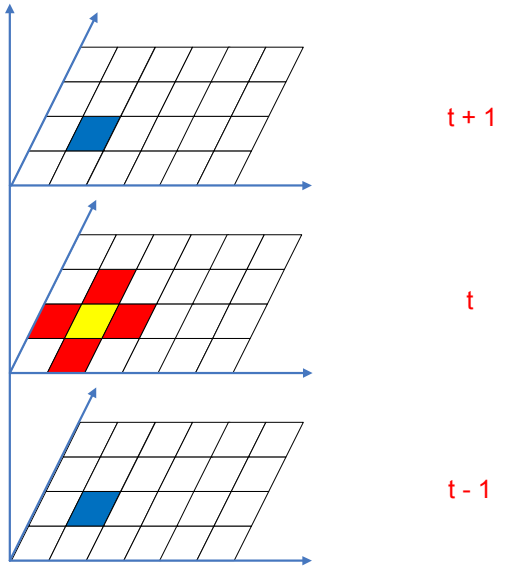

In this section, the mean vector and the entries of the precision matrix are described for application with the CM SAF climate data record. A multivariate GMRF that includes time and space is used since the climate data record has both a space and time dimension.

Here, a model in which each pixel only conditionally depends on its own temporal neighbors is considered (yellow pixel is only conditionally dependent on the two blue pixels). There are also other models for space and time interactions, see for example Rue and Held (2005), p.120ff or Knorr-Held (2000).

It is useful to define the precision matrix as a Kronecker product. The exact construction of the precision matrix by using the sum of two Kronecker products is described later.

Figure 4.3: Spatially and temporal dependency of adjacent pixels within the climate data record

The red pixels represent the spatially and the blue pixels the temporally dependent neighbors.

Figure 4.3 illustrates a spatio-temporal cross-section of the climate data record. Each pixel has a mean (yellow pixel) and four spatial (red pixels) and two temporal neighbors (blue pixels). For every pixel and every time index the conditional expectation and spatial dependence structure has to be defined. The dependence structure is expressed in the precision matrix $\tilde{\boldsymbol{Q}}$ which corresponds to a block matrix.

Mean vector $\vec{\mu}$

Every pixel and every time index is described by one μ_{it}. Under H_0, every pixel in the field has a separate mean vector. Under H_1, there are two different mean vectors for every pixel. The mean vector looks as follows:

$$\vec{\mu} = \begin{pmatrix} \vec{\mu}_1 \\ \vdots \\ \vec{\mu}_T \end{pmatrix}$$

Precision matrix Q

As outlined above, the precision matrix contains the spatial and temporal dependence structure. $\tilde{\boldsymbol{Q}} = (\tilde{\boldsymbol{Q}}_{tu})$ is a block matrix and each element $\tilde{\boldsymbol{Q}}_{tu}$ is a $n \times n$ matrix.

Figure 4.4 visualizes how the $\tilde{\boldsymbol{Q}}_{tt}$, $t=1,\ldots,T$ containing the spatial correlation are arranged in the diagonal (in red). The $\tilde{\boldsymbol{Q}}_{t+1,t}, \tilde{\boldsymbol{Q}}_{t,t+1}, t = 1,\ldots,T-1$ contain the temporal correlation structure (in blue). Since only the pixels of one time index before and one time index after are chosen to be conditionally dependent, only the first off diagonals have non-zero entries. All other $\tilde{\boldsymbol{Q}}_{tu}$ are set to zero (in black).

$$\tilde{\boldsymbol{Q}} = \begin{pmatrix} \tilde{\boldsymbol{Q}}_{11} & \tilde{\boldsymbol{Q}}_{12} & \cdots & \tilde{\boldsymbol{Q}}_{1t} & \cdots & \tilde{\boldsymbol{Q}}_{1T} \\ \tilde{\boldsymbol{Q}}_{21} & \tilde{\boldsymbol{Q}}_{22} & \ddots & \tilde{\boldsymbol{Q}}_{2t} & \cdots & \tilde{\boldsymbol{Q}}_{2T} \\ \vdots & \ddots & \ddots & \ddots & \ddots & \vdots \\ \tilde{\boldsymbol{Q}}_{t1} & \ddots & \tilde{\boldsymbol{Q}}_{t,t-1} & \tilde{\boldsymbol{Q}}_{tt} & \tilde{\boldsymbol{Q}}_{t,t+1} & \tilde{\boldsymbol{Q}}_{tT} \\ \vdots & \ddots & \ddots & \ddots & \ddots & \vdots \\ \tilde{\boldsymbol{Q}}_{T1} & \tilde{\boldsymbol{Q}}_{T2} & \cdots & \tilde{\boldsymbol{Q}}_{Tt} & \cdots & \tilde{\boldsymbol{Q}}_{TT} \end{pmatrix}$$

Figure 4.4: Structure of precision matrix

The red blocks contain the spatial and the blue blocks the temporal correlation structure.

Next, the spatial and temporal block structure of the precision matrix is described in more detail. All spatial blocks are equal and all temporal blocks are equal. First, the construction of one single spatial and one single temporal block is depicted and then the construction of the whole precision matrix $\tilde{\boldsymbol{Q}}$ is described. In the following, only one spatial block and one temporal is considered, thus we are again in the univariate case and the indices i and j are used again. Within one $\tilde{\boldsymbol{Q}}_{tu}$ there are $n \times n$ pixels and $i = 1,\ldots,n$ and $j = 1,\ldots,n$.

Spatial blocks:

One $\tilde{\boldsymbol{Q}}_{tt}$ is constructed as follows:

$$\tilde{\boldsymbol{Q}}_{tt} = \tilde{\boldsymbol{Q}}_{11} = (\boldsymbol{I}_n - \beta_{ij}^{sp} \boldsymbol{A})\kappa_i$$

where $\boldsymbol{I}_n$ is the identity matrix of size $n \times n$ and $\boldsymbol{A}$ an adjacency matrix with $a_{ij} = a_{ji} = 1$ if $\{i,j\} \in \varepsilon, \forall i \neq j \in v$ and $a_{ij} = a_{ji} = 0$ otherwise. The structure of $\tilde{\boldsymbol{Q}}_{tt} = \tilde{\boldsymbol{Q}}_{11}$ (example of a 6×4 grid) is shown in Figure 4.5 bottom. In our model $\boldsymbol{A}$ is chosen so that the four direct spatial neighbors (see

Figure 4.3) of each pixel have entries equal to 1. Some border pixel have only two or three spatial neighbors (see Figure 4.5 top). This is the reason why some pixels in the first off diagonals in Figure 4.5 are zero. For instance, pixel 6 has only neighbours 5 and 12 and hence $a_{ij} = a_{ji} = 0$ for i=6 and j=7. The diagonal elements of $\tilde{\boldsymbol{Q}}_{tt} = \tilde{\boldsymbol{Q}}_{11}$ (yellow pixes in Figure 4.5 bottom) are κ_i and the red pixels in Figure 4.5 (where $a_{ij} = a_{ji} = 1$) are equal to $-\kappa_i \beta_{ij}^{sp}$.

19	20	21	22	23	24
13	14	15	16	17	18
7	8	9	10	11	12
1	2	3	4	5	6

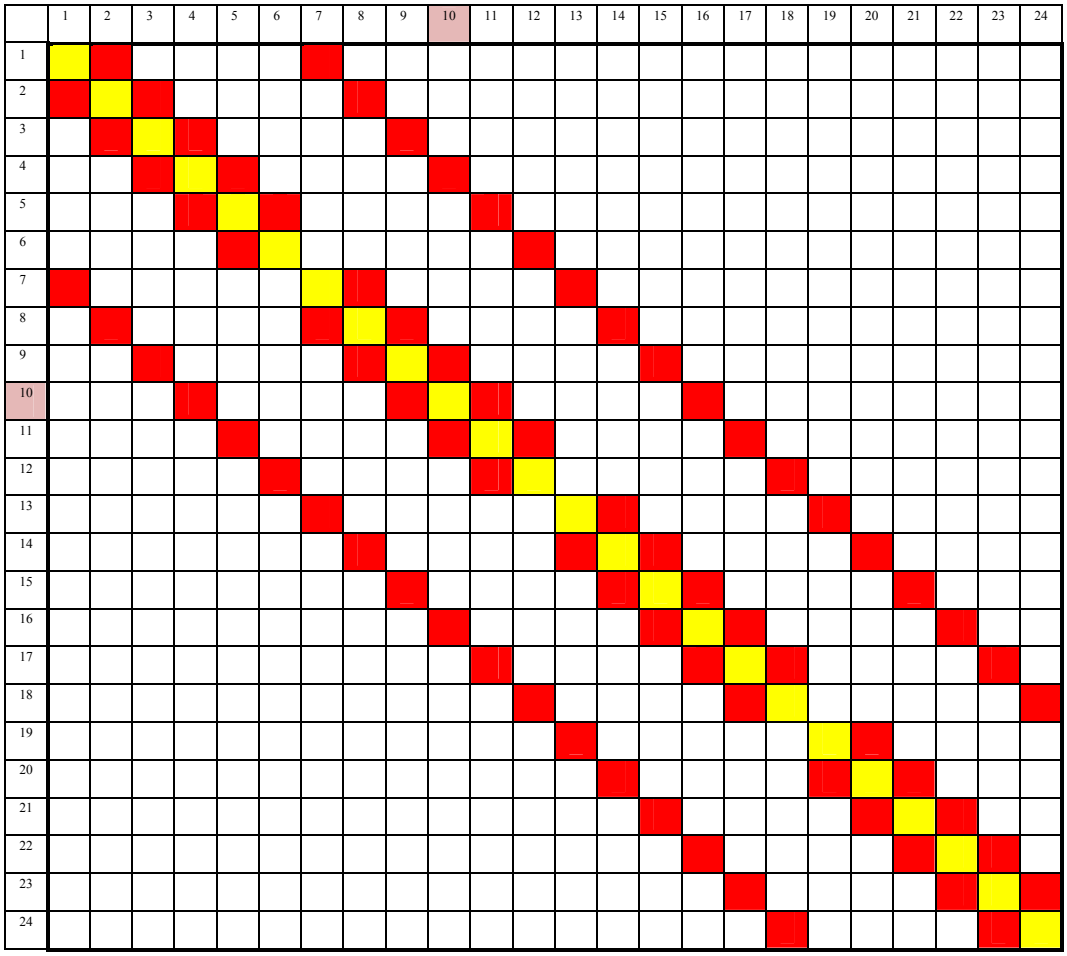

Figure 4.5: Layout of the 6x4 grid (top) and structure of $\tilde{\boldsymbol{Q}}_{tt} = \tilde{\boldsymbol{Q}}_{11}$ (bottom).

The red pixels are neighbors of the yellow pixels and contain the $-\kappa_j \beta_{ij}^{sp}$.

One example of the dependence structure is given: Pixel 10 conditionally depends on the pixels 4, 9, 11 and 16.

With help of the above mentioned specification of GMRFs as full conditionals, $\tilde{\boldsymbol{Q}}_{tt}$, $\mathbf{K}$, $\mathbf{B}^{sp}$ can be expressed as follows (here again the indices i and j are used to make clear that we are within one single block and ^{sp} stands for spatial):

$$\tilde{\boldsymbol{Q}}_{tt} = \tilde{\boldsymbol{Q}}_{11} = \mathbf{K} \cdot \mathbf{B}^{sp} = \begin{pmatrix} \kappa_i & 0 & \dots & \dots & \dots & \dots & \dots & \dots & 0 \\ 0 & \ddots & 0 & & & & & & \vdots \\ \vdots & 0 & \ddots & 0 & & & & & \vdots \\ \vdots & & 0 & \ddots & \ddots & & & & \vdots \\ \vdots & & & 0 & \ddots & 0 & & & \vdots \\ \vdots & & & & \ddots & \ddots & 0 & & \vdots \\ \vdots & & & & & 0 & \ddots & 0 & \vdots \\ \vdots & & & & & & 0 & \ddots & 0 \\ 0 & \dots & \dots & \dots & \dots & \dots & \dots & 0 & \kappa_i \end{pmatrix} \begin{pmatrix} 1 & -\beta_{ij}^{sp} & 0 & \dots & 0 & -\beta_{ij}^{sp} & 0 & \dots & 0 \\ -\beta_{ij}^{sp} & \ddots & \ddots & 0 & \ddots & 0 & \ddots & \ddots & \vdots \\ 0 & \ddots & \ddots & \ddots & 0 & \ddots & \ddots & \ddots & 0 \\ \vdots & 0 & \ddots & \ddots & \ddots & \ddots & \ddots & 0 & -\beta_{ij}^{sp} \\ 0 & \ddots & 0 & \ddots & \ddots & & 0 & \ddots & 0 \\ -\beta_{ij}^{sp} & 0 & \ddots & \ddots & & \ddots & \ddots & 0 & \vdots \\ 0 & \ddots & \ddots & \ddots & 0 & \ddots & \ddots & \ddots & 0 \\ \vdots & \ddots & \ddots & 0 & \ddots & 0 & \ddots & \ddots & -\beta_{ij}^{sp} \\ 0 & \dots & 0 & -\beta_{ij}^{sp} & 0 & \dots & 0 & -\beta_{ij}^{sp} & 1 \end{pmatrix}$$

$$= \begin{pmatrix} \kappa_i & -\kappa_i\beta_{ij}^{sp} & 0 & \dots & 0 & -\kappa_i\beta_{ij}^{sp} & 0 & \dots & 0 \\ -\kappa_i\beta_{ij}^{sp} & \ddots & \ddots & 0 & \ddots & 0 & \ddots & \ddots & \vdots \\ 0 & \ddots & \ddots & \ddots & 0 & \ddots & \ddots & \ddots & 0 \\ \vdots & 0 & \ddots & \ddots & \ddots & \ddots & \ddots & 0 & -\kappa_i\beta_{ij}^{sp} \\ 0 & \ddots & 0 & \ddots & \ddots & \ddots & 0 & \ddots & 0 \\ -\kappa_i\beta_{ij}^{sp} & 0 & \ddots & \ddots & \ddots & \ddots & \ddots & 0 & \vdots \\ 0 & \ddots & \ddots & \ddots & 0 & \ddots & \ddots & \ddots & 0 \\ \vdots & \ddots & \ddots & 0 & \ddots & 0 & \ddots & \ddots & -\kappa_i\beta_{ij}^{sp} \\ 0 & \dots & 0 & -\kappa_i\beta_{ij}^{sp} & 0 & \dots & 0 & -\kappa_i\beta_{ij}^{sp} & \kappa_i \end{pmatrix}$$

Note that some entries in the first off diagonals in matrix $\tilde{\boldsymbol{Q}}_{tt}$ and $\tilde{\mathbf{B}}^{sp}$ are 0.

Temporal block:

As the temporal blocks are located in the first off-diagonals, $\vec{y}_t$ only depends on $\vec{y}_{t+1}$ and $\vec{y}_{t-1}$ (blue $\tilde{\boldsymbol{Q}}_{tu}$ in Figure 4.4). Only the diagonal elements of the temporal precision matrices are non-zero since each pixel solely conditionally depends on its own temporal neighbors. One matrix $\tilde{\boldsymbol{Q}}_{tu}$ is:

$$\tilde{\boldsymbol{Q}}_{tu} = \tilde{\boldsymbol{Q}}_{12} = (-\beta_{ij}^{te} \boldsymbol{I}_n)\kappa_i$$

Thus, only the diagonal elements of the temporal block are equal to $-\kappa_i \beta_{ij}^{te}$.

Expressed as full conditionals (^{te} stands for temporal):

$$\tilde{\boldsymbol{Q}}_{tu} = \tilde{\boldsymbol{Q}}_{12} = \mathbf{K} \cdot \mathbf{B}^{te} = \begin{pmatrix} \kappa_i & 0 & \dots & \dots & \dots & \dots & \dots & \dots & 0 \\ 0 & \ddots & 0 & & & & & & \vdots \\ \vdots & 0 & \ddots & 0 & & & & & \vdots \\ \vdots & & 0 & \ddots & \ddots & & & & \vdots \\ \vdots & & & 0 & \ddots & 0 & & & \vdots \\ \vdots & & & & \ddots & \ddots & 0 & & \vdots \\ \vdots & & & & & 0 & \ddots & 0 & \vdots \\ \vdots & & & & & & 0 & \ddots & 0 \\ 0 & \dots & \dots & \dots & \dots & \dots & \dots & 0 & \kappa_i \end{pmatrix} \begin{pmatrix} -\beta_{ij}^{te} & 0 & \dots & \dots & \dots & \dots & \dots & \dots & 0 \\ 0 & \ddots & 0 & & & & & & \vdots \\ \vdots & 0 & \ddots & 0 & & & & & \vdots \\ \vdots & & 0 & \ddots & \ddots & & & & \vdots \\ \vdots & & & 0 & \ddots & 0 & & & \vdots \\ \vdots & & & & \ddots & \ddots & 0 & & \vdots \\ \vdots & & & & & 0 & \ddots & 0 & \vdots \\ \vdots & & & & & & 0 & \ddots & 0 \\ 0 & \dots & \dots & \dots & \dots & \dots & \dots & 0 & -\beta_{ij}^{te} \end{pmatrix}$$

$$= \begin{pmatrix} -\beta_{ij}^{te}\kappa_i & 0 & \dots & \dots & \dots & \dots & \dots & \dots & 0 \\ 0 & \ddots & 0 & & & & & & \vdots \\ \vdots & 0 & \ddots & 0 & & & & & \vdots \\ \vdots & & 0 & \ddots & \ddots & & & & \vdots \\ \vdots & & & 0 & \ddots & 0 & & & \vdots \\ \vdots & & & & \ddots & \ddots & 0 & & \vdots \\ \vdots & & & & & 0 & \ddots & 0 & \vdots \\ \vdots & & & & & & 0 & \ddots & 0 \\ 0 & \dots & \dots & \dots & \dots & \dots & \dots & 0 & -\beta_{ij}^{te}\kappa_i \end{pmatrix}$$

Full precision matrix:

$\tilde{\boldsymbol{Q}}$ is now composed of the spatial and temporal blocks as shown in Figure 4.4. In order to construct $\tilde{\boldsymbol{Q}}$, the Kronecker product can be used

$$\tilde{\boldsymbol{Q}} = (\boldsymbol{I}_T \otimes \tilde{\boldsymbol{Q}}_{tt} + \boldsymbol{C} \otimes \tilde{\boldsymbol{Q}}_{tu})$$

where $\boldsymbol{C}$ is a $T \times T$ matrix with c_{tt}= 0 and $c_{t,t+1}$=1 and $c_{t,t-1}$ = 1, $t > 1$ and 0 otherwise. This leads to the matrix presented in Figure 4.6. For better readability a simpler 3x3 region with 3 time indices is chosen.

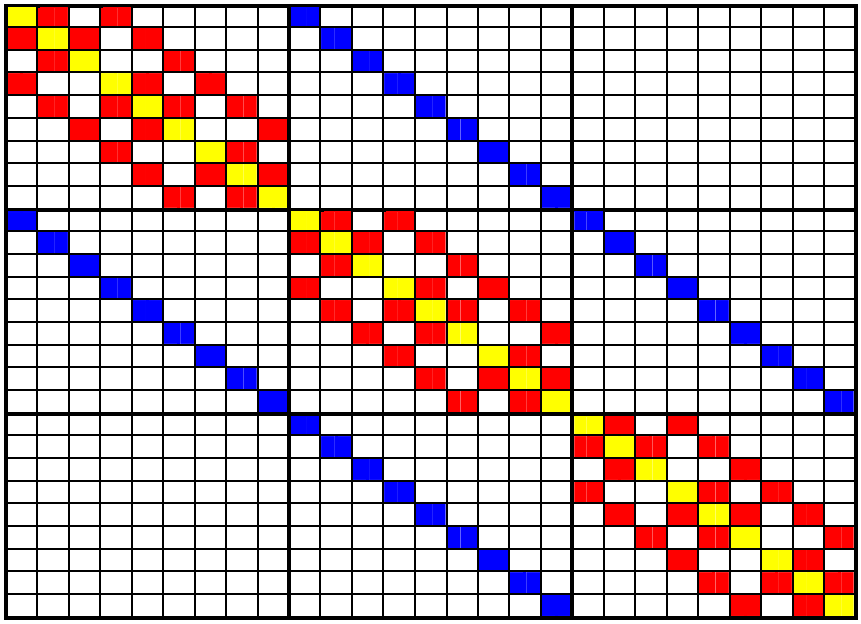

Figure 4.6: Full precision matrix with spatial and temporal entries

The red pixels represent the spatially and the blue ones the temporally dependent pixels. The yellow pixels are κ_i, the red are $-\kappa_i \beta_{ij}^{sp}$ and the blue pixels are $-\kappa_i \beta_{ij}^{te}$.

Also here, the full conditionals can be used to define the MGMRF. β_{ij}^{sp} and β_{ij}^{te} denote different parameters for the spatial and temporal dependence structure.

$\tilde{\boldsymbol{Q}} = \tilde{\mathbf{K}} \cdot \tilde{\mathbf{B}}$, with

$$\tilde{\mathbf{K}} = \begin{pmatrix} \kappa_i & 0 & \cdots & \cdots & 0 \\ 0 & \ddots & 0 & & \vdots \\ \vdots & 0 & \ddots & 0 & \vdots \\ \vdots & & 0 & \ddots & 0 \\ 0 & \cdots & \cdots & 0 & \kappa_i \end{pmatrix}$$

$$\tilde{\mathbf{B}} = \begin{pmatrix} 1 & -\beta_{ij}^{sp} & 0 & \cdots & 0 & -\beta_{ij}^{sp} & 0 & \cdots & 0 \\ -\beta_{ij}^{sp} & \ddots & \ddots & 0 & \ddots & 0 & \ddots & \ddots & \vdots \\ 0 & \ddots & \ddots & \ddots & 0 & \ddots & \ddots & \ddots & 0 \\ \vdots & 0 & \ddots & \ddots & \ddots & \ddots & \ddots & 0 & -\beta_{ij}^{sp} \\ 0 & \ddots & 0 & \ddots & \ddots & \ddots & 0 & \ddots & 0 \\ -\beta_{ij}^{sp} & 0 & \ddots & \ddots & \ddots & \ddots & \ddots & 0 & \vdots \\ 0 & \ddots & \ddots & \ddots & 0 & \ddots & \ddots & \ddots & 0 \\ \vdots & \ddots & \ddots & 0 & \ddots & 0 & \ddots & \ddots & -\beta_{ij}^{sp} \\ 0 & \cdots & 0 & -\beta_{ij}^{sp} & 0 & \cdots & 0 & -\beta_{ij}^{sp} & 1 \end{pmatrix}$$

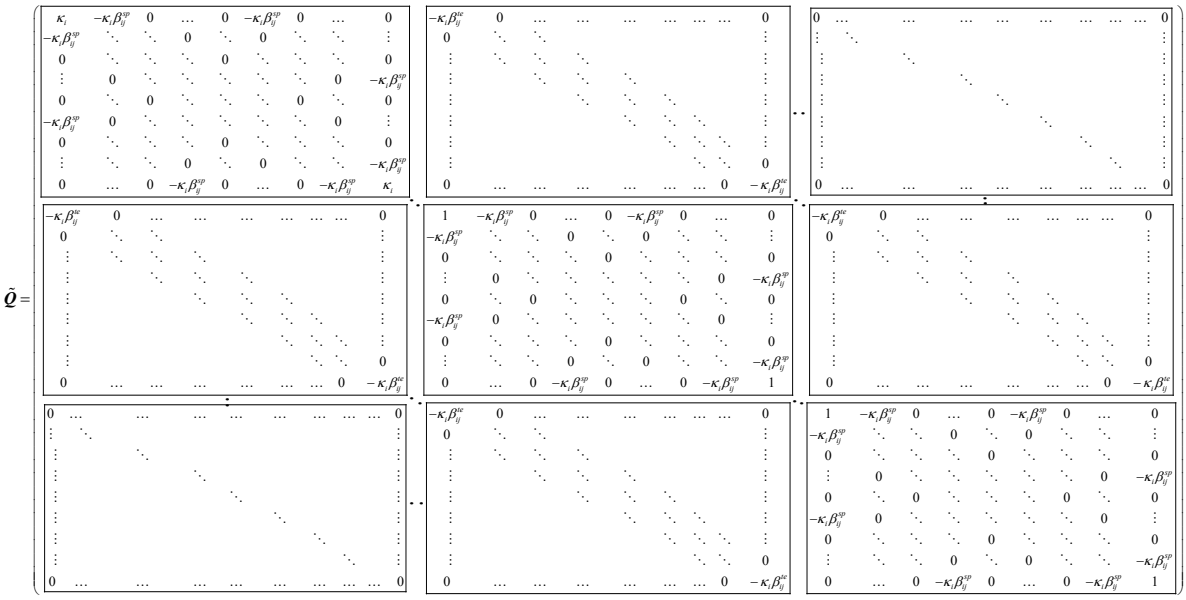

Here again, it must be noted that some elements in the first off diagonals in matrix $\tilde{\boldsymbol{Q}}$ and $\tilde{\mathbf{B}}$ are 0.

4.2.3 Model and model assumptions

Null and alternative hypothesis:

In the following, i and j denote the spatial and t and t' the temporal indices and $i = 1,\ldots,n, j = 1,\ldots,n$, $t = 1,\ldots,T$ and $t' = 1,\ldots T$.

H_0: There is no break at any time index for all observations y_{it} in the considered region.

$$H_0 : \mu_{it} = \mu_{it'}, \text{ but } \mu_{it} \neq \mu_{jt} \text{ for } i \neq j, t < t'$$

H_1: There is a break at time index t_b for the observations y_{it} in the considered region.

$$H_1 : \begin{cases} \mu_{it} = \mu_{it'} \forall t, t' \leq t_b \\ \text{for some i: } \mu_{it'} = \mu_{it} + a \ \forall t' > t_b \\ \text{for all other i: } \mu_{it'} = \mu_{it} \forall t' > t_b \end{cases}$$

a is a scalar and equal for all pixels.

Distribution of y_{it} under H_0 and H_1:

$$\vec{y} = \begin{pmatrix} \vec{y}_1 \\ \vdots \\ \vec{y}_t \\ \vdots \\ \vec{y}_T \end{pmatrix} \sim \mathrm{N}_{Tn} \left(\begin{pmatrix} \vec{\mu}_1 \\ \vdots \\ \vec{\mu}_t \\ \vdots \\ \vec{\mu}_T \end{pmatrix}, \begin{pmatrix} \tilde{\boldsymbol{Q}}_{11} & \tilde{\boldsymbol{Q}}_{12} & 0 & 0 & 0 \\ \tilde{\boldsymbol{Q}}_{21} & \ddots & \tilde{\boldsymbol{Q}}_{t-1,t} & 0 & 0 \\ 0 & \tilde{\boldsymbol{Q}}_{t,t-1} & \tilde{\boldsymbol{Q}}_{tt} & \tilde{\boldsymbol{Q}}_{t,t+1} & 0 \\ 0 & 0 & \tilde{\boldsymbol{Q}}_{t+1,t} & \ddots & \tilde{\boldsymbol{Q}}_{T-1,T} \\ 0 & 0 & 0 & \tilde{\boldsymbol{Q}}_{T,T-1} & \tilde{\boldsymbol{Q}}_{TT} \end{pmatrix} \right),$$

under H_0: $\mu_{i1} = \mu_{it} = \mu_{it'}, \text{but } \mu_{it} \neq \mu_{jt}, t < t'$

under H_1: $\mu_{it'} = \mu_{it} + a, \forall t' > t_b, \text{but } \mu_{it} \neq \mu_{jt}$

Density of y_{it} under H_0 and H_1:

$$f(\vec{y}) = \left(\frac{1}{2\pi}\right)^{\frac{nT}{2}} \left|\tilde{\boldsymbol{Q}}\right|^{1/2} \cdot \exp\left(-\frac{1}{2} \begin{pmatrix} y_{11}-\mu_{11} \\ y_{21}-\mu_{21} \\ \vdots \\ y_{n1}-\mu_{n1} \\ \vdots \\ y_{1t}-\mu_{1t} \\ y_{2t}-\mu_{2t} \\ \vdots \\ y_{nt}-\mu_{nt} \\ \vdots \\ y_{1T}-\mu_{1T} \\ y_{2T}-\mu_{2T} \\ \vdots \\ y_{nT}-\mu_{nT} \end{pmatrix}^{\mathsf{T}} \begin{pmatrix} \tilde{\boldsymbol{Q}}_{11} & \tilde{\boldsymbol{Q}}_{1t} & \cdots & 0 \\ \tilde{\boldsymbol{Q}}_{t1} & \tilde{\boldsymbol{Q}}_{tt} & \cdots & \tilde{\boldsymbol{Q}}_{T-1,T} \\ \vdots & \ddots & \ddots & \vdots \\ 0 & \tilde{\boldsymbol{Q}}_{T,T-1} & \cdots & \tilde{\boldsymbol{Q}}_{TT} \end{pmatrix} \begin{pmatrix} y_{11}-\mu_{11} \\ y_{21}-\mu_{21} \\ \vdots \\ y_{n1}-\mu_{n1} \\ \vdots \\ y_{1t}-\mu_{1t} \\ y_{2t}-\mu_{2t} \\ \vdots \\ y_{nt}-\mu_{nt} \\ \vdots \\ y_{1T}-\mu_{1T} \\ y_{2T}-\mu_{2T} \\ \vdots \\ y_{nT}-\mu_{nT} \end{pmatrix} \right),$$

under H_0: $\mu_{i1} = \mu_{it} = \mu_{it'}$, but $\mu_{it} \neq \mu_{jt}, t < t'$

under H_1: $\mu_{it'} = \mu_{it} + a, \forall t' > t_b$, but $\mu_{it} \neq \mu_{jt}$

Models and assumptions

Three different models were formulated with different parameterizations of the precision matrices. For all three models the conditional expectation and precision are defined after Rue and Held (2005):

$$\mathrm{E}\left[y_{it} \middle| \vec{y}_{-it}\right] = \mu_{it} + \beta_{ij}^{sp} \sum_{j:i\sim j} \left(y_{jt} - \mu_{jt}\right) + \beta_{ij}^{te} \sum_{u:t\sim u} \left(y_{iu} - \mu_{iu}\right)$$

$$\mathrm{Prec}(y_{it} \mid \vec{y}_{-it}) = \kappa_i > 0$$

As mentioned above, in matrix terms:

$$\tilde{\boldsymbol{Q}}_{tt} = \tilde{\boldsymbol{Q}}_{11} = \mathbf{K} \cdot \mathbf{B}^{sp}$$

$$\tilde{\boldsymbol{Q}}_{tu} = \tilde{\boldsymbol{Q}}_{12} = \mathbf{K} \cdot \mathbf{B}^{te}$$

The β_{ij}^{sp} of $\mathbf{B}^{sp}$ and the β_{ij}^{te} of $\mathbf{B}^{te}$ ($\beta_{ij}^{sp}, \beta_{ij}^{te} \neq 0$) express the spatial and temporal dependence structure (influence of the red and blue pixels on the yellow pixels in Figure 4.3) and κ_i represents the precision. κ_i as well as $-\kappa_i \beta_{ij}$ are parameterized differently in each model. The κ_i is determined on the one hand by the diagonal entries of the precision matrix and on the other hand by a constant c that is multiplicative. c is in the following model descriptions ignored, but explained in the text.

Model 1:

This is the original model as described in Rue and Held (2005). The diagonal elements are defined as κ_i=1. The non-zero off-diagonals of $\tilde{\boldsymbol{Q}}$ are parameterized by either b or f, depending on whether it is the spatial or temporal block of $\tilde{\boldsymbol{Q}}$.

$\tilde{\boldsymbol{Q}}_{tt} = \tilde{\boldsymbol{Q}}_{11},\ldots,\tilde{\boldsymbol{Q}}_{TT} = \mathbf{K}\cdot\mathbf{B}^{sp}$

$\tilde{\boldsymbol{Q}}_{tu} = \mathbf{K}\cdot\mathbf{B}^{te}$ for $|t-u|=1$

κ_i of $\mathbf{K}$ are 1

The $\kappa_i\beta_{ij}^{sp}$ of $\mathbf{K}\cdot\mathbf{B}^{sp}$ are parametrized by b

and the $\kappa_i\beta_{ij}^{te}$ of $\mathbf{K}\cdot\mathbf{B}^{te}$ by f

thus $\beta_{ij}^{sp} = b$ and $\beta_{ij}^{te} = f$

The parameter c is not presented above, but as mentioned κ_i consists of the diagonal entries of the matrix $\tilde{\boldsymbol{Q}}$ and of a constant c. As c is part of κ_i, $\tilde{\boldsymbol{Q}}$ is multiplied by c. Because $\tilde{\boldsymbol{Q}}$ is a symmetric positive definite (SPD) matrix, b and f cannot take any value. Therefore corresponding restrictions have to be set for maximum likelihood estimation. The valid two-dimensional parameter space for $b > 0$ and $f > 0$ is outlined in Figure 4.7.

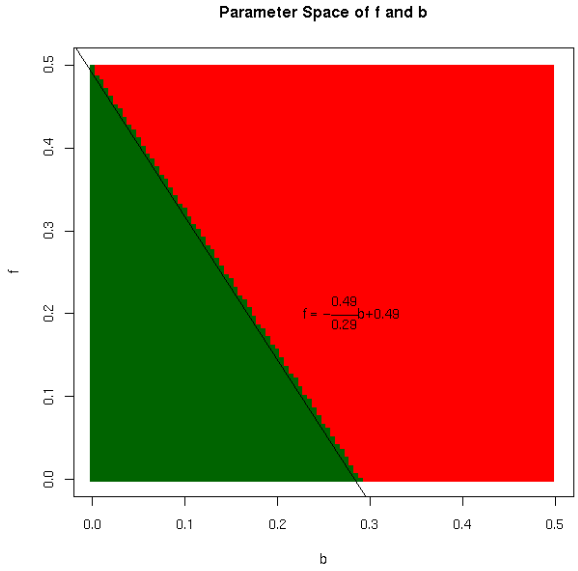

Figure 4.7: Parameter space for *b*>0 and *f*>0 under model 1

Valid parameter space in green and linear function that separates it approximately from the invalid parameter space.

In the maximum likelihood estimation[1] the lower and upper boundary of each parameter can be defined separately. The maximum likelihood estimator is then searching the optimal parameters in a rectangular box. Obviously, a rectangular box is not appropriate here because it would strongly delimit the parameter space. A function $f = -\frac{0.49}{0.29}b + 0.49$ that separates approximately the valid parameter space from the one where the matrix wouldn't be positive definite, is defined. This function is inserted and guarantees that only the green parameter area is searched during the maximum likelihood estimation process.

In Model 1, b and f can never be larger than 0.3 or 0.5, respectively.

[1] The R function optim() is used

Model 2:

This model is an extension of the first model. The diagonal elements of the precision matrix are set to the number of spatially and temporally dependent neighbors *(#nb*). This allows the choice of higher values for *b* and *f* that still enable positive definite precision matrices.

$$\tilde{\boldsymbol{Q}}_{tt} = \tilde{\boldsymbol{Q}}_{11},\ldots,\tilde{\boldsymbol{Q}}_{TT} = \mathbf{K}\cdot\mathbf{B}^{sp}$$
$$\tilde{\boldsymbol{Q}}_{tu} = \mathbf{K}\cdot\mathbf{B}^{te} \quad \text{for } |t-u| = 1$$
κ_i of $\mathbf{K}$ are parametrized by $\#nb$
The $\kappa_i\beta_{ij}^{sp}$ of $\mathbf{K}\cdot\mathbf{B}^{sp}$ are parametrized by b
and the $\kappa_i\beta_{ij}^{te}$ of $\mathbf{K}\cdot\mathbf{B}^{te}$ by f
thus $\beta_{ij}^{sp} = \frac{b}{\#nb}$ or $\beta_{ij}^{te} = \frac{f}{\#nb}$

In contrast to model 1, *b* and *f* are not exact representations of β_{ij}^{sp} or β_{ij}^{te}, respectively. This is because κ_i is not 1 anymore, but set to *#nb* and thus β_{ij}^{sp} or β_{ij}^{te} doesn't simply remain *b* or *f*. As $\kappa_i\beta_{ij}^{sp}$ or $\kappa_i\ \beta_{ij}^{te}$ is parameterized by *b* or *f* and κ_i by *#nb*, β_{ij}^{sp} or β_{ij}^{te} equals *b*/#nb or *f*/*#nb*. The consequence of this retransformation is that not all β_{ij}^{sp} remain equal, because the number of adjacent and dependent pixels close to the border of the domain is smaller. Also, this model has a broader valid parameter space as shown in Figure 4.8.

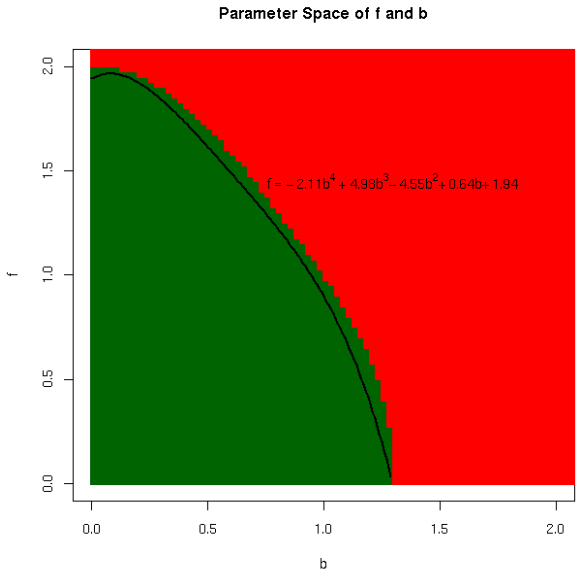

Figure 4.8: Parameter space for *f>0* and *b>0* under model 2

Valid parameter space in green and polynomial function that separates it approximately from the invalid parameter space.

This time, in order to enlarge the parameter maximally, a polynomial function of order 4 is used with the coefficients shown in the equation in Figure 4.8. As this model is used later for the real data set, the exact procedure of how the likelihood values were determined outside the green valid parameter space is described here in more detail. An if-else-statement was inserted into the function that ensures that within the green parameter space the likelihood is determined normally and outside of it a high and thus unlikely value is returned so that the search continues within the green parameter space. In order to avoid abrupt changes between the green and red parameter space, the likelihood that is returned was set to increase as larger the distance to the green parameter space gets. For every location

within the red space the closest point to the polynomial curve was determined. Then the likelihood at this point was taken and 10 times the distance was added to that likelihood value.

Model 3:

A third model is:

$$\tilde{\boldsymbol{Q}}_{tt} = \tilde{\boldsymbol{Q}}_{11},..,\tilde{\boldsymbol{Q}}_{TT} = \mathbf{K}\cdot\mathbf{B}^{sp}$$

$$\tilde{\boldsymbol{Q}}_{tu} = \mathbf{K}\cdot\mathbf{B}^{te} \quad \text{for } |t-u| = 1$$

κ_i are parametrized by $\#nb$

The $\kappa_i\beta_{ij}^{sp}$ of $\mathbf{K}\cdot\mathbf{B}^{sp}$ are parametrized by $\#nb_i \cdot b \cdot \sqrt{\frac{\#nb_j}{\#nb_i}} = b\cdot\sqrt{\#nb_i\cdot\#nb_j}$

and the $\kappa_i\beta_{ij}^{te}$ of $\mathbf{K}\cdot\mathbf{B}^{te}$ by $\#nb_i \cdot f \cdot \sqrt{\frac{\#nb_j}{\#nb_i}} = f\cdot\sqrt{\#nb_i\cdot\#nb_j}$,

thus $\beta_{ij}^{sp} = b\cdot\sqrt{\frac{\#nb_j}{\#nb_i}}$ or $\beta_{ij}^{te} = f\cdot\sqrt{\frac{\#nb_j}{\#nb_i}}$

This model is similar to model 2, but $\kappa_i\beta_{ij}^{sp}$ and $\kappa_i\ \beta_{ij}^{te}$ are not parameterized simply by *b* and *f*, but by the term above.

Again, *b* and *f* cannot be used directly but have to be transformed first. The dual parameter constraint applied for this model is the same as for model 1 (see Figure 4.7).

The R-Code for all three models can be found in Appendix 9.3.

4.2.4 Maximum Likelihood Estimation and Function optim()

Once the mean vector and the precision matrix are defined under the null and alternative hypothesis, the unknown parameters can be estimated. The unknown parameters under H_0 are: one μ for each pixel, and *b*, *c* and *f* for the precision matrix. Under H_1 there is additionally one single parameter *a* which corresponds to the change of the mean at time index t_b. For the estimation of the parameters the R-Function optim() is used.

The Newton-Raphson method as part of optim() searches the zero point of the first derivate *g´(x)* corresponding to a local maximum or minimum of the original function *g(x)*. Thereby, the first derivative *g´(x)* is approximated by a Taylor series expansion $\tilde{g}'(x_n)$:

$$g'(x) \approx \tilde{g}'(x_n) = g'(x_n) + g''(x_n)(x_{n+1} - x_n)$$

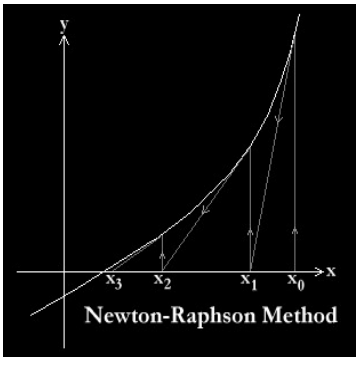

Figure 4.9: Newton-Raphson Method (Hunsley, 1997)
x_0-x_n show the points where the approximations are made.

Thus, *g´(x)* is approximated by the tangent $\tilde{g}'(x)$ at x_0.

The algorithm works as follow:

1. Start with a guess, say x_0, where the second derivate is not null.
2. At x_1 where the first tangent hits the x axis, the second approximation is made.

   This is at the point $x_{n+1} = x_n - \frac{g'(x_n)}{g''(x_n)}$

3. Repeat that step until convergence is reached.

The Newton-Raphson-method can be generalized for multivariate functions and an optimization of multiple parameters can be conducted. An approximation of a Hessian matrix is used instead of *g´´(x)*. The parameter "method" = L-BFGS-B in optim() uses the described quasi Newton-method. The parameters "lower" and "upper" allow the assignment of search boundaries (Held, 2008).

4.2.5 Likelihood Ratio Test

The likelihood ratio test compares the likelihood L of the model under H_0 and under H_1. The likelihood ratio statistic W follows asymptotically a χ_1^2 distribution as there is only one parameter more under H_1 than under H_0:

$$W = 2\log\left(\frac{L(H_0)}{L(H_1)}\right) \sim \chi_1^2$$

W can also be expressed by the log likelihood l instead of the likelihood L. Then, the likelihood ratio statistic becomes:

$$W = 2 \cdot \log\left(\frac{L(H_1)}{L(H_0)}\right) = 2 \cdot (l(H_0) - l(H_1)) = (-2l(H_0)) - (-2l(H_1)) \sim \chi_1^2$$

If W is larger than $\chi^2_{1,0.05}$, H_0 can be rejected.

In our case, the likelihood function under H_0 is:

$$L(\vec{\mu}, b, c, f) = \left(\frac{1}{2\pi}\right)^{\frac{Tn}{2}} \left|\widetilde{\boldsymbol{Q}}\right|^{1/2} \exp\left(-\frac{1}{2}\sum_{tu}\left(\vec{y}_t - \vec{\mu}_t\right)^{\mathsf{T}} \tilde{\boldsymbol{Q}}_{tu} \left(\vec{y}_u - \vec{\mu}_u\right)\right) \text{with } \mu_{it} = \mu_{it'}, \text{ but } \mu_{it} = \mu_{jt} \text{ for } i \neq j, t < t'.$$

and the log likelihood:

$$l(\vec{\mu}, b, c, f) = \frac{Tn}{2} \cdot \left(-\log\left(2\pi\right)\right) + \frac{1}{2}\log\left(\left|\widetilde{\boldsymbol{Q}}\right|\right) - \frac{1}{2}\sum_{tu}\left(\vec{y}_t - \vec{\mu}_t\right)^{\mathsf{T}} \tilde{\boldsymbol{Q}}_{tu} \left(\vec{y}_u - \vec{\mu}_u\right)$$

By multiplying the log likelihood function with -2 we get twice the negative log likelihood:

$$-2l_{H_0}(\vec{\mu}, b, c, f) = n \cdot T \cdot \log(2\pi) - \log(\left|\tilde{\boldsymbol{Q}}\right|) + \left(\vec{y} - \vec{\mu}\right)^{\mathsf{T}} \left(\tilde{\boldsymbol{Q}}_{tu}\right)\left(\vec{y} - \vec{\mu}\right) \text{ with } \mu_{it} = \mu_{it'},$$
$$\text{but } \mu_{it} = \mu_{jt} \text{ for } i \neq j, t < t'.$$

Under H_1 we get for twice the negative log likelihood function:

$$-2l_{H_1}(\vec{\mu}, b, c, f, a) = n \cdot T \cdot \log(2\pi) - \log(\left|\tilde{\boldsymbol{Q}}\right|) + \left(\vec{y} - \vec{\mu} - a \cdot \vec{d}\right)^{\mathsf{T}} \left(\tilde{\boldsymbol{Q}}_{tu}\right)\left(\vec{y} - \vec{\mu} - a \cdot \vec{d}\right),$$
$$\text{with } \mu_{it'} = \mu_{it} + a, \forall t' > t_b$$

and with $\vec{d} = \begin{pmatrix} 0 \\ \vdots \\ 0 \\ 1 \\ \vdots \\ 1 \end{pmatrix}$ where $d_1, \ldots d_{t_b} = 0$ and $d_{t_b+1}, \ldots, d_T = 1$

Thus, the likelihood ratio statistic can be calculated as:

$$W = -2l_{H_o}(\vec{\mu}, b, c, f) - (-2l_{H_1}(\vec{\mu}, b, c, f, a))$$

This W has to be compared to χ_1^2 and then the decision whether H_0 or H_1 is more probable can be made. In the used R functions of the spatial tests (see Appendix 9.3) twice the negative log likelihood is minimized which is equivalent to maximizing the likelihood.

4.2.6 Power of tests

In order to evaluate the accuracy of the maximum likelihood estimator, idealized time series with different break magnitudes were simulated under H_0 and H_1. The spatial domain consisted of 6×4 pixels. The same break was applied to every pixel. The breaks were of magnitude between 0 (no break) and 0.2. This was done for every model separately and with known parameters $\vec{\mu}$ =1, b=0.2, c=60 and f=0.1. These parameters were chosen such that the spread of the artificial time series corresponded more or less to the spread of the original time series. For all three models 100 simulations have been conducted. In the following, for all models one example under H_0 with no break and one example under H_1 with a break of magnitude 0.1 are shown (see Figure 4.10 - Figure 4.12).

Model 1

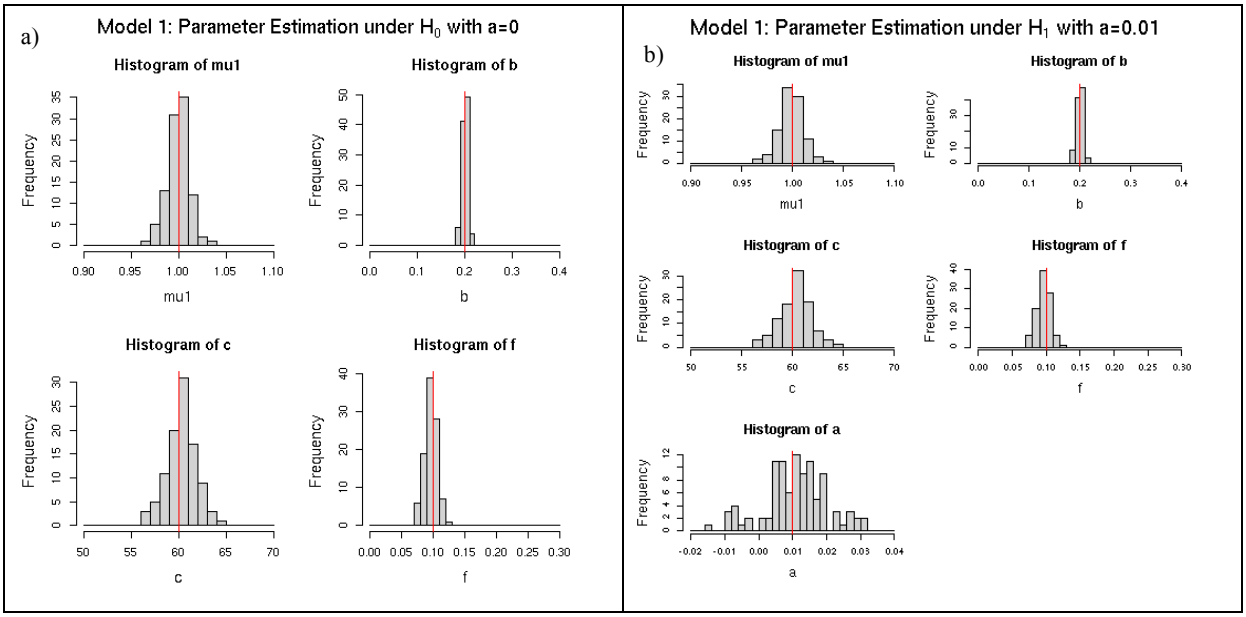

Figure 4.10: Parameter estimation with model 1

a) Parameter estimation (n=100) under H_0 and with no break (a=0).
b) Parameter estimation (n=100) under H_1 and with one break of height a=0.01.
The red lines indicate the true parameters.

Model 2

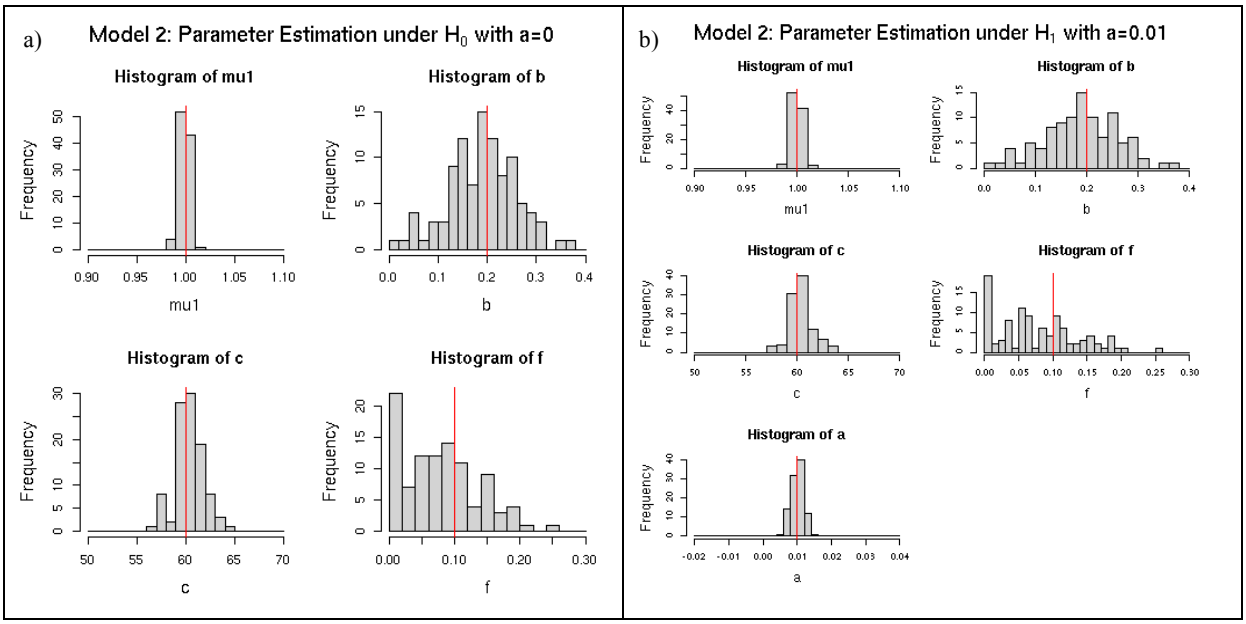

Figure 4.11: Parameter estimation with model 2

a) Parameter estimation (n=100) under H_0 and with no break (a=0).
b) Parameter estimation (n=100) under H_1 and with one break of height a=0.01.
The red lines indicate the true parameters.

Model 3

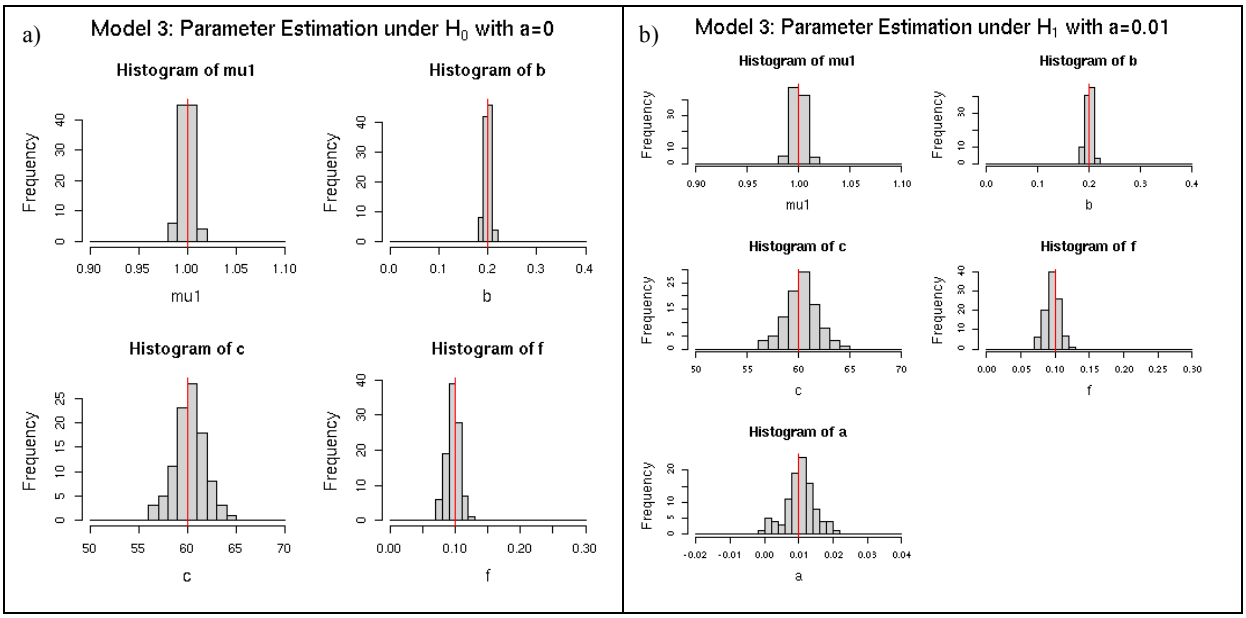

Figure 4.12: Parameter estimation with model 3

a) Parameter estimation (n=100) under H_0 and with no break (a=0).
b) Parameter estimation (n=100) under H_1 and with one break of height a=0.01.
The red lines indicate the true parameters.

Model 1 and 3 showed very similar results, especially for the parameters of the precision matrix. All simulations seemed to be normally distributed around the true parameters with a relatively low standard deviation. In model 2, the parameters *b* and *f* had higher standard deviations, but the parameter *a* (magnitude of break) was estimated more precisely. In model 2, the parameter *f* often

reached the lower boundary. This is due to the fact that the standard deviation was larger compared to the other models and the true parameter was located close to the lower parameter boundary. A parameter located in the centre of the parameter space would yield a better normal distribution of *f* and *b*. This is shown in Figure 4.13. This Figure also serves as verification that the parameter estimation under model 2 with the inserted polynomial function worked correctly close to the upper boundaries of the valid parameter space.

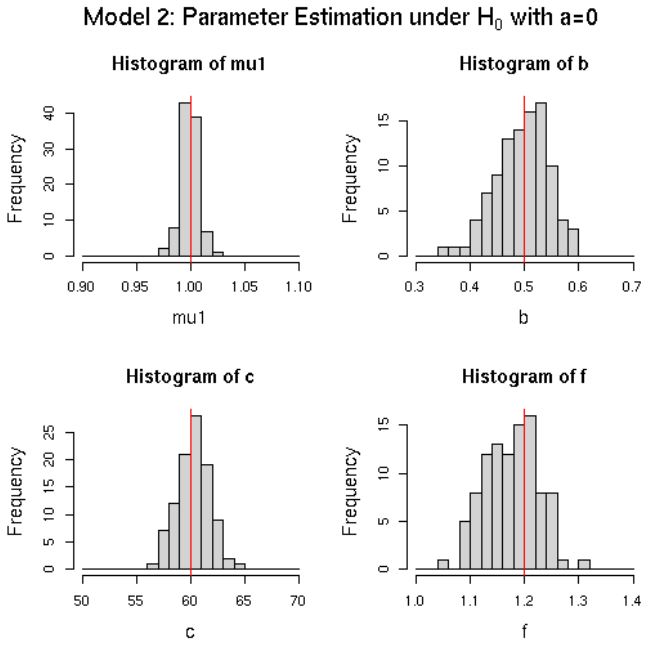

Figure 4.13: Parameter estimation with model 2 with true *b*=0.5 and true *f*=1.2

Parameter estimation (n=100) under H_0 and with no break (a=0). The red lines indicate the true parameters.

In a next step, the three models were compared to the original SNHT. The data of the above simulations were used. In Figure 4.14 the statistical power for these four different models and for different break magnitudes is presented. The statistical power is the probability that a wrong null hypothesis is rejected. As soon as there is a simulation with a break, the null hypothesis is theoretically wrong, even if the break is very small. Very small magnitudes of the breaks were not detected under all four models and thus the null hypothesis wasn't rejected. As soon as the height of the break increased, null hypotheses were rejected. In Figure 4.14 the probability of correctly rejecting the null hypothesis is given, plotted against break magnitude. For instance, with model 2 the null hypothesis was already rejected at a break magnitude of 0.009 in all 100 idealized simulations. With models 1 and 3, the null hypothesis was rejected for all 100 idealized simulations for break magnitudes of 0.045 and 0.02, respectively.

Additionally to the three models, the SNHT was evaluated with 100 idealized simulations. For the SNHT a range of ±10 months within a break should be found, was set. Note that for the SNHT no dependence structure for adjacent pixels was assumed and thus the spatial correlation was set to 0.

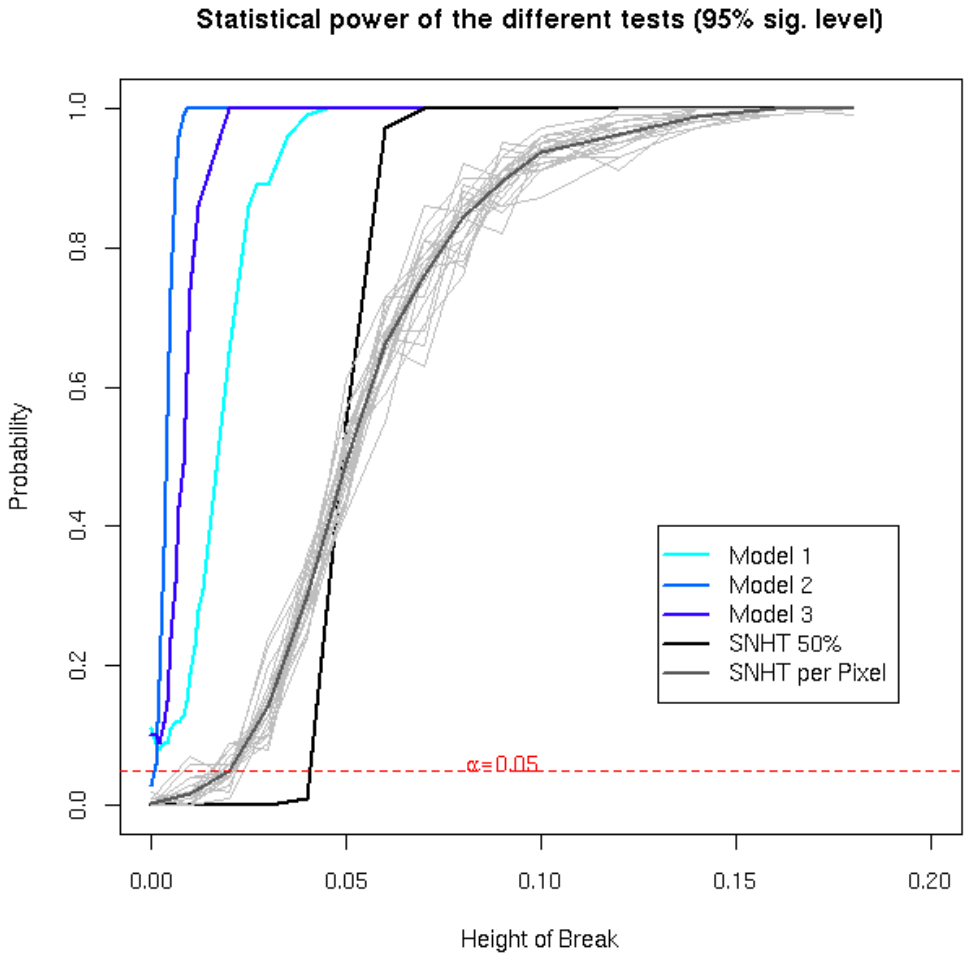

Figure 4.14: Statistical power of the different tests (95% sig. level)

The red line indicates the type I Error for model 1-3. The SNHT 50% was calculated as follows: If for one simulation, 12 or more pixels out of the 24 had a significant break, the simulation was considered to be significant. This was done for all 100 simulations and then the number of significant simulations was divided by 100. The SNHT per pixel shows for each of the 24 pixels the probability that the null hypothesis was correctly rejected.

With a 95% significance level, the null hypothesis of a break of magnitude 0 should be rejected in 5% (red line) of the cases (type I Error). As there are only 100 simulations, this was not exactly true for model 1-3. It is however visible that the alpha Error for the SNHT was about 0% and not 5% as expected. This means that the decision never fell for H_1 and H_0 was not rejected 5 times. This can be explained. The SNHT wrongly rejects the null hypothesis in 5% of the cases, however not necessarily between the ±10 defined months but rather somewhere within the whole time period. Hence, the probability that the SNHT finds the (wrong) break within the given range of ±10 months is much smaller than 5%.

Figure 4.15 shows the same issue but with a 90% significance level.

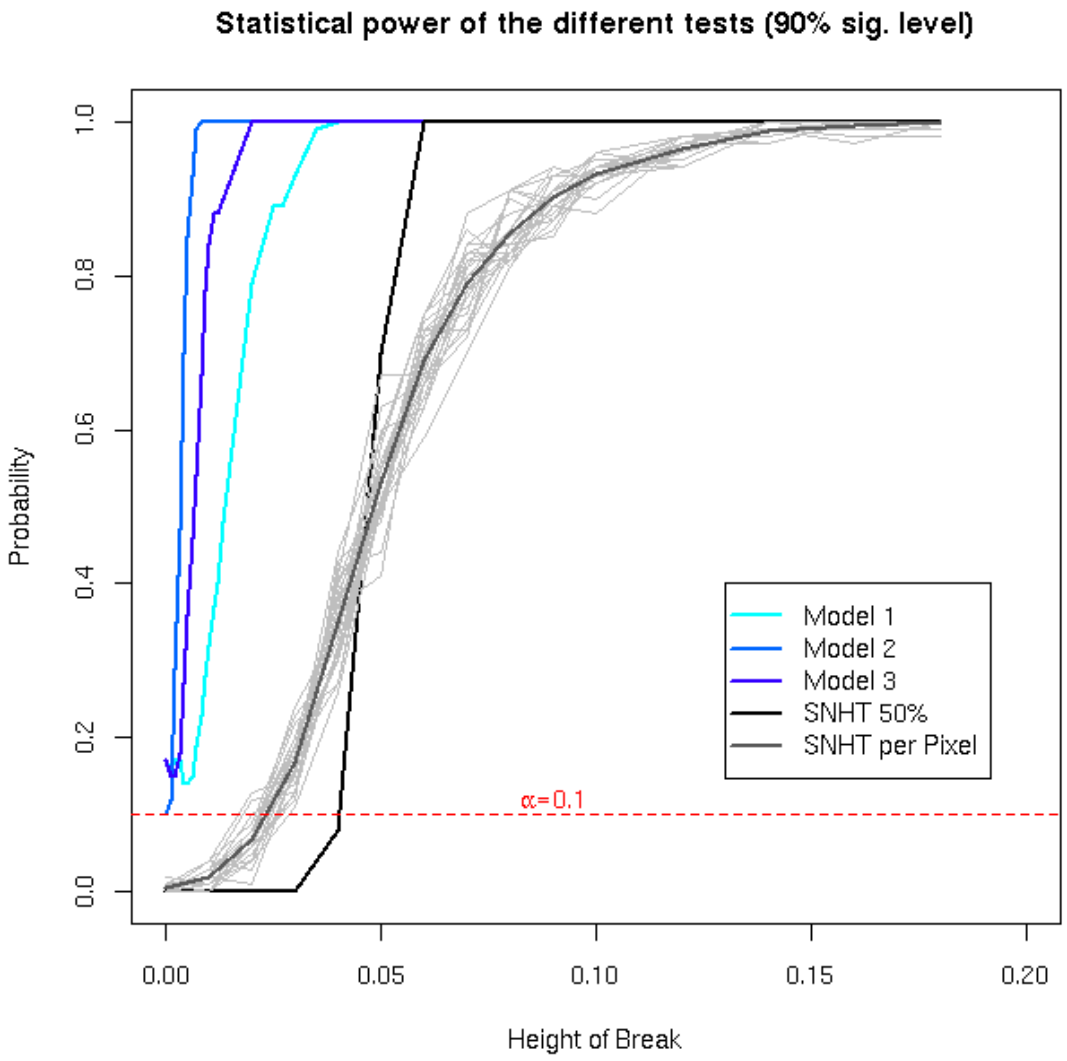

Figure 4.15: Statistical power of the different tests (90% sig. level)

The red line indicates the type I Error for model 1-3. The red line indicates the alpha Error. The SNHT 50% was calculated as follows: If for one simulation, 12 or more pixels out of the 24 had a significant break, the simulation was considered to be significant. This was done for all 100 simulations and then the number of significant simulations was divided by 100. The SNHT per pixel shows for each of the 24 pixels the probability that the null hypothesis was correctly rejected.

These diagnostic results demonstrate that the newly developed spatial test was suitable to find smaller breaks than the SNHT. Model 2 was the most sensitive model; it found breaks with half the magnitude than the other two models. Since it also estimated the most important parameter, namely the height of the break most appropriately, model 2 will be used for testing the real data set in the next section.

4.3 Results

In this chapter, a new spatial homogeneity was presented. The difference to the SNHT was that the spatial and temporal correlation structure was included and that a whole region instead of single pixels was tested. The accuracy of the spatial homogeneity test was explored with idealized time series and three different models. Model 2 was chosen to be used for further investigations with the real data set, because it was most sensitive and has estimated the parameter *a* most accurately.

In this section, the results of the application of the spatial homogeneity test are shown.

The test was applied to 6 regions. The regions were chosen in a way that different patterns could be investigated. In Figure 4.16 the result of the SNHT and the investigated regions for the spatial test are shown. A region with no break was taken, one with the same break for each pixel and one with different breaks. Additionally, interesting regions over the desert, the Alps and over France were tested. Input data were the Q-Series. The coordinates and number of pixels of these six regions are given in Table 4.1.

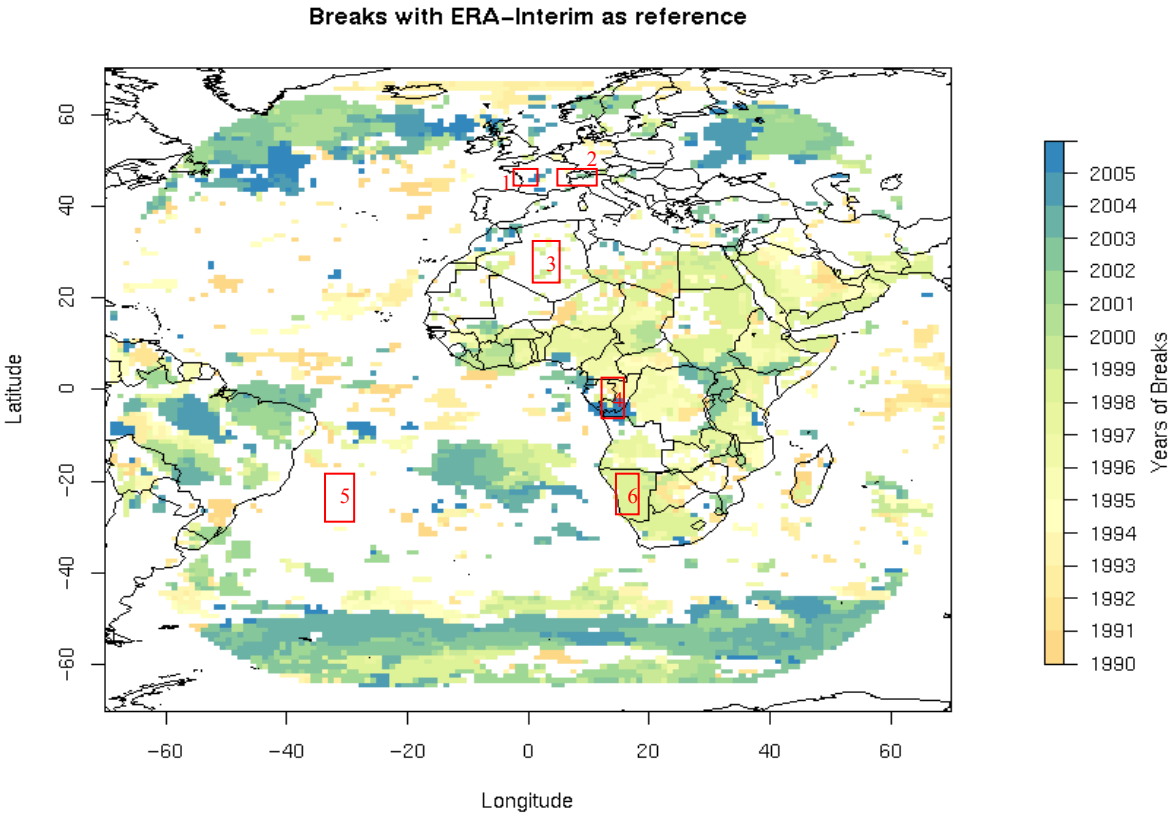

The rectangular boxes show the regions that were chosen for investigations with the spatial homogeneity test.

Region	Coordinates	Number of pixels
1	45-47°N / 0-2°E	9
2	46-47°N / 6-10°E	10
3	27-30°N / 2°W-2°E	20
4	66-63°S / 12-14°E	12
5	42-40°S / 34-32°W	9
6	42-40°S / 16-18°E	9

Table 4.1: Six chosen regions

The coordinates as well as the number of pixels of each region are given.

In the following, the results for each region are shown. More exactly, the likelihood ratio statistic W was plotted at each month between 1990 and 2005.

$$W = 2 \cdot \log\left(\frac{L(H_1)}{L(H_0)}\right) = 2 \cdot (l(H_0) - l(H_1)) = (-2l(H_0)) - (-2l(H_1)) \sim \chi_1^2$$

The red line corresponds to the 95%-significance level of the χ_1^2-distribution with Bonferroni correction. This correction was applied because of the multiple testing problem. As there are 192 tests and a 95%-significance level, approximately 10 incorrectly rejected null hypotheses are expected. As the Bonferroni correction is very conservative, only large breaks are significant.

As in the SNHT, if a break occurred in the first or last ten months of the time series it was ignored.

Further, the T-Series of the SNHT are plotted for each pixel in the region (gray lines) as well as for the mean of the whole region (black lines). In addition, a plot with the Q-Series, the estimated and true Q-Series difference at the break and the true height of the break in W/m^2 is given. The true height of the break was derived by subtracting the mean of the absolute global radiation in W/m^2 after the break from the mean of the absolute global radiation in W/m^2 before the break.

Region 1

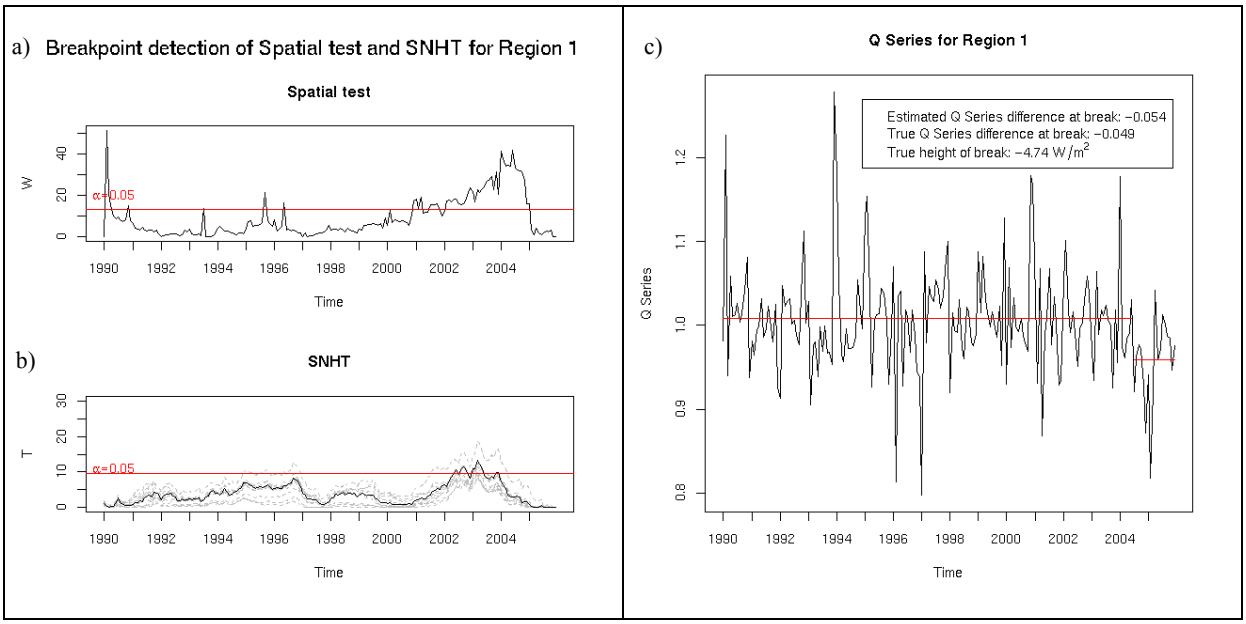

Figure 4.17: Comparison of Spatial test and SNHT for region 1

a) Result of spatial test. The red line corresponds to the significance level α=0.05 of the χ_1^2 -distribution after Bonferroni correction. b) Result of SNHT. The red line corresponds to the critical level α=0.05 of the SNHT (obtained by simulation of random normal numbers). c) Q-Series with means for and after the break (red lines). The true height of break is the difference between the absolute mean global radiation in W/m^2 before and after the break.

Estimated parameters at break:

$\bar{\mu}$ = (1.0077, 1.0073, 1.0070, 1.0093, 1.0093, 1.0107, 1.0080, 1.0085, 1.0083)

b = 1.2509 , c = 108.0017, f = 0.2004, a = -0.0539

Region 2

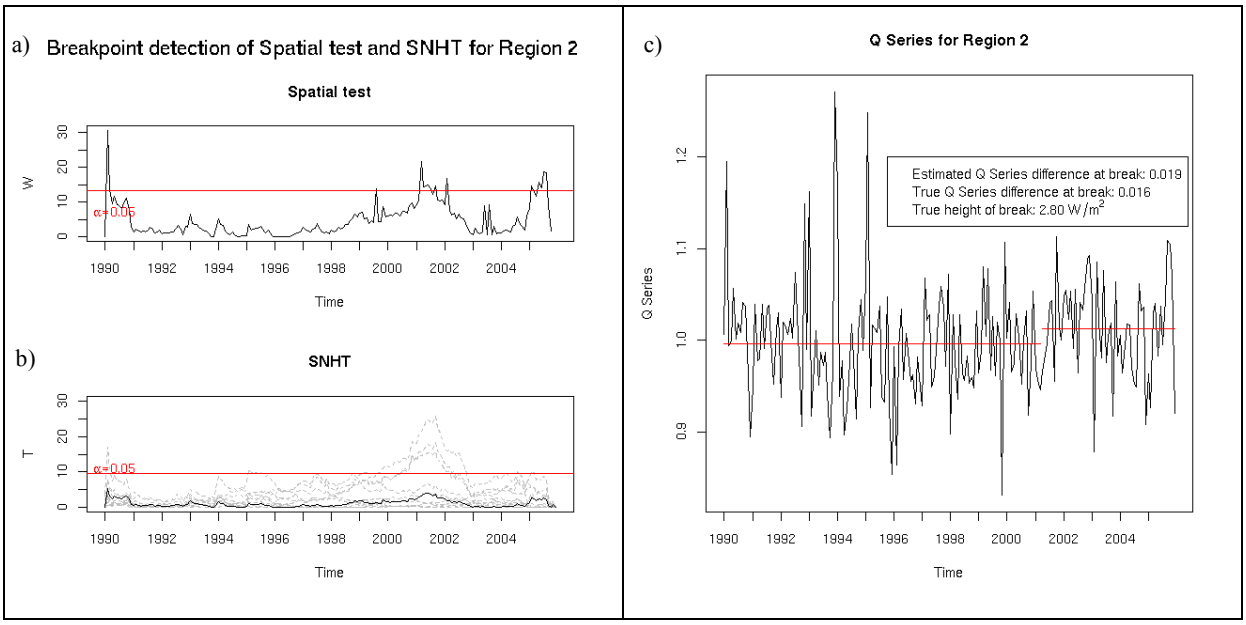

Figure 4.18: Comparison of Spatial test and SNHT for region 2

a) Result of spatial test. The red line corresponds to the significance level α=0.05 of the χ_1^2 -distribution after Bonferroni correction. b) Result of SNHT. The red line corresponds to the critical level α=0.05 of the SNHT (obtained by simulation of random normal numbers). c) Q-Series with means before and after the break (red lines). The true height of break is the difference between the absolute mean global radiation in W/m^2 before and after the break.

Estimated parameters at break:

$\vec{\mu}$ = (0.9950, 0.9947, 0.9940, 0.9941, 0.9941, 0.9976, 0.9990, 0.9982, 0.9964, 0.9949)

b = 1.29, c = 74.9998, f = 0.0357, a = 0.01943

Region 3

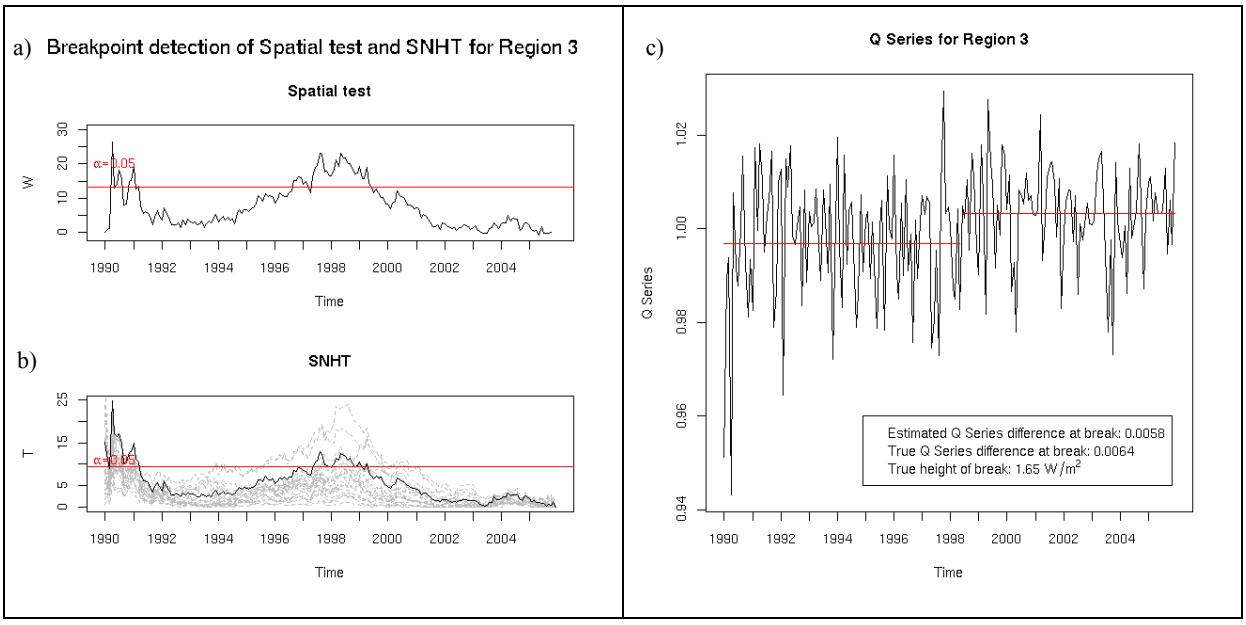

Figure 4.19: Comparison of Spatial test and SNHT for region 3

Same as in Figure 4.18 but for region 3.

Estimated parameters at break:

$\bar{\mu}$ = (0.9971, 0.9971, 0.9972, 0.9973, 0.9974, 0.9972, 0.9972, 0.9972, 0.9973, 0.9974, 0.9973, 0.9973, 0.9973, 0.9973, 0.9974, 0.9974, 0.9974, 0.9974, 0.9974, 0.9974)

b = 1.2822, c = 684.9978, f = 0.0649, a = 0.0058

Region 4

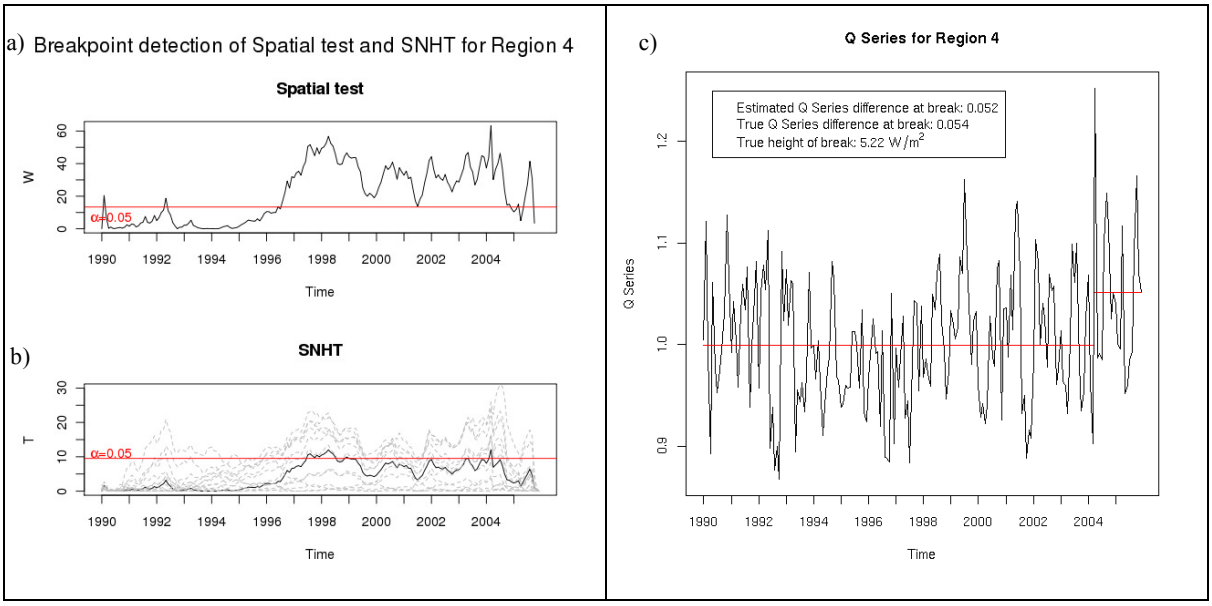

Figure 4.20: Comparison of Spatial test and SNHT for region 4

Same as in Figure 4.18 but for region 4.

Estimated parameters at break:

$\bar{\mu}$ = (0.9993, 0.9996, 0.9987, 1.0005, 0.9993, 0.9980, 0.9984, 0.9979, 0.9973, 0.9980, 0.9979, 0.9974)

b = 1.2708, c = 100.0006, f = 0.1203, a = 0.0541

Region 5

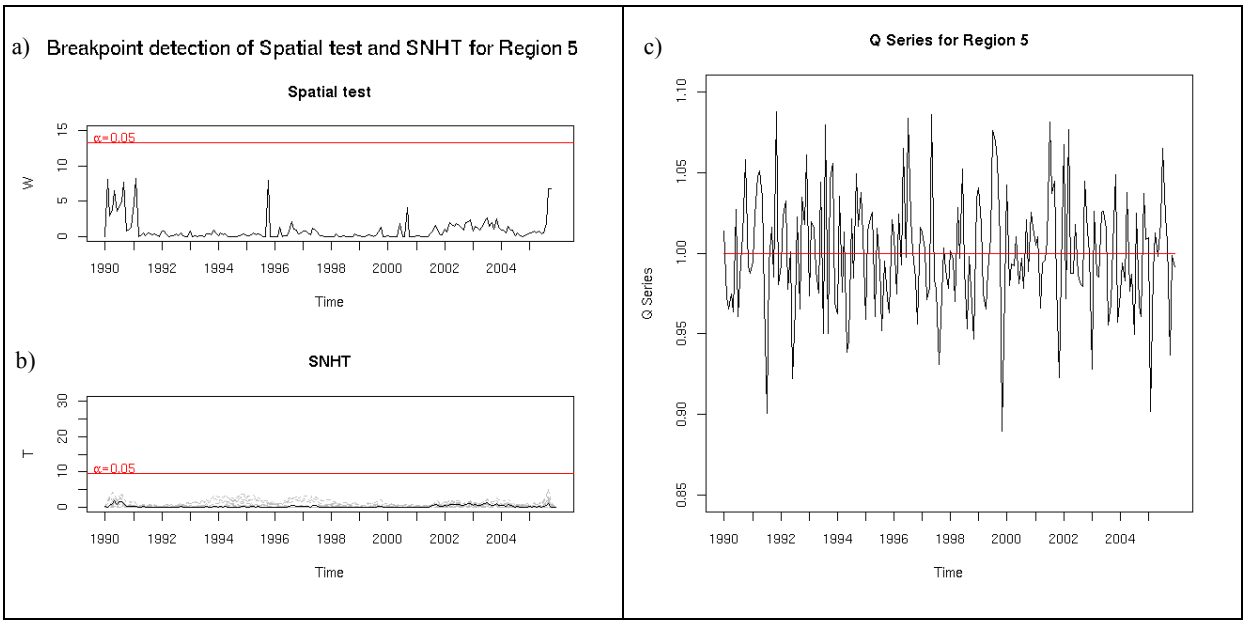

Figure 4.21: Comparison of Spatial test and SNHT for region 5

Same as in Figure 4.18 but for region 5

Estimated parameters under H_0:

$\vec{\mu}$ = (0.9995, 0.9997, 0.9998, 0.9997, 0.9997, 0.9998, 0.9997, 0.9996, 0.9995)

b = 1.2805, c= 176.0012, f = 0.0789

Region 6

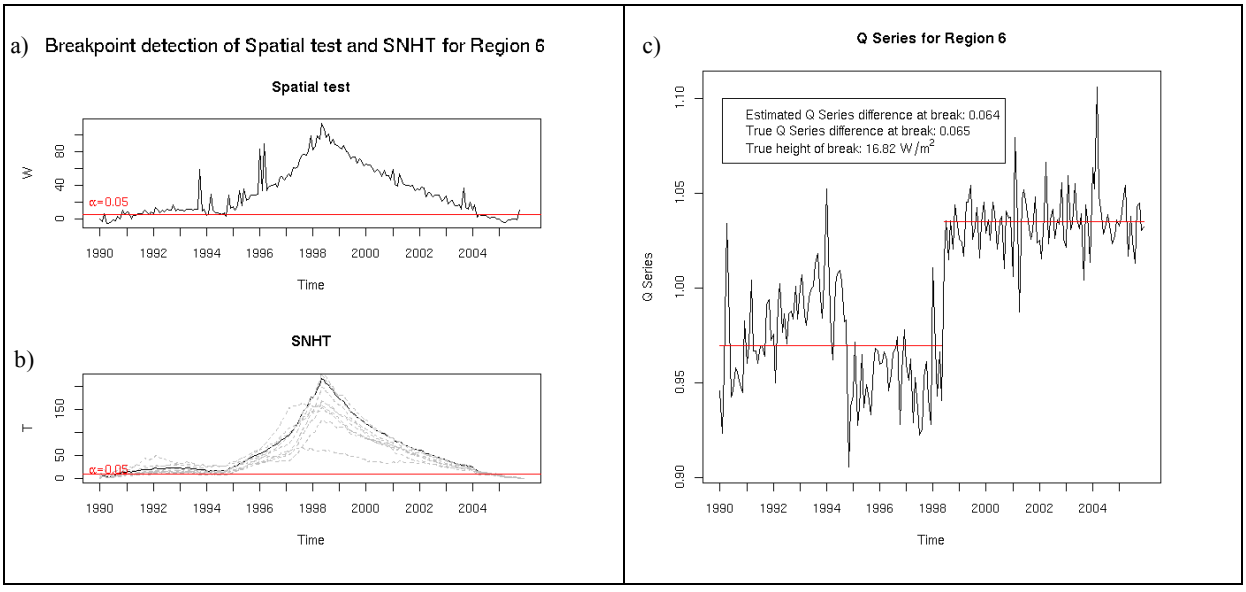

Figure 4.22: Comparison of Spatial test and SNHT for region 6

Same as in Figure 4.18 but for region 6

Estimated parameters at break:

$\vec{\mu}$ = (0.9698, 0.9702, 0.97024, 0.9701, 0.9703, 0.9701, 0.9702, 0.9702, 0.9700)

b = 1.1273, c = 193.0074, f = 0.6027, a = 0.0640

For all 6 regions, very similar break patterns were found by the spatial test and the SNHT. The highest *W*- and *T*-values in one and the same region mostly occurred in the same months and were significant in both tests. Region 6 showed the highest *W*- and *T*-values. This was due to the large differences in the time series of the satellite and ERA-Interim data set. For this time series, a model H_1 that suggests one break is not adequate, because clearly two breaks and a trend are visible in Figure 4.22.

From the width of the highest peak, the domain of uncertainty is readable. For example for region 1, where the highest *W*-values occurred in the middle of 1998, the uncertainty approximately amounted ± 12 months.

The MGMRF was specified through its full conditionals and expectation and precision were:

$$\mathrm{E}\left[y_{it}\,|\,\vec{y}_{-it}\right] = \mu_{it} + \beta_{ij}^{sp}\sum_{j:i\sim j}\left(y_{jt}-\mu_{jt}\right) + \beta_{ij}^{te}\sum_{u:t\sim u}\left(y_{iu}-\mu_{iu}\right)$$

$$\mathrm{Prec}(y_{it}\,|\,\vec{y}_{-it}) = \kappa_i > 0$$

κ_i is the precision and was parameterized by *#nb·c* in model 2. The variance is then $\tau^2 = \frac{1}{\kappa_i}$. The other two parameters of the precision matrix were *b* and *f*. Again, as model 2 was used, *b* and *f* have to be divided by *#nb* in order to get the true spatial and temporal β_{ij}, respectively. As seen in the equations above, the β_{ij} represent the weights of the influence of the dependent adjacent pixels.

For all regions *b* and *f* were very close to the border of the valid parameter space. The parameter *b* that stands for the spatial correlation structure was mostly characterized by very high values. This indicates that spatially adjacent pixels had a high weight. In contrast, the parameter *f* had low values (except for region 6) which means that the temporal correlation structure was less distinctive. The reason for the high value of parameter *f* in region 6 might be due to the very inhomogeneous Q-Series. As a model with only two means is not appropriate, the temporal parameter *f* has to adjust for the large difference towards the two means and thus becomes large.

The plot of the Q-Series shows that the found breaks make sense. In each plot, the estimated and true Q-Series difference is indicated. This difference was estimated by maximum likelihood estimation (parameter *a*), and was also calculated. The point in time of the break was known and thus the mean values of the Q-Series before and after the break could be determined. A comparison of these two values showed that they were for all six regions very close to each other. This illustrates that the maximum likelihood procedure estimated the height of the break well.

Additionally, the true height of the break is indicated in each figure, expressed in W/m^2. That one was calculated in the following way: The difference of the absolute SIS of the test (satellite data record) and reference (ERA-Interim data set) series before and after the break was determined and then the difference of these two values was calculated.

In the spatial test, the influence of breaks of single pixels was reduced. Only breaks that occurred in a larger area were detected by the spatial homogeneity test and breaks of single pixels were ignored. This gives a more homogenous image of breaks.

Still, in different regions, different points in time of the breaks were found. This indicates that the breaks didn't occur because of replacements of satellites. If the breaks appeared at a satellite replacement, they should arise within the same time period over the whole visible disc.

4.4 Discussion

This section discusses the two research questions that were introduced in section 4.1.

The first part of this discussion treats the question whether it is possible to create a homogeneity test that is more powerful than the SNHT with the use of the information of spatially adjacent pixels.

The simulation of idealized time series showed that the maximum likelihood procedure accurately estimated all unknown parameters. All parameters varied around their true values. Especially the parameters $\bar{\mu}$ and a had a low variance in the simulation data set. On the other hand, also the means and the height of the break of the Q-Series of the real data were estimated very accurately. This was proven by calculating the true means of the corresponding Q-Series and the true height of the break at a given point in time and by comparing it to the corresponding values obtained by the maximum likelihood estimation.

A visual inspection of the Q-Series also validates the correct estimation of timing for the detected breaks. The comparison with the original SNHT demonstrates that both tests gave very similar results. These results are evidence that the spatial test worked correctly.

The new spatial homogeneity test found breaks with lower magnitudes compared to the original SNHT. This was visualized in Figure 4.14 and in Figure 4.15 where the statistical power of both tests was investigated. This is further affirmed by comparing the *W*- and *T*-Series of the real data set; they basically show the same course, but much more *W*-values than *T*-values were significant.

By testing a whole region, the influence of a break in a single pixel is reduced. This is desirable as the SNHT gave a lot of different breaks, even for adjacent pixels. For our climate data record, the result of the spatial homogeneity test is more useful because the focus is laid on breaks that are significant over a larger region.

On the one hand, it is desirable that the spatial test discovers breaks with low magnitudes because even if a break is of small magnitude, it might be important if it occurs in a spatially consistent pattern. On the other hand, it is also obvious that a break must be of a certain magnitude that justifies a homogenization procedure. The uncorrected χ^2 was not a good measure to decide when a break is significant or not, because it almost always rejected the null hypothesis. Therefore, a Bonferroni-correction was applied in order to reduce the increased type I Error that occurred due to multiple testing.

However, several aspects have to be considered before correcting breaks in a climate data record.

The magnitude of a break should always put in relation to the absolute magnitude of SIS at a specific location. For locations with a high irradiance, a break of a given magnitude has a smaller influence than for locations with low values of SIS. Thus, not only the difference in the Q-Series, but also the difference in the absolute and relative height of the shift should be considered.

Further, the requested accuracy threshold of 15 W/m^2 and the optimal accuracy requirement of 8 W/m^2 of the satellite climate data record should be kept in mind. Special attention should be given to breaks that exceed the threshold of 8 W/m^2 or even 15 W/m^2.

The second question was whether it is justified to homogenize the climate data record. As the data set is derived by different satellites, breaks at more or less the same points in time are expected, namely at the periods of satellite replacement. However, the breaks were very inhomogeneous and did not appear at satellites replacements. Additionally, there are no other justified reasons for the appearance of the different breaks. Satellite changes would cause a high and consistent break and this one would be visible in the SNHT as well as in the spatial test. Furthermore, the methodology that was used to generate the climate data record included a self-calibration procedure that is supposed to take care of calibration changes from one satellite to the next. This is an explanation why no breaks were found at satellite replacements. Therefore it is difficult to decide whether and especially how the breaks should be corrected. For instance, in the case when breaks are discontinuous in space, does the homogenization only have to be applied over regions with significant breaks? Shall the homogenization be unified for climatologically similar regions like ocean and land or tropics, subtropics and temperate climate zones? Several questions arise from the development of this new spatio-temporal homogeneity test that need to be answered before a homogenization is carried out.

It must be noted that both, the SNHT and the spatial test, find breaks of relatively low magnitudes compared to the absolute mean SIS. In the investigated regions, the height of the break, expressed in W/m^2 was on the order of few percentages or per mills compared to the absolute mean SIS. For instance, the annual variation of SIS at different locations of the visible disc of MeteoSat was investigated in my semester thesis (Schibli, 2011). In the Subtropics for example the annual variation of the absolute SIS amounts to 200 W/m^2. Even at the equator the annual variation reaches 50 W/m^2 (Schibli, 2011, Section 3.2). In addition, the absolute height of the break only exceeded in region 6 the requested accuracy threshold of 15 W/m^2. The height of the break was slightly higher, namely 16.82 W/m^2. For all other regions the absolute height of the break expressed in W/m^2 was well below that threshold.

Another reason for not homogenizing the satellite data set is that the reference data set is model based and may also contain inhomogeneities. For the calculation of global radiation in the ERA Interim data set, among other, also satellite data was used. It is possible that satellite replacements have an influence on the quality of the ERA Interim data set and cause breaks in the reference data record. The reason for the use of this reference data record was its full coverage of the whole visible disc of Meteosat. As mentioned above, ground stations are absent in many parts of the globe. Hence, it is difficult to say which of the two data records, satellite or Re-Analysis, is more correct. However, when measured and compared in absolute SIS, both data sets had very similar time series and trends.

Due to these reasons the data set has not been corrected. Also WMO (2011) stated that one has to bear in mind that independent attempts at homogenization may easily result in quite different data and that the adjusted data shouldn't be considered as absolutely correct nor should the original data always be considered as wrong.

5 Relations of global radiation with large-scale climate variability phenomena

In this chapter, the relation of SIS as well as of CI with two large-scale variability phenomena, namely El Niño Southern Oscillation (ENSO) and North Atlantic Oscillation (NAO), is investigated. In the first section, a short overview of these two oscillations is given and the research gaps and research questions are introduced. Then, a separate section for ENSO and NAO follows where the relationship between these oscillations and SIS, CI, temperature and precipitation is investigated. Each of these sections contains a methods, results and discussion part.

5.1 Overview of ENSO and NAO and research questions

5.1.1 El Niño Southern Oscillation

The El Niño Southern Oscillation is the strongest known natural climate variability and can last from some months to several years. In the context with the ENSO phenomenon usually three different states are differentiated: the neutral period, the El Niño and the La Niña period. While the ENSO phenomenon mainly occurs in the Pacific, it can affect the global climate system, specifically the sea-level pressure, sea-surface temperature, sea-level height, surface wind and the ocean sub-surface temperature (Dijkstra, 2006).

The neutral state of ENSO is characterized by unequal air pressures over the eastern Pacific at the South American coast (high) and the western Pacific between Australia and Indochina (low). At the same time, the low sea-surface temperatures in the eastern Pacific and the relatively high temperatures in the western Pacific stabilize this pressure distribution. Trade winds from east to west are a further component of this ocean-atmosphere-system. They compensate for the pressure gradient. In higher layers the wind blows in the opposite direction. These wind patterns are also known as the so-called Walker Circulation. The surface water is driven westwards through trade winds which causes a decline in the sea-level height in the eastern Pacific and an increase in the western Pacific. The upwelling cold water in the eastern Pacific supports a thermal high pressure system. A result of the absence of precipitation in these areas are for instance deserts at the west coast of South America. The neutral period of ENSO is summarized in Figure 5.1.

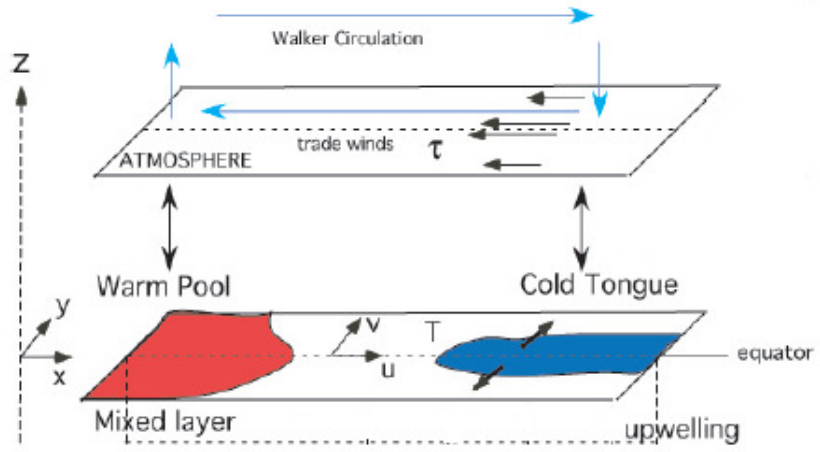

Figure 5.1: Neutral state of ENSO (adapted from Dijkstra, 2006)

A cross section of the ocean-atmosphere-system between Indonesia and South America during the neutral phase of ENSO is shown. The Walker circulation with its corresponding wind patterns and cold and warm water layers are visible.

The El Niño period is characterized by an increase in the sea-level pressure over the western Pacific and a decrease over the eastern Pacific. As a consequence the trade winds diminish and both the sea level and the water temperatures at the west coast of South America rise. In the extreme case of El Niño the Walker circulation can reverse.

During La Niña periods all phenomena of the neutral state are intensified and therefore the Walker circulation increases in strength. Further, the water temperatures are higher and the precipitation is stronger in the western Pacific and the inverse is true for the eastern Pacific (Trenberth, 1991, van Loon and Shea, 1985).

Many studies have been conducted on the influence of ENSO on the weather patterns in South America, Asia, Australia and North America (Ropelewski and Halpert, 1986, Rasmusson and Carpenter, 1983, Alexander et al., 2009). Several authors have also studied the impact of ENSO in Europe and Africa. Their results are interpreted together with the results of the analysis of this thesis.

5.1.2 North Atlantic Oscillation

The NAO is a meridional oscillation in the Atlantic Ocean and is defined as the difference of the normalized sea level pressure anomaly between Iceland and the Azores (Hurrell et al., 2001). The positive phase of NAO is characterized by a strengthening of the Iceland low and the Azores high. On the other hand, the negative phase has both a very weak Iceland low and Azores high (Portis et al., 2000).

During the positive phase of NAO, there is more precipitation over northern Europe and Scandinavia. In contrast, during the negative phase, more precipitation is observed over southern Europe, the Mediterranean and North Africa (Hurrell, 1995).

The NAO further has also significant effects on the European temperatures. Between 1940 and 1970, when the NAO had a downward trend, winter temperatures were lower than normal. This period was followed by an upward trend in the NAO index. In the eighties, the NAO remained constantly in the positive phase in winters contributing to significantly warmer winters in Europe (Hurrell, 1995).

Other characteristics of the NAO are:

- Low sea surface temperatures during NAO+ in the Atlantic Ocean at the west coast of Africa and in the east and northeast of Greenland.
- Movement of the extra tropical cyclones that cause more storms over Iceland and northern Europe during NAO+ and a slight increase in storms over southern Europe.

The NAO phenomena are more pronounced in wintertime (Hurrell, 1995).

The situation of the negative and positive NAO phase is summarized in Figure 5.2.

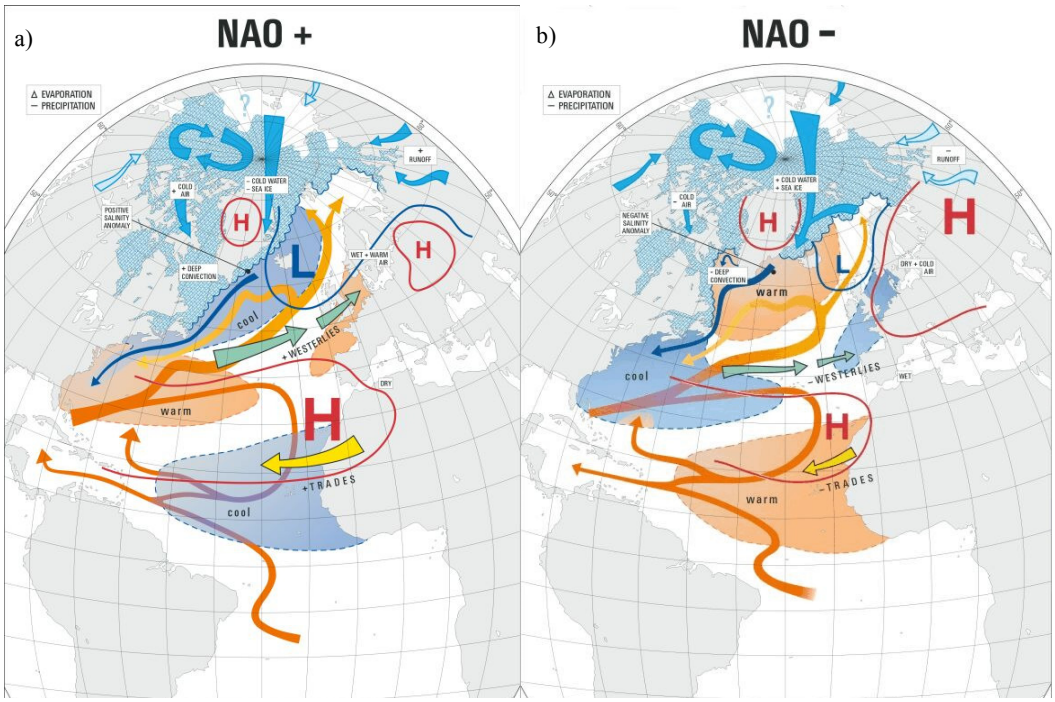

Figure 5.2: Positive and negative phase of NAO (Wanner et al., 2001)

a) NAO+ with a strengthening of the Iceland low and the Azores high
b) NAO- with a weak Iceland low and Azores high

Many studies have been conducted in order to investigate the impact of NAO on the European weather, among other Hurrell and Van Loon (1997), Wanner et al. (2001) or Hurrell et al. (2003).

5.1.3 Research gaps and research questions

As mentioned above, the impacts of the two different oscillations on the weather are well explored. For instance, the impacts of ENSO have been studied by Ropelewski and Halpert (1986), Rasmusson and Carpenter (1983) or by Rasmusson (1983). On the other hand the NAO was investigated among other by Hurrell (1995) or Wanner (2001). Thus, general weather patterns of these oscillations are quite well known, especially in specific regions, and the influence on precipitation and temperature is well established. However, especially for ENSO, only few studies over Europe and Africa have been conducted (Brönnimann, 2007, Toniazzo and Scaife, 2006). In addition, only very few studies investigated the relations between the large-scale climate variability phenomena and SIS or CI, respectively. With the CM SAF climate data record it is possible to conduct spatially gap-free investigations of the relation between these climate phenomena and observed (not modelled) SIS or CI and thus to complement previous studies. Therefore, the research questions that are discussed in this chapter are:

- Is it possible to detect statistically significant climate-related patterns in the satellite-based data record by use of correlation analysis and analysis of variance between large-scale climate variability indices and SIS (or CI)?
- What are the physical explanations for the patterns revealed by above analysis and how coherent are these patterns to what was found in similar studies for temperature and precipitation?

These two research questions are treated separately for each oscillation in the corresponding sub-sections.

At locations where the weather patterns are known, the behaviour of CI and SIS can easily be assumed, because precipitation is highly correlated with CI and that one correlates negatively with SIS. SIS is further linked to surface temperature. However, these relationships are not linear and no studies have examined them with a spatio-temporally continuous satellite-based climate data record.

In addition to the two mentioned large-scale climate variability phenomena also the Pacific/North American Oscillation (PNA) was investigated. As the investigations for the PNA were done in less detail than for ENSO and NAO, an overview of the PNA as well as of the conducted analyses are in Appendix 9.4.

5.2 El Niño Southern Oscillation

5.2.1 Methods

In Figure 5.3 the course of the monthly El Niño Southern Oscillation Index between 1983 and 2005 is presented. Positive and negative ENSO years and months are well visible. A more detailed allocation to positive, neutral and negative months is given later in this section (Table 5.1).

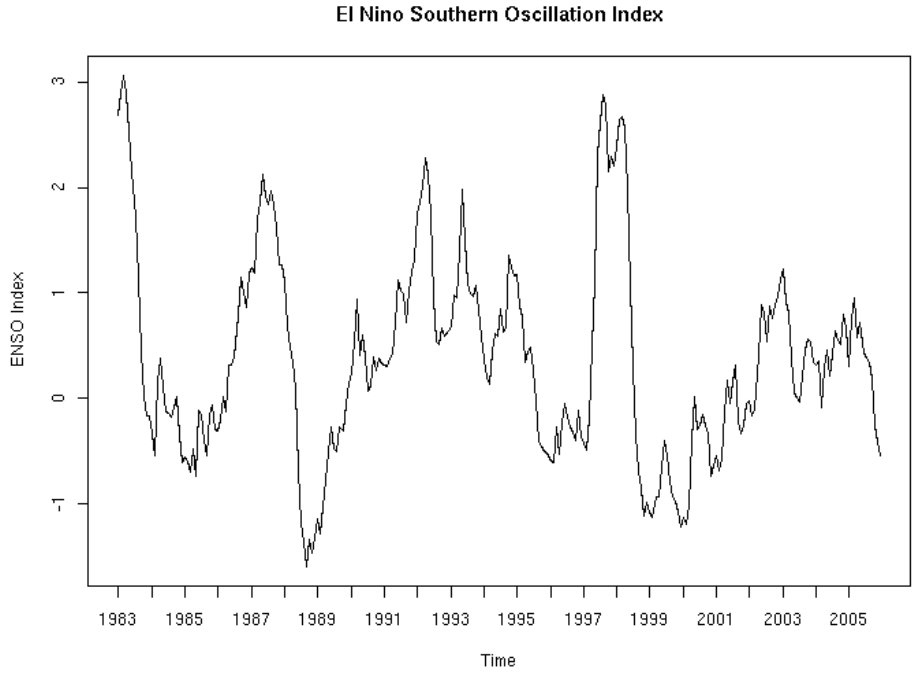

Figure 5.3: El Niño Southern Oscillation Index

Course of ENSO Index between 1983 and 2005.

In the results section for the El Niño Southern Oscillation, patterns with distinctive characteristics of SIS and cloudiness during El Niño and La Niña phases have been identified. For each of these patterns the differences between the positive, neutral and negative phase of ENSO have been compared. Each month between 1983 and 2005 was allocated either to a positive, neutral or negative phase. The allocation was based on Null (2011). He allocated all months with an index that was between -0.5 and 0.5 to the neutral phase, the months with an index higher than 0.5 to a positive and lower than -0.5 to a negative phase. Table 5.1 summarizes the positive, neutral and negative phases of ENSO.

Positive phase	Neutral phase	Negative phase
Jan 83 – Jun 83	Jul 83 – Sep 84	Oct 84 – Sep 85
Aug 86 – Feb 88	Oct 85 – Jul 86	May 88 – May 89
May 91 – Jul 92	Mar 88 – Apr 88	Sep 95 – Mar 96
May 94 – Mar 95	Jun 89 – Apr 91	Jul 98 – Jun 00
May 97 – Mai 98	Aug 92 – Apr 94	Oct 00 – Feb 01
May 02 – Mar 03	Apr 95 – Aug 95	
Jun 04 – Mar 05	Apr 96 – Apr 97	
	Jun 98	
	Jul 00 – Sep 00	
	Mar 01 – Apr 02	
	Apr 03 – Mai 04	
	Apr 05 – Dec 05	

Table 5.1: Positive, neutral and negative ENSO-phases

The positive phase includes 85, the neutral 130 and the negative 61 months.

These three phases were compared with one-way ANOVA and pairwise T-Tests for independent groups and boxplots are presented. The positive phase included 85 months, the neutral phase 130 months and the negative phase 61 months. In the following, a short overview of the one-way ANOVA and the T-Test for independent groups is given.

The model of a one-way ANOVA is given by:

$$Y_{ij} = \mu + A_i + \varepsilon_{ij}, \ \sum A_i J_i = 0$$

This model describes the relationship between treatment and response. Y_{ij} represents the j-th $(1,\ldots,J_i)$ observation in the i-th treatment group (here i=1,2,3). μ is the overall mean and A_i the i-th treatment effect. A necessary constraint is $\sum A_i J_i = 0$. It is further assumed that the errors are normally and independently distributed: $\varepsilon_{ij} \sim N(0,\sigma^2)$ iid.

The null and alternative hypotheses are:

H_0 : all $A_i = 0$
H_1 : at least one $A_i \neq 0$

Since $\varepsilon_{ij} \sim N(0,\sigma^2)$, $F=\frac{MS_{treat}}{MS_{res}}$ (the ratio of the treatment and residual mean square) has under H_0 a F-distribution with I-1 and N-I degrees of freedom. I is the total number of groups (here 3) and $N = \sum J_i$. Thus, the null hypothesis can be rejected if $F > F_{1-\alpha,I-1,N-I}$ (see for example Sachs and Hedderich (2006)).

The test statistic for the T-Test for two independent groups A and B is:

$$t = \frac{\bar{X}_A - \bar{X}_B}{\sqrt{\frac{\mathrm{var}(A)}{N_A} + \frac{\mathrm{var}(B)}{N_B}}}$$, where $\bar{X}_A$ and $\bar{X}_B$ are the means of the two groups.

The null and alternative hypotheses for the T-Test for independent groups are:

$$H_0 : \bar{X}_A = \bar{X}_B$$
$$H_1 : \bar{X}_A \neq \bar{X}_B$$

If $|t| > t_{1-\alpha,df}$, the null hypothesis is rejected. It is assumed that *A* and *B* are independent and normally distributed and that they have equal variances (see for example Sachs and Hedderich (2006)).

For the pairwise comparisons, Bonferroni correction (p-values are multiplied with the number of comparisons) was applied. It was used, because Bonferroni correction is conservative and thus only true differences are detected. The model assumption, namely normal distribution and homogeneity of variance, were mostly fulfilled.

Additionally, one strong El Niño year (97/98), one strong La Niña year (88/89) and a neutral year (96/97) were compared. For each of these events the months from June to May in the following year were taken as then the event was strongest for both, El Niño and La Niña. In this time period, El Niño was strongest in August and September and La Niña from September to November. The ENSO Indexes for these three particular years are shown in Figure 5.4.

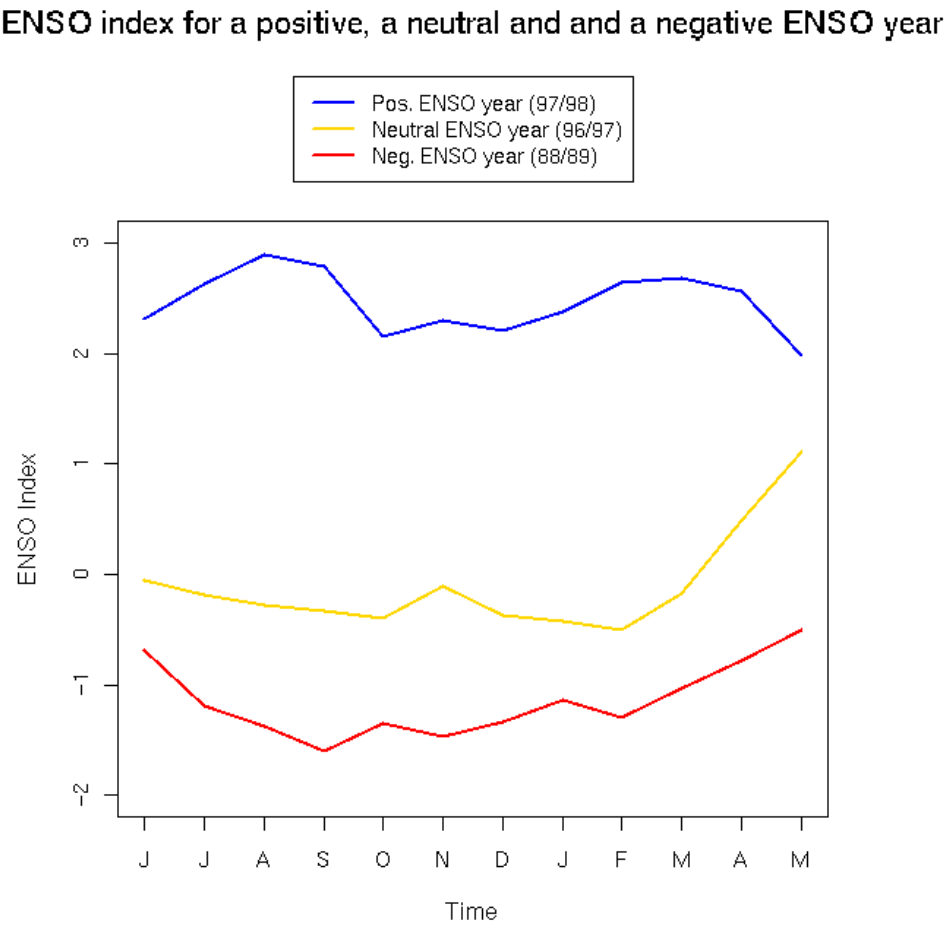

Figure 5.4: ENSO Index for one specific positive, neutral and negative ENSO year

5.2.2 Results

In order to gain a first overview of the patterns that are caused by ENSO, the deseasonalized SIS and the deseasonalized CI are plotted for a typical El Niño and a typical La Niña event (Figure 5.5). The

year 97 and 88 were selected, respectively. For both events, the same months were investigated, namely September, October and November.

El Niño and La Niña showed opposite patterns for SIS as well as for CI. As expected, there were more clouds in north-eastern Brazil during La Niña and more clouds in southern Brazil during the El Niño. The patterns were quite pronounced over Europe despite the fact that ENSO doesn't have a great influence on the European weather in general.

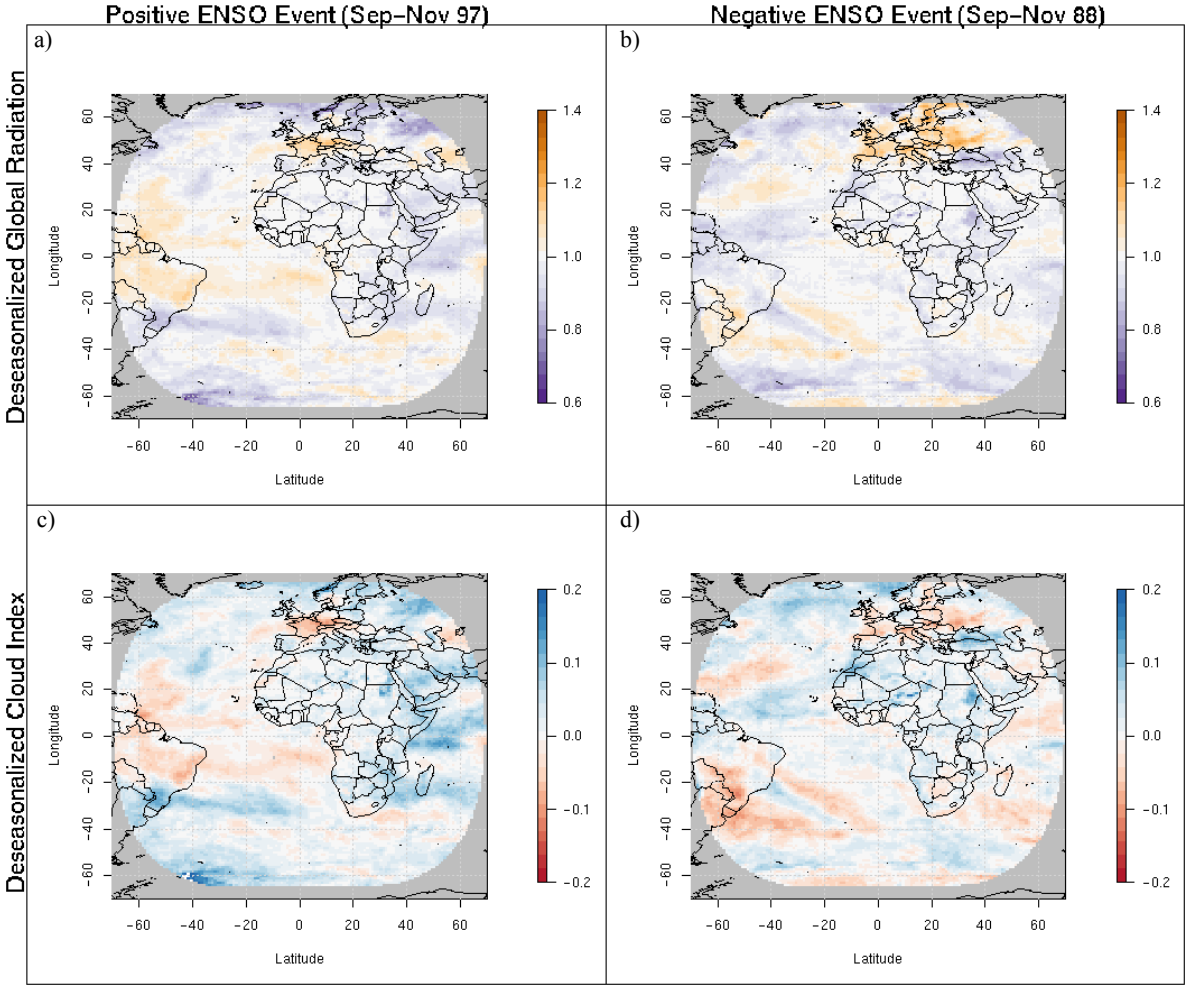

Figure 5.5: Deseasonalized SIS and deseasonalized CI for a typical El Niño and La Niña event

a) Deseasonalized SIS at a positive ENSO event. b) Deseasonalized SIS at a negative ENSO event. c) Deseasonalized CI at a positive ENSO event. d) Deseasonalized CI at a negative ENSO event.

In Figure 5.6, the whole time series of MFG was used and the correlation of the deseasonalized SIS and the deseasonalized CI with the ENSO Index was calculated for each pixel in the visible disc. Only significant correlations were plotted.

There were mainly six patterns identifiable for SIS as well as for CI. It is well observable that positive correlations between SIS and ENSO Index occurred in the northeast of Brazil and in southern Africa whereas negative correlations occurred in the Atlantic between 20°N and 40°N and between 10°S and 30°S, in the southeast of Brazil, in North Africa and the Middle East. The opposite was true for the correlation between CI and ENSO Index.

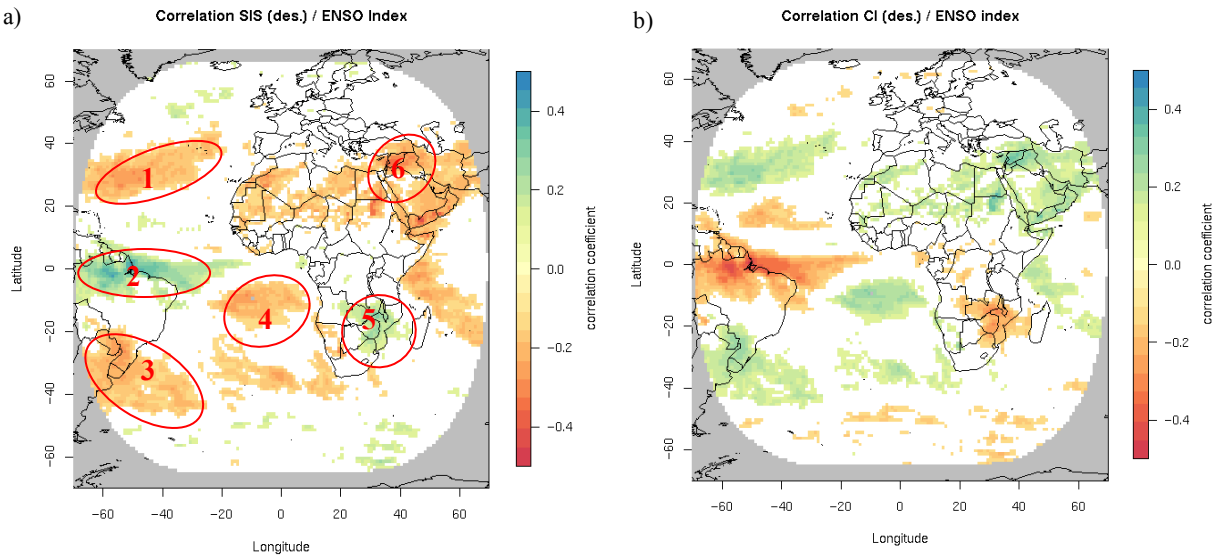

Figure 5.6: Correlation of deseasonalized SIS and deseasonalized CI with ENSO Index

a) Correlation between deseasonalized SIS and ENSO Index with 6 patterns that were investigated in more detail.
b) Correlation between deseasonalized CI and ENSO Index.
Only significant correlations are presented.

Additionally, the correlation between the deseasonalized temperature and precipitation and the ENSO Index was plotted. These patterns corresponded quite well to the observed patterns of the correlation between SIS / CI and ENSO Index. Also, the correlation between cloudiness and precipitation was usually positive. Only pattern 4 was different between CI and the precipitation plot. High cloudiness and simultaneously low precipitation occurred at El Niño events and the opposite was true for La Niña events.

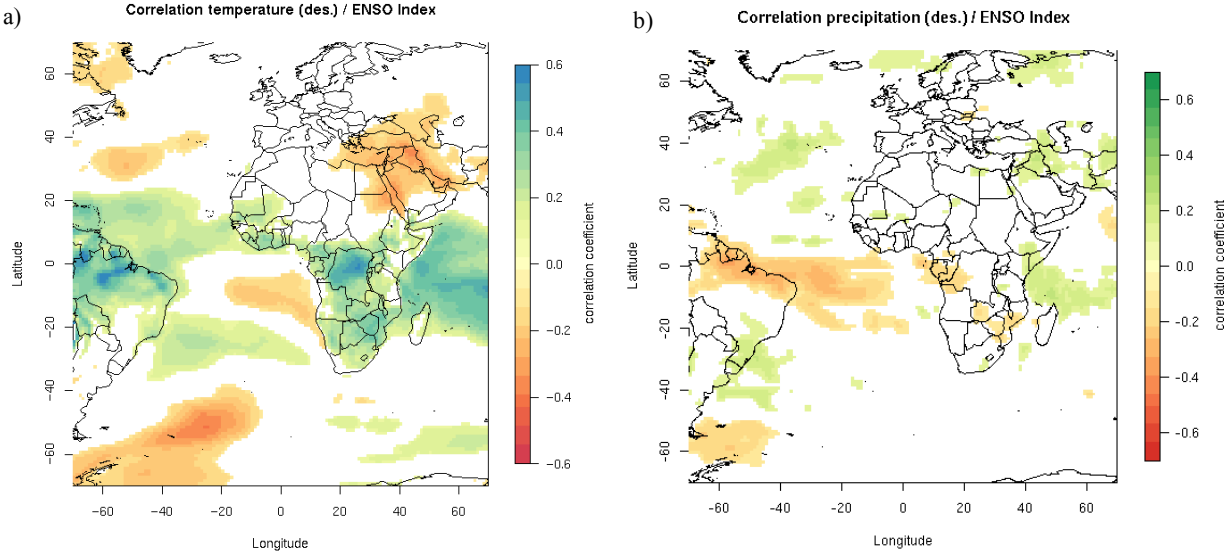

Figure 5.7: Correlation of deseasonalized temperature and deseasonalized precipitation with ENSO Index

a) Correlation between deseasonalized temperature and ENSO Index.
b) Correlation between deseasonalized precipitation and ENSO Index.
Only significant correlations are presented.

Table 5.2 gives an overview of the patterns and the corresponding regions.

Pattern	Region	Coordinates
Pattern 1	Northern Atlantic	27-50°N / 60-10°W
Pattern 2	North east of Brazil	10°S-10°N / 60-30°W
Pattern 3	South east of Brazil	50-20°S / 60-40°W
Pattern 4	Southern Atlantic	20-5°S / 20-15°W
Pattern 5	Southern Africa	35-10°S / 20-40°E
Pattern 6	Middle East	30-40°N / 35-50°E

Table 5.2: Description of the 6 patterns

The regions as well as the coordinates are given. As the significant pixels don't occur in a rectangular pattern, only the pixels that had a significant correlation between CI and ENSO Index were considered.

All six patterns have been investigated in detail. As described in the methods part, for each pattern, an analysis of variance and pairwise T-Tests were conducted in order to test whether the positive, neutral and negative phases were significantly different from each other. In addition, one specific El Niño, one neutral phase and one La Niña were compared.

The ANOVA gave significant differences for all six patterns and for SIS as well as for CI between the positive, neutral and negative phase of ENSO.

Table 5.3 gives an overview of all six patterns.

	Pattern 1	Pattern 2	Pattern 3	Pattern 4	Pattern 5	Pattern 6
Agreement SIS / temperature	yes	yes	no	yes	yes	Yes
Agreement CI / precipitation	yes	yes	yes	no	yes	Yes
Difference in SIS for extreme La Niña year compared to extreme El Niño	0.87 W/m^2	-24.44 W/m^2	17.10 W/m^2	3.05 W/m^2	-4.21 W/m^2	-0.58 W/m^2
Difference in CI for extreme La Niña year compared to extreme El Niño	-0.01 %	0.07 %	-0.08 %	-0.01 %	0.02%	-0.01 %

Table 5.3: Summary of the 6 patterns

The first row indicates whether SIS and temperature showed similar behaviors during the positive, negative and neutral phase of ENSO. The second row states this issue for CI and precipitation. The last two rows present the difference of absolute SIS and absolute CI between the chosen extreme positive (97/98) and extreme negative (88/89) ENSO year.

The results of pattern 4 and 6 are now presented in more detail. These two patterns were chosen because they have not yet been as widely investigated as the other patterns. Pattern 4 showed significant differences between the three ENSO-phases for SIS and CI whereas for precipitation and temperature no trend could be identified. Actually, CI and precipitation showed different behaviors. While there was more cloudiness during positive phases, there seemed at the same time to be less

precipitation. Pattern 6 is also presented more detailed, because it is quite far away from the typical ENSO regions and therefore especially interesting.

A description of the remaining 4 patterns can be found in Appendix 9.5.

5.2.2.1 Pattern 4

Pattern 4 is situated in the southern Atlantic and thus especially interesting because there is no ground station data in this area. During positives phases of ENSO, there was more cloudiness and thus less radiation reaching the surface. During negative phases the opposite was observable (Figure 5.8).

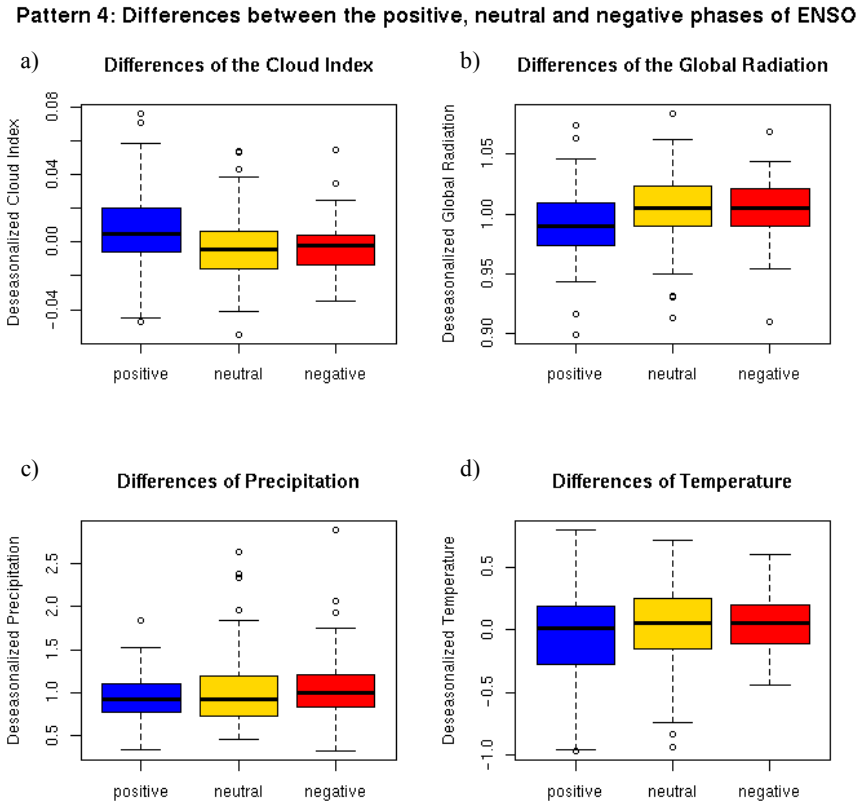

Figure 5.8: Differences between positive, neutral and negative phases of ENSO for pattern 4

a) Differences of deseasonalized CI. b) Differences of deseasonalized SIS.
c) Differences of deseasonalized precipitation. d) Differences of deseasonalized temperature.

There were significant differences for CI and the SIS. The pairwise tests showed that the positive phase was different from the other two phases. However, for precipitation and temperature no pairwise differences were found (see Table 5.4).

Pattern 4		Cloud Index	Global Radiation	Precipitation	Temperature
Means	Mean pos	0.01	0.10	0.94	-0.048
	Mean neut	-0.003	1.00	1.00	0.01
	Mean neg	-0.003	1.00	1.08	0.05
	Global F value	9.3462**	9.2505**	5.7829*	3.0646
Pairwise tests	Pos/neut	**	**	n.s.	n.s.
	Pos/neg	*	*	n.s.	n.s.
	Neut/neg	n.s.	n.s.	n.s.	n.s.

Table 5.4: Descriptives of pattern 4

Npos=85, Nneut=130, Nneg=61, * p<.05, ** p<.01, *** p<.001

In Figure 5.9, the four variables in the specific positive, neutral and negative year are shown. The comparison of these three particular years gave quite opposite results. During the strong phase of La Niña (September to December), there seemed to be more cloudiness and precipitation and less SIS. These results stand in contrast to the ones obtained in Figure 5.8 where the whole time period was investigated.

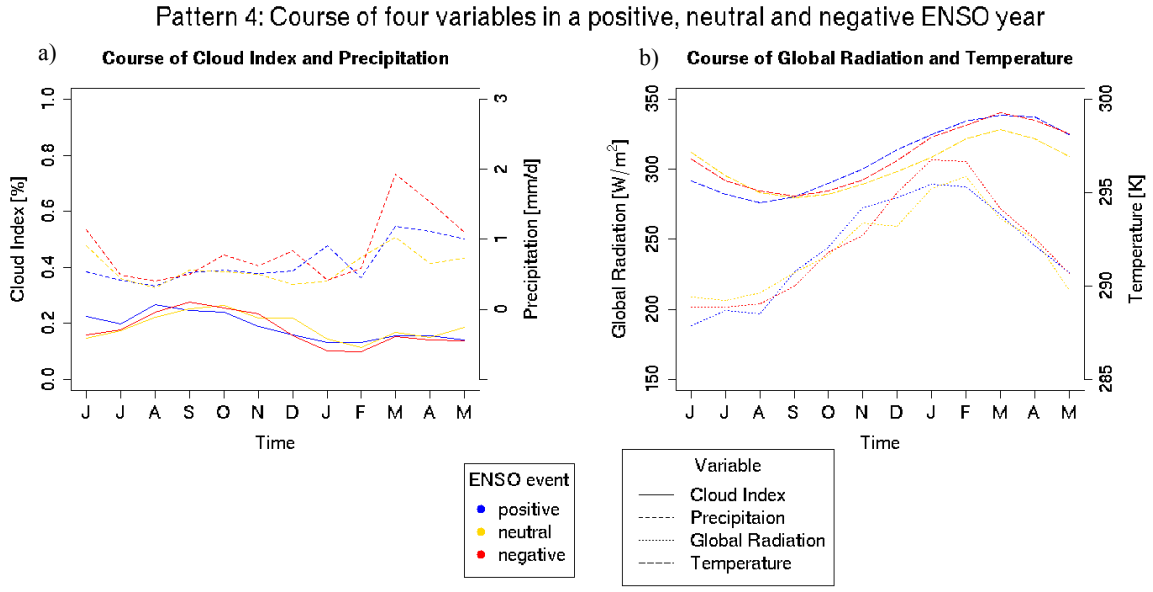

Figure 5.9: Specific positive, neutral and negative ENSO year for pattern 4

a) Course of absolute CI and precipitation in a positive (97/98), neutral (96/97) and negative (88/89) ENSO year.
b) Course of absolute SIS and temperature in a positive (97/98), neutral (96/97) and negative (88/89) ENSO year.

In summary, the trends for pattern 4 were not as clear as for the other patterns. Especially the three specific years with strong El Niño and strong La Niña were in contrast to the result obtained for the whole time period.

5.2.2.2 Pattern 6

Pattern 6 is located in the Middle East and includes only some countries in the eastern part of the Mediterranean. As visible in Figure 5.10, the region was characterized by more cloudiness, more precipitation and both lower SIS and temperature during El Niño phases (opposite conditions during La Niña phases).

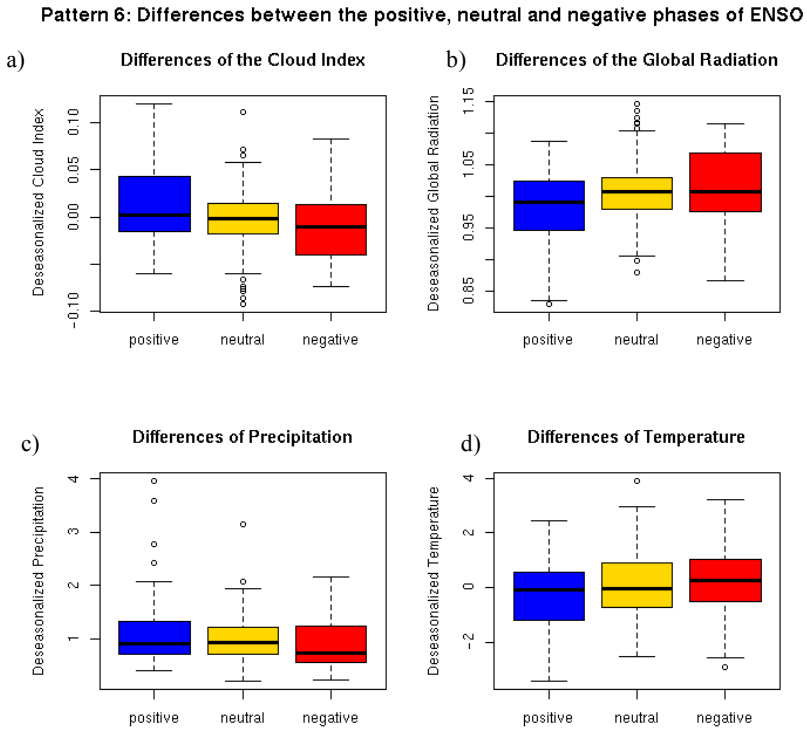

Figure 5.10: Differences between positive, neutral and negative phases of ENSO for pattern 6

a) Differences of deseasonalized CI. b) Differences of deseasonalized SIS.
c) Differences of deseasonalized precipitation. d) Differences of deseasonalized temperature.

Table 5.5 shows that there were significant differences for all four variables. The pairwise tests indicated that especially the positive and negative phases differed significantly and that the differences were more pronounced for CI and SIS as for precipitation and temperature.

Pattern 6		Cloud Index	Global Radiation	Precipitation	Temperature
Means	Mean pos	0.013	0.98	1.11	-0.31
	Mean neut	-0.003	1.01	0.99	0.08
	Mean neg	-0.01	1.01	0.87	0.27
	Global F value	15.597***	14.618***	8.2124**	8.1443**
Pairwise tests	Pos/neut	**	**	n.s.	n.s.
	Pos/neg	***	***	*	*
	Neut/neg	n.s.	n.s.	n.s.	n.s.

Table 5.5: Descriptives of pattern 6

N_{pos}=85, N_{neut}=130, N_{neg}=61, * p<.05, ** p<.01, *** p<.001

Figure 5.11 for the specific ENSO events showed similar results. The cloud index was 6% higher during El Niño and 24 % more precipitation was observed compared to the La Niña year. In contrast, SIS was 0.3% higher during the El Niño year. The mean temperature over this specific time period was the same for the El Niño and the La Niña year. This is not expected, since the higher cloudiness during the El Niño year leads to less radiation at the Earth's surface and therefore lower temperatures.

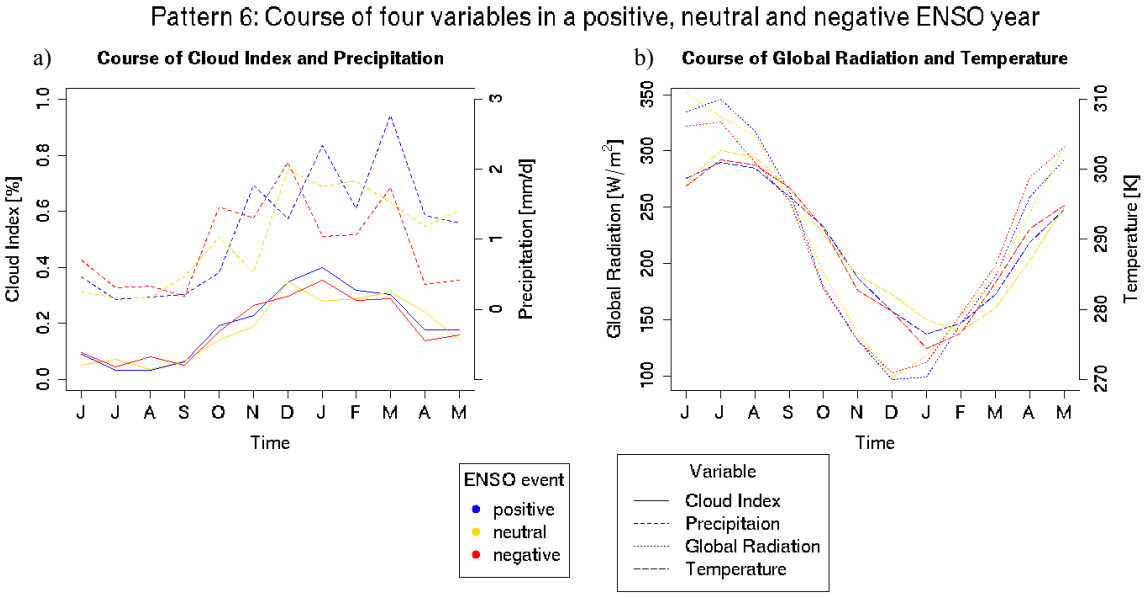

Figure 5.11: Specific positive, neutral and negative ENSO year for pattern 6

a) Course of absolute CI and precipitation in a positive (97/98), neutral (96/97) and negative (88/89) ENSO year.
b) Course of absolute SIS and temperature in a positive (97/98), neutral (96/97) and negative (88/89) ENSO year.

Thus, the cloud index and precipitation anomalies were very clearly pronounced with more precipitation and cloudiness during El Niño and less during La Niña. However, no clear trend was found for both, SIS and temperature.

5.2.3 Discussion

The first ENSO-related research question of the climate analysis part is discussed. In many parts of the visible disc of Meteosat links between ENSO and SIS or CI were found. Especially regions that are strongly affected by ENSO also showed significant correlations between the ENSO anomaly to SIS and CI. SIS was positively correlated to ENSO in the northeast of Brazil and in southern Africa and negatively in the north and south Atlantic, in the southeast of Brazil and in the Middle East. Over Europe, no significant correlations were detected between ENSO and SIS or CI. The above correlations were classified into six patterns. Most of these patterns could be linked to results from previous studies.

Figure 5.12 shows the areas that are affected by El Niño. These regions largely correspond to the patterns documented in the results section. Comparison of Figure 5.5 with Figure 5.12 reveals that patterns 1, 2, 3, and 5 are regions with known ENSO effects.

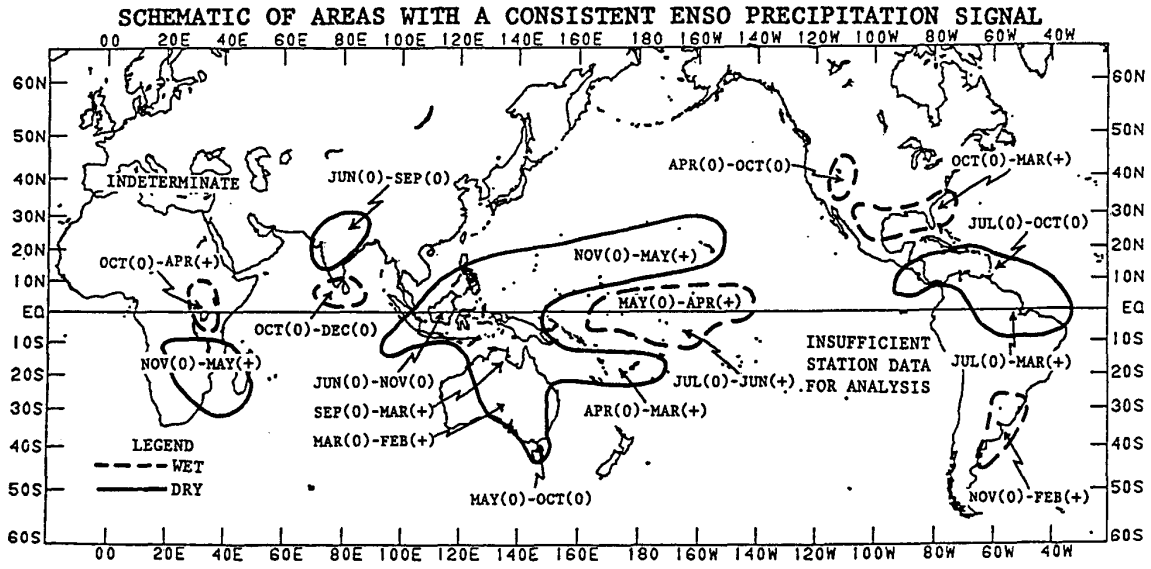

Figure 5.12: Global effects of ENSO (Ropelewski and Halpert, 1986)

Schematic representation of the principal ENSO-related precipitation.

In order to discuss the second research question, each pattern is now compared to the results from previous studies and the physical backgrounds for the appearance of the patterns, where possible, are given.

Pattern 1 showed enhanced cloudiness and precipitation during El Niño events. Figure 5.12 also indicates that this region is wetter than usual during El Niño even though the region's boundaries do not exactly match.

The relationship between ENSO and the climate variability was strongest in pattern 2 (north-eastern Brazil) and was previously investigated by many scientists. The results found for pattern 2 are consistent with many other studies. Walker (1924) already noted that the rainfall variability in north-eastern Brazil is generally related to El Niño. Hastenrath and Heller (1977) also found a relationship between drought in north-eastern Brazil and ENSO. Further, Ropelewski and Halpert (1986) stated that this region had a very consistent ENSO-precipitation relationship. As visible in Figure 5.7, there was less rainfall in north-eastern Brazil during El Niño years. The reason for this effect is mainly that the usually low pressure over the southern Pacific in El Niño years becomes a high pressure system in the southern Atlantic (Hastenrath and Heller, 1977). The high pressure in the southern Atlantic prevents rainfall, because of the subsidence of the air masses and the reduction of the moisture content in the air (Chu, 1991). Thus, the formation of clouds is reduced and more SIS reaches the surface. However, droughts also occurred in the absence of El Niño years and other circulation mechanisms such as movements of low and high pressure areas and changing wind patterns might explain climatic variations in north-eastern Brazil (Chu, 1991).

Pattern 3 suggested more precipitation and clouds during El Niño years. The study of Ropelewski and Halpert (1986) indicated that the relationship between rainfall and ENSO was very consistent and that there was a clear tendency for enhanced precipitation during El Niño phases. The increased precipitation in southern Brazil during El Niño might be related to the strong subtropical westerlies that occur during El Niño events (Arkin, 1982). These enhanced westerlies are in turn activated by the south-southeastward oriented convergence zone.

It is difficult to find results and explanations from previous studies that would correspond to pattern 4, mainly because this pattern is over the ocean. Such areas have only become part of climatic investigation since the advent of globally applicable numerical weather models or satellite data during

the last decades. Papadimas et al. (2010) studied the spatio-temporal variability and co-variability of the downward solar radiation at the Earth's surface. They used factor analysis by grouping time-series that are highly correlated, in a smaller number of new artificial time-series (called factors). Thus, areas with common characteristics of solar radiation variability could be found and teleconnection patterns revealed. The factors resulting from that particular study are summarized in Figure 5.13.

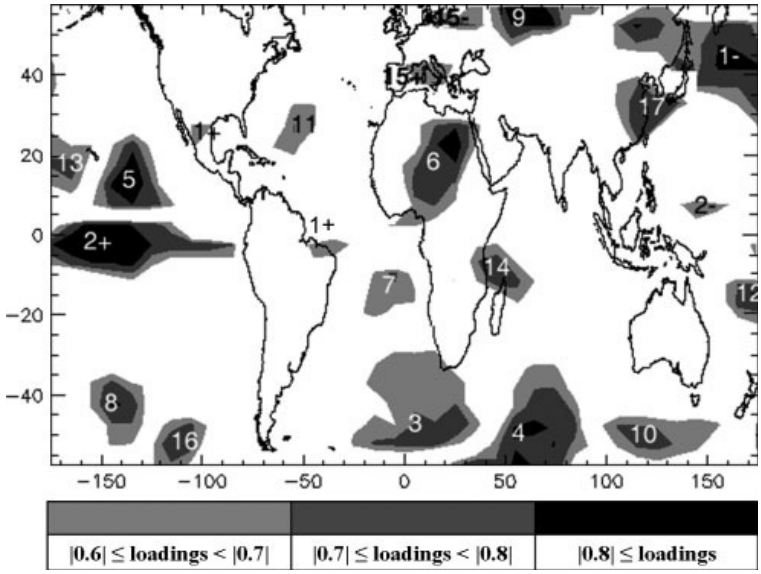

Figure 5.13: Regions with common characteristics of solar radiation variability

Result of factor analysis conducted by Papadimas et al. (2010). Shown are the isopleths of the factor loadings of the most important factors of the solar downward radiation anomalies for the DJF season.

In Figure 5.13, factor 7 corresponds to pattern 4. Papadimas et al. (2010) didn't find a direct link to ENSO, but they pointed out that factor 7 might be explained by common pressure and cloudiness conditions. This deficiency could explain that in Table 5.4 only significant pairwise correlation for the cloud index and SIS have been found but none for precipitation and temperature. In contrast to all other patterns El Niño years tended to have more clouds but less precipitation at the same time for this pattern. Since it is difficult to find climatological explanations for this pattern it is likely that the relationship of SIS and CI with ENSO was by chance.

Ropelewski and Halpert (1986) found that in southern Africa (pattern 5) dry conditions were related to positive ENSO phases. They explained that ENSO was associated with an equatorward shift of the innertropical convergence zone and thus a displacement of clouds and precipitation off from pattern 5. However, according to Nicholson (1983), droughts in eastern Africa are not necessarily related to ENSO and often persist for several years and even decades.

For pattern 6 Ropelewski and Halpert (1986) found a relationship between ENSO and precipitation. However, they also stated that for some particular years the direction of the ENSO-precipitation relationship was changed. As visible from Table 5.5 the pairwise differences for precipitation were only significant between the negative and positive phase. However, CI and SIS differed significantly.

Over Europe no significant correlation (on the 95%-level) was found. However, several authors have studied the impact of ENSO on the climate in Europe and climatic teleconnections with ENSO have been detected (Van Oldenborgh et al., 2000, Kenyon and Hegerl, 2010). Mariotti et al. (2002) found significant correlations between rainfall and the Nino3.4 index (which includes the sea surface temperature anomalies) for the European Mediterranean region. In central and eastern Europe the correlation was found to be negative in autumn and positive in winter and spring. In western Europe

and the Mediterranean region they stated a positive correlation in autumn and a negative correlation in spring. Their results are summarized in Figure 5.14.

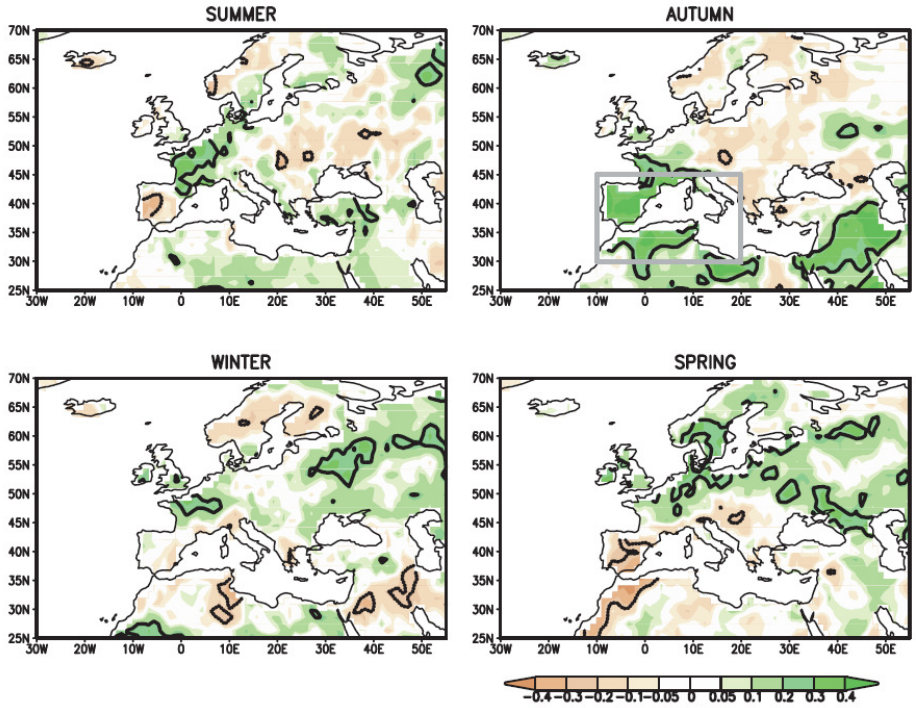

Figure 5.14: Investigations done by Mariotti et al. (2002)

Correlation between rainfall and the Nino3.4 index.

By comparing the correlation in autumn to our correlation in Figure 5.5 (where also the months September to November are presented), it is visible that the results are very similar. Both suggest that there are more rain and clouds over Spain in El Niño years.

In summary, the typical patterns of ENSO yield also clear patterns in the satellite-based climate record about cloudiness and SIS derived from MFG satellites. They are consistent with results from previous studies that look at temperature and precipitation. More patterns could be detected with the satellite data since it covers regions with low coverage of ground-based meteorological measurements. For the regions in South America and South Africa the physical background of these patterns appeared to be sound and compatible with previous explanations (Hurrell, 2011). However, in other regions the relation between ENSO and the underlying climatic processes was less clear.

5.3 North Atlantic Oscillation

5.3.1 Methods

For the NAO, only a positive and a negative phase were distinguished. The allocation was done according to Hurrell (2011). A monthly based NAO Index was used. In Figure 5.15, the course of the NAO Index for all months during the investigated time period is shown.

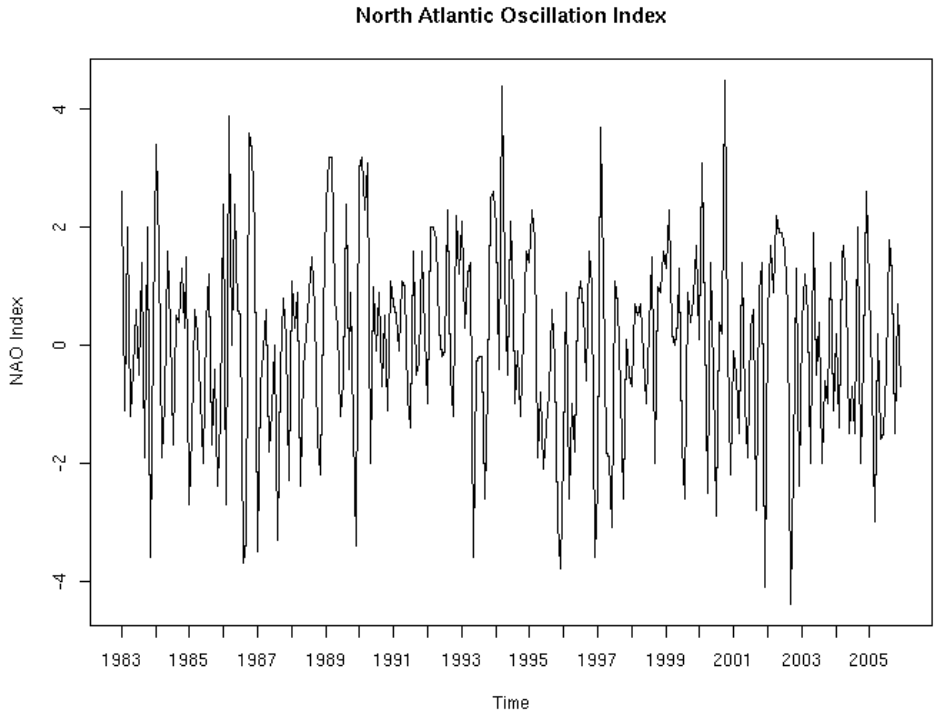

Figure 5.15: North Atlantic Oscillation Index

Course of NAO Index between 1983 and 2005.

In the following analyses only the months of the winter half year were considered (October to March). The monthly index of the NAO is based on the difference of the normalized sea level pressures between Ponta Delgada (Azores) and Stykkisholmu/Reykjavik (Iceland) (Hurrell, 2011).

Again, the correlation between the NAO Index and deseasonalized SIS, CI, precipitation and temperature was calculated and the significant correlations were plotted.

Further, investigations in different specific European countries have been conducted. Therefore, Spain, France, Italy, Ireland and southern Scandinavia were used and the absolute CI, SIS, precipitation and temperature were calculated in winter. The described values are the average over all pixels in each particular country and over all positive or negative winters, respectively. Positive and negative winters are listed in Table 5.6.

Positive winters		Negative winters
1983	1994	1985
1984	1995	1987
1986	1998	1996
1988	1999	1997
1989	2000	2001
1990	2002	2004
1991	2003	
1992	2005	
1993		

Table 5.6: Positive and negative NAO winters

5.3.2 Results

In contrast to ENSO, the NAO has much more influence on the European climate, because the oscillation consists of a dipole of pressure anomalies in the north Atlantic that is associated with changes in the surface westerlies onto Europe. As mentioned above, the NAO is most distinct in winter months. In Figure 5.16, the mean deseasonalized SIS and CI are presented in a positive and negative NAO winter. It is well detectable that SIS was increased over the Iberian Peninsula, France and Italy and decreased over Great Britain, Scandinavia and eastern Europe during the positive winter. During the negative winter, the opposite was observable, but with important exceptions. For instance, only over Germany, Poland and in the southwest of Scandinavia increased SIS was seen.

Additionally to the influence of the NAO onto Europe, also opposite patterns during the positive and negative phase over South America were identified. Especially in the south of Brazil, decreased SIS seemed to go along with the positive phase and increased SIS with the negative phase. However, this relationship was quite low, especially during the negative phase.

As expected, CI showed opposite correlations to NAO compared to the SIS.

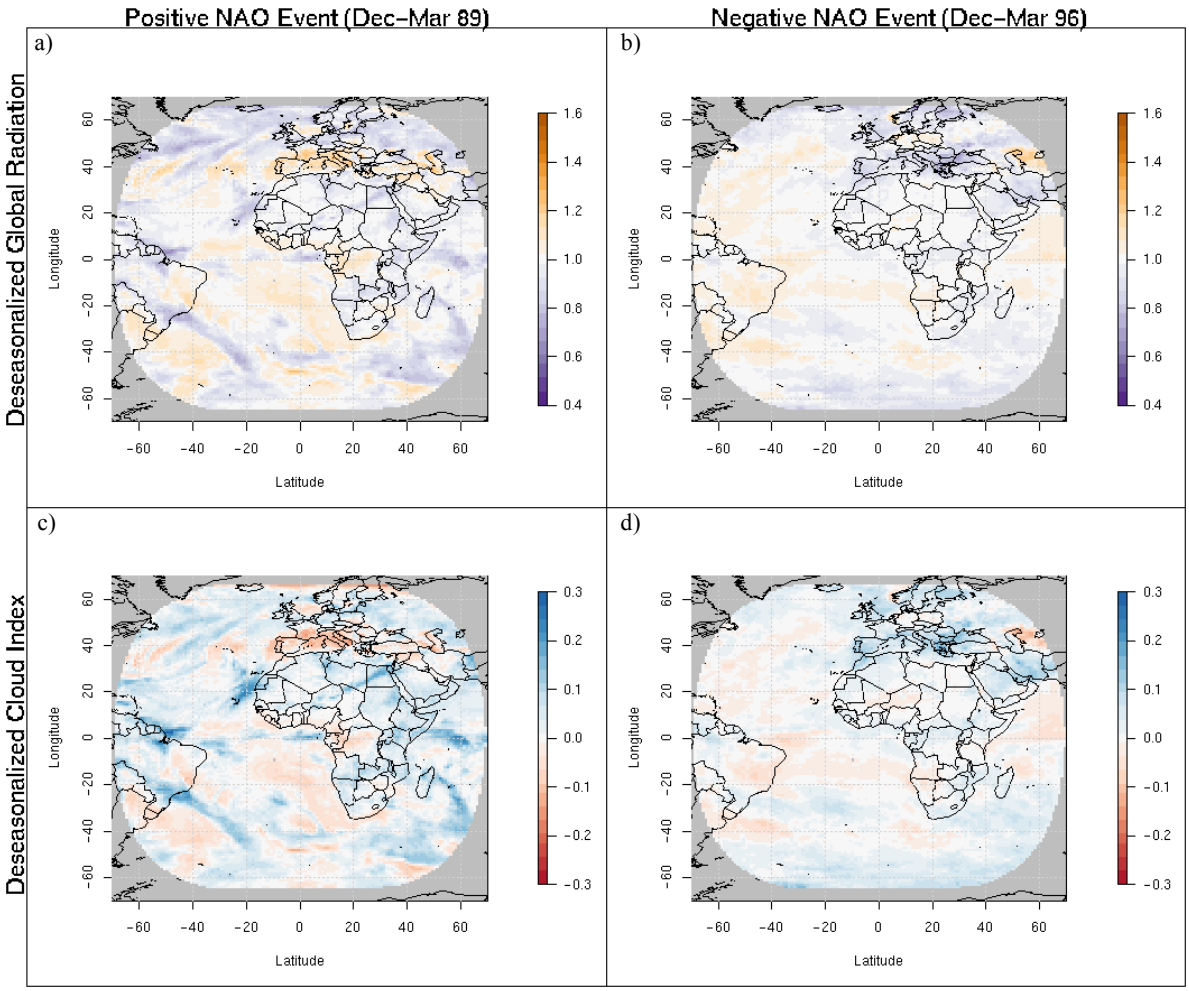

Figure 5.16: Deseasonalized SIS and deseasonalized CI for a typical positive and negative NAO Event

a) Deseasonalized SIS at a positive NAO event. b) Deseasonalized SIS at a negative NAO event.
c) Deseasonalized CI at a positive NAO event. d) Deseasonalized CI at a negative NAO event.

In Figure 5.17, the correlation is plotted for each pixel in the time period of 1983 to 2005 for the months from October to March between the NAO Index and SIS or CI, respectively. Clear patterns were visible in southern Europe: increased SIS during positive and decreased SIS during negative

phases. The correlations over Ireland and Scandinavia were opposed to the correlations over northern Europe. An interesting pattern could be seen between Ireland, England and Scandinavia. While over the continents the correlation of SIS and the NAO was negative, a positive correlation was detected at the eastern coast of England.

Further, quite distinct patterns were found over the northern Atlantic. While the Azores were characterized by an increased SIS and less clouds during the positive phase of the NAO, the opposite correlation was detected more northwards over the Atlantic. Over the other parts of the visible disc of Meteosat, especially over Africa and South America, no correlations were found.

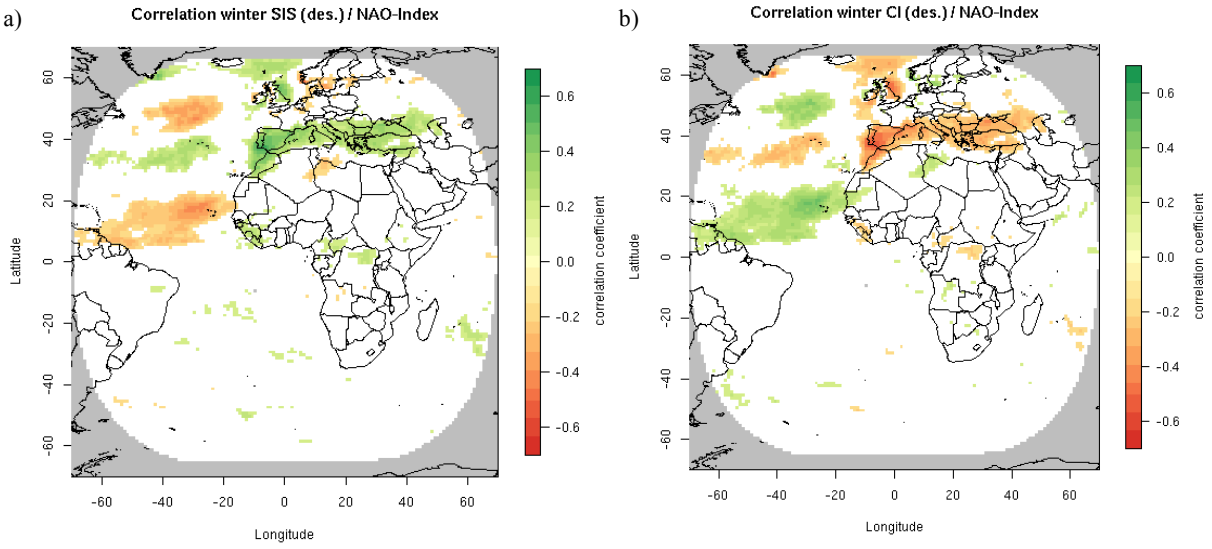

Figure 5.17: Correlation of deseasonalized SIS and deseasonalized CI with NAO Index in winter months

a) Correlation between deseasonalized SIS and NAO Index.
b) Correlation between deseasonalized CI and NAO Index.
Only significant correlations are presented.

Figure 5.18 a) shows that in general Europe was warmer during positive phases of the NAO. Only in Spain there was no significant correlation. Iceland and Greenland were on the other hand characterized by a negative correlation between temperature and NAO Index. As single variable, the temperature seemed to be significantly influenced by the NAO over North Africa.

It is also noteworthy that the correlation of the temperature with the NAO exceeded the other three discussed correlations.

The precipitation plot in Figure 5.18 b) is characterized by a positive correlation over northern Europe and a negative correlation over south-western Europe. The patterns of precipitation and of the CI didn't agree everywhere. Especially over the ocean in the north of Europe, the correlations seemed to be inversely. This is in contrast to what would be expected, namely a positive relation between CI and precipitation.

During the positive NAO phase wet and warm weather occurs in northern Europe and dry and cold weather in southern Europe.

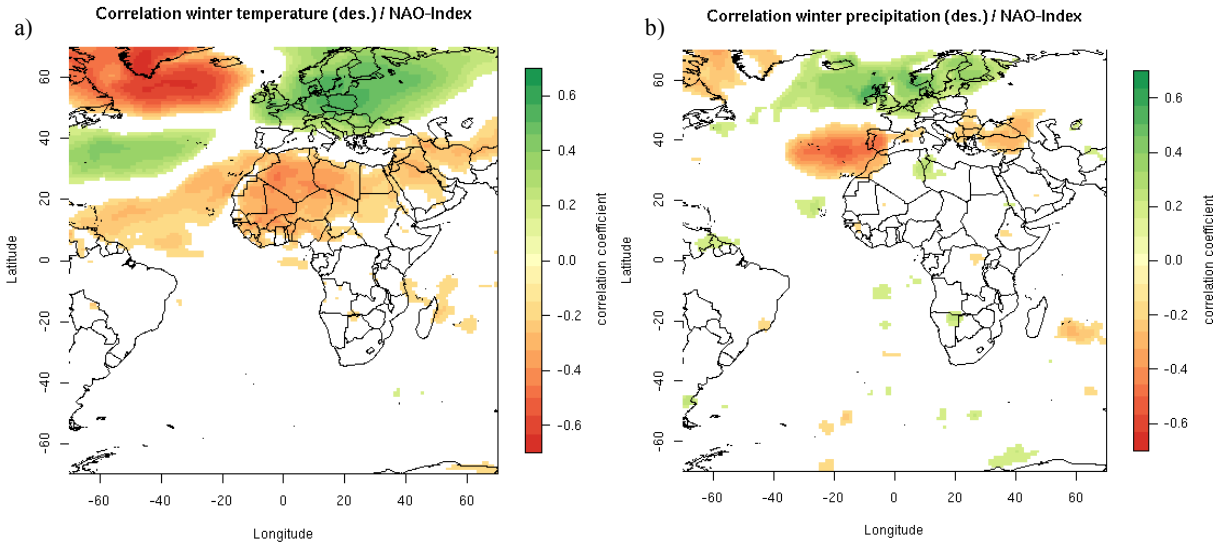

Figure 5.18: Correlation of deseasonalized temperature and precipitation with NAO Index in winter months

a) Correlation between deseasonalized temperature and NAO Index.
b) Correlation between deseasonalized precipitation and NAO Index.
Only significant correlations are presented.

In Table 5.7, the effects of positive and negative NAO winters for five selected countries are described. All winters between 1983 and 2005 were used and each winter was assigned either to a positive or negative event. Three countries in southern Europe were taken and for northern Europe, Ireland and southern Scandinavia were investigated, because they showed the most distinct patterns.

	NAO phase	Cloud index	Global radiation	Precipitation	Temperature
Spain	Positive winters	0.25	124.88 W/m^2	1.91 mm/h	280.33 K
	Negative winters	0.28	120.50 W/m^2	2.29 mm/h	279.97 K
France	Positive winters	0.39	81.18 W/m^2	2.60 mm/h	278.34 K
	Negative winters	0.41	78.53 W/m^2	2.71 mm/h	277.99 K
Italy	Positive winters	0.33	98.08 W/m^2	2.34 mm/h	276.74 K
	Negative winters	0.36	93.35 W/m^2	2.94 mm/h	276.36 K
Ireland	Positive winters	0.46	51.59 W/m^2	4.67 mm/h	279.56 K
	Negative winters	0.45	51.58 W/m^2	4.24 mm/h	279.43 K
Southern Scandinavia	Positive winters	0.50	38.19 W/m^2	3.15 mm/h	270.34 K
	Negative winters	0.50	38.54 W/m^2	2.89 mm/h	270.18 K

Table 5.7: Absolute values of the four variables for positive and negative winters

Comparison of absolute cloud index, global radiation, precipitation and temperature between positive and negative winters.

In all three countries located in southern Europe, CI was smaller and SIS was higher during winters with a positive NAO. In contrast, both variables over Ireland and southern Scandinavia were insensitive to the phase of NAO. For the precipitation there is a pronounced discrepancy between southern and northern Europe. Generally, there was more precipitation over the 3 southern countries

during negative winters and more precipitation over Ireland and southern Scandinavia during positive NAO winters.

5.3.3 Discussion

It is firstly discussed whether it is possible to detect relationships between SIS or CI and the NAO by use of the CM SAF climate data record. Because the NAO is located in the north Atlantic, the visible disc of Meteosat is generally suited for the investigation. One exception is North America that is also influenced by the NAO but cannot be investigated here. It is not surprising that distinct patterns and relationships were found specifically over Europe. These patterns were further most pronounced during winter months, but also relationships and significant correlations were found by investigating other seasons. It was also visible that the correlations were most pronounced in the northern hemisphere, whereas in the southern hemisphere less significant relationships between the NAO Index and weather patterns were found.

The remaining section of this discussion treats the second research question for the NAO.

The physical patterns of the NAO have been widely investigated, among others by Hurrell (1995) or by Wanner (2001). It is known that the NAO exerts a dominant influence on surface air temperatures, storminess, precipitation, ocean heat content, ocean currents and sea ice cover (Hurrell et al., 2003). While temperature variations can be associated to changes in the pressure systems, precipitation variations are related to the shift and intensification in the Atlantic storm activity. However, the increased storm activity is again a consequence of the strengthened pressure anomalies. During positive phases of the NAO, the pressure in the subtropical Atlantic is higher than normal and over the northern Atlantic lower than normal. Hence, the westerlies are strengthened and bring relatively warm air over Europe, especially in winters. At the same time, the northerly winds over Greenland and north-eastern Canada are enhanced and carry cold air southwards which decreases the temperatures over the northwest Atlantic. Because the subtropical high-pressure center is strengthened, the clockwise wind that flows around this center is also stronger and brings colder air to North Africa and the Middle East (Hurrell et al., 2003, Hurrell and VanLoon, 1997). Thus, during positive NAO phases, the temperature is increased over Europe and decreased over the north Atlantic and over northern Africa.

The precipitation patterns reported in literature can be explained by the Atlantic storm activities. During positive phases, the storms are shifted northeastwards and there is an enhanced activity from Newfoundland into northern Europe and a simultaneously weakened activity over southern Europe (Rogers, 1997). At the same time, there are also more intense and frequent storms in the vicinity of Iceland and the Norwegian Sea (Serreze et al., 1997).

These relationships of temperature and of precipitation with the NAO are well visible in Figure 5.18. It is also detectable, that the enhanced westerlies bring relatively warm air masses over almost whole Europe whereas the storm tracks dominate in northern Europe and over Iceland.

It remains to discuss the patterns for SIS and CI. CI is strongly but not linearly related to the precipitation. In general, regions with enhanced storm activities in positive phases were characterized by more rain and thus a higher cloudiness (and lower SIS) and inversely. This was true for southern Europe where less rain and less cloud cover was observable during positive phases and for the north Atlantic and parts of Great Britain and Scandinavia with more rain and a higher CI. However, this relationship was not clear over the ocean between the British islands and Scandinavia and between Great Britain and Iceland. In these regions, there is a negative correlation between precipitation and CI in winter months (Figure 4.17). As this negative correlation only occurred over the ocean, there are no

other studies at hand that would help explaining the result. In order to investigate the reasons for this behaviour in more detail, precipitation and CI were plotted in a strong positive and negative NAO year (Figure 5.19).

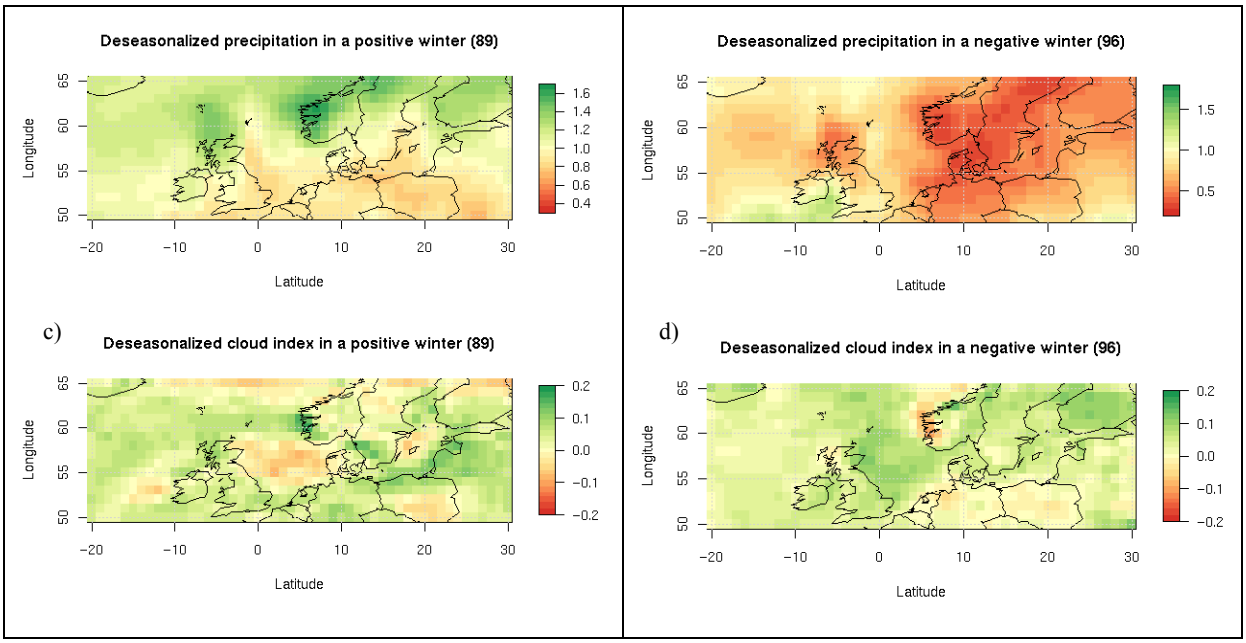

Figure 5.19: Deseasonalized precipitation and cloud index in a positive (89) and negative (96) NAO year

a) Deseasonalized precipitation in a positive NAO year. b) Deseasonalized precipitation in a negative NAO year. c) Deseasonalized CI in a positive NAO year. d) Deseasonalized CI in a negative NAO year.

It is observable that during the positive phase of NAO during winter precipitation as well as CI were higher than normal over large areas of northern Europe with single exceptions. The pattern in the negative phase of NAO during winter was much more interesting. There was, as expected, less precipitation than normal; but in contrast, CI was still relatively high. Only in the southwest of Scandinavia, the cloud index was smaller than normal. In the south of Great Britain and in the west of Ireland neither a positive nor a negative trend was visible. Exactly in these regions, a positive correlation between CI and NAO Index was observed (compare to Figure 5.17). Thus, during the positive phase of NAO in winter CI and precipitation were both higher than normal, but during the negative phase of NAO in winter, only precipitation was decreased without a simultaneously decrease of the cloudiness. The conclusion of this pattern is that there was a high cloudiness in the negative phase of NAO in winter, but the clouds didn't bring more precipitation. There are no other studies to compare this result with, because no one has investigated the behaviour of SIS over this specific region. Chiacchio and Wild (2010) studied the effect of the NAO on downward surface shortwave radiation (DSW) at GEBA stations but not over the ocean. Further investigation is necessary to approve this pattern and to find physical explanations.

It is also visible in Figure 5.19 that CI between Great Britain and Scandinavia was exactly inverse to what was expected, in the positive as well as in the negative winter. It was decreased during the positive phase of NAO in winter and increased during the negative phase.

In the following, the results of similar studies are discussed and compared to our results. The most similar study is the one conducted by Chiacchio and Wild (2010). As already mentioned, they investigated the relation between the downward surface shortwave radiation, measured by GEBA stations, and the NAO Index. They found statistically significant and high correlations (up to 0.68) in southern Europe for the period between 1970 and 2000. A more detailed overview of their correlation analysis is given in Figure 5.20.

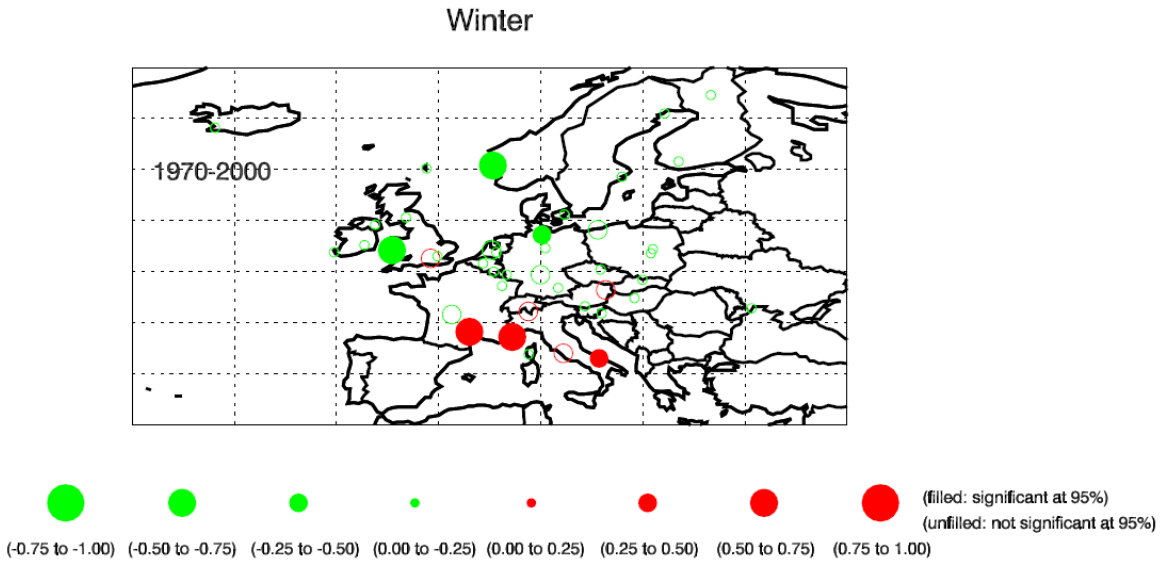

Figure 5.20: Correlation between surface solar radiation and NAO Index

Map of correlation coefficients displayed for each site in winter (DJF) between the surface solar radiation and the North Atlantic Oscillation (NAO) Index during 1970–2000. Magnitudes and their signs of correlation (red circles for positive and green circles for negative values) are computed. Significant correlation coefficients at the 95% confidence level are filled circles, and non-significant correlation coefficients are unfilled circles (Chiacchio and Wild, 2010).

These correlations correspond very well to the ones found in Figure 5.17. The highest correlations between temperature and NAO Index were also around 0.6.

In Figure 5.18, increased temperatures over Europe and decreased temperatures over the northwest Atlantic were found. This is consistent with the results of Hurrell (1995). He also stated that since 1980 warm winters in Europe and cold conditions in the northwest Atlantic were observable. At the same time, the NAO was mainly in the positive phase during winters (Hurrell, 1995). Hurrell (1995) suggested that these temperature conditions are strongly related to the NAO Index.

These explanations show that the patterns found in this study correspond quite well to the results from similar studies and can well be explained.

6 Conclusion

This chapter summarizes the most important findings of this master thesis and gives an outlook motivating further scientific investigations in the field.

The thesis consisted of two parts, namely the homogeneity analysis and a climate analysis.

6.1 Homogeneity analysis

By use of the SNHT several temporal inhomogeneities were found throughout the CM SAF climate data record of SIS. Especially over Africa inhomogeneities were detected. Problematic regions also occurred in the high latitudes. Over Europe, the Sahara and over the oceans, only few pixels were subject to breaks.

A new spatial homogeneity test was then developed that includes the information of spatially adjacent pixels and tests the homogeneity of a region instead of single pixels. The results were similar to the ones of the SNHT. However, the influence of a break in a single pixel was reduced and only breaks that were significant over a large region were detected. The adjustment of the significance level by use of the Bonferroni-correction allowed to extract the important breaks. The spatial test developed within this study should be generally applicable for homogeneity analysis of gridded data sets.

It was decided to not homogenize the climate data record because the breaks couldn't be allocated to satellite replacements and the breaks did not affect climatic trends in the data set.

There are two issues that need further investigation: on the one hand the enhancement of the spatial test and on the other hand a careful investigation about typical characteristics of satellite data and about the quality requirements of reference data.

Three key issues and research questions arose from the present study that need further investigation. Firstly, how should a spatio-temporal data set be homogenized once a discontinuous pattern of breaks has been found by the newly developed spatial test? Secondly, what are the next steps needed to enhance the spatial test? Thirdly, how can uncertainties and potential discontinuities in the reference data be treated more appropriately?

Follow-up research is needed in order find out how to deal with the breaks detected by the spatial test developed within this thesis. The distinct regional patterns revealed by the homogeneity analysis is of great value when revising the CM SAF climate data record of SIS. It has to be kept in mind that the breaks found here are likely not due to satellite changes, so they must have been introduced by the heliosat algorithm that was used to derive the data record from the raw and uncalibrated satellite data. In comparison to a classical ground station time series (which cannot be re-measured) the CM SAF climate data record can be re-generated with an improved algorithm based on the detective work carried out as part of this thesis. Still, for breaks that cannot be traced back to algorithm deficiencies a method needs to be developed for how to correct the discontinuous spatial field of such breaks. It should for instance be evaluated if only patches with significant breaks shall be corrected and neighboring patches are then kept untouched. A strategy may further be chosen to correct inhomogeneities grouped by climatologically similar regions like land/oceans or by bioclimatic gradients (like tropical, temperate, boreal, maritime, continental). The latter strategy is supported by the results of this thesis which demonstrate a dependency of breaks from the underlying surface types and/or geographic region.

Extensions of the existing spatial test could possibly improve its effectiveness. In the following, several extensions are proposed.

In this thesis, model 2 (see 4.2.3) was used, because it estimated the height of the break most appropriately and it detected breaks with low magnitudes. However, other criteria not investigated here might also be important. So far, we know that each model has been successful when employed with simulated data using the same model. All other cases have not yet been tested. Therefore, the robustness of a model with data coming from a different model could serve as a criterion. Table 6.1 shows which combinations have been tested in this thesis and the ones that were not investigated (with question mark). For instance, the model that works well with simulation data from most of the other models could be chosen as the most reliable one.

		Simulation			
		Model 1	Model 2	Model 3	SNHT
Use	Model 1	Good	?	?	?
	Model 2	?	Good	?	?
	Model 3	?	?	Good	?
	SNHT	?	?	?	Good

Table 6.1: Robustness under different models

The cases in the diagonal have been investigated in this thesis; it remains to examine the other combinations in a next step.

Another option would be to vary the number of spatial and temporal neighbors. In this thesis, the combination of 4 spatial and 2 temporal neighbors was used. However, it is very likely that other combinations are more appropriate. The number of neighbors of course depends on the characteristics of the respective data set.

In the existing spatial test the height of the break was parameterized by a (by a scalar) for every pixel. However, a priori knowledge might indicate that some pixels in the region are free of breaks. For instance, our analysis has demonstrated that the break pattern might be restricted to land or ocean areas depending on the chosen region. Therefore, a vector with 0 and 1 could be inserted in order to ensure that for pixels without a break a is set to zero.

As a last example of possible extensions, models that contain more than one break could be developed. As the CM SAF climate data record is based on a retrieval method that is carried out pixel wise and therefore largely independent in time and space, a model with for instance two breaks and three different μ's per pixel would probably be more appropriate. It is expected that the parameters of the precision matrix would change because they wouldn't have to adjust anymore for a single mean value in the time series.

Reference data sets should be investigated in more detail before carrying out the homogeneity test. For instance, the ERA-Interim could be used as reference in combination with ground stations where available. This was not possible within the current study as the time series of the GEBA-stations that cover the full time period of the satellite dataset have not yet been homogenized (personal communication from Arturo Sanchez, 04.07.2011). However, upon availability, GEBA data could serve as reference in order to guarantee the stability of the ERA-Interim model-based data. In addition, it could be investigated whether the spatial patterns of breaks in both the satellite and the model-based data have different characteristics in dependence of surface type, climatic region or satellite viewing geometry.

Finally, it would be important to apply the spatial test to other data sets in order to evaluate its general applicability to spatio-temporal data. In general, all data sets that are gridded and potentially contain breaks can be investigated as long as corresponding reference series are available. For instance, the ERA-40 and ERA-Interim could be tested against each other in order to adjust ERA-40 towards ERA-Interim.

6.2 Climate analysis

A climate analysis was conducted with the CM SAF climate data record. Significant correlations and patterns between three large scale climate variability phenomena and SIS or cloud index have been detected. The relation of SIS to ENSO and NAO over the whole visible disc of Meteosat is especially interesting as it has not been investigated before.

Significant positive correlations between the ENSO Index and SIS were found in the northeast of Brazil and in southern Africa. Negative correlations were found in the Atlantic between 20°N and 40°N and between 10°S and 30°S, in the southeast of Brazil, in North Africa and in the Middle East. Six spatial patterns were identified where the difference between the negative and positive ENSO phase was significant. Over Europe no significant correlations were found. The correlations and patterns found for ENSO were in line with results from earlier studies. However, there were few important exceptions. For instance, over the southern Atlantic there was a positive correlation between the ENSO Index and cloud index, but a negative correlation between ENSO Index and precipitation.

The correlation between NAO and SIS was positive over northern Europe and negative over parts of Ireland, Great Britain and Scandinavia. While the temperature had a positive correlation with the NAO over most parts of Europe, SIS was significantly positive at much less locations. Also cloud index and precipitation showed partly different correlations with the NAO. Especially, over the ocean between England and Scandinavia and between England and Iceland cloud index and precipitation showed opposed behaviors. A more detailed inspection revealed that especially in the negative NAO winter low precipitation and at the same time a high cloud index were found whereas the positive NAO winter showed both, higher precipitation and higher cloud index. Thus, during the negative NAO winter precipitation was decreased without a simultaneously decrease of the cloudiness.

The findings from the analysis of large scale variability phenomena were causally explained with underlying climatological processes and they further agree with similar studies based on precipitation or temperature.

The analysis has demonstrated that the CM SAF climate data record is potentially suitable for a wide range of climate analysis exercises. In this thesis only few topics were examined. As the CM SAF data record covers a large area and has a relatively high temporal and spatial resolution homogeneously covering land and ocean areas with the same spatial density, it can serve for much more investigations. For instance, global dimming and brightening trends could be investigated (Wild et al, 2005). As the time period of global brightening began in the eighties, the data record might be appropriate to monitor the present brightening trends. Trend difference between rural and urban areas, or maritime and continental areas, could for instance be examined. Furthermore, it would also be interesting to study the effect of volcanic eruptions (Pinatubo and El Chichon) on CM SAF data record of SIS.

In addition, it is also important to advance the understanding of the interactions between the greenhouse gas forcing, changes in temperature and SIS and the NAO (Hurrell et al., 2003). The satellite data record could help to investigate these interactions because it contains long term measurements of SIS and the cloud index over exactly the region that is most influenced by the NAO with a high spatial resolution.

These examples outline how the CM SAF climate data record of SIS is of great value for climate monitoring and climate analysis. Any methodological improvements of the CM SAF climate data record based on the results found by the homogeneity analysis in the first part of this thesis will transfer into a more reliable future version of this data set that in turn will increase its significance in climate research.

7 References

ADLER, R., HUFFMAN, G., CHANG, A., FERRARO, R., XIE, P., JANOWIAK, J., RUDOLF, B., SCHNEIDER, U., CURTIS, S., BOLVIN, D., GRUBER, A., SUSSKIND, J., ARKIN, P. & NELKIN, E. 2003. The version-2 global precipitation climatology project (GPCP) monthly precipitation analysis (1979-present). *Journal of Hydrometeorology,* 4, 1147-1167.

ALEXANDER, L., UOTILA, P. & NICHOLLS, N. 2009. Influence of sea surface temperature variability on global temperature and precipitation extremes. *Journal of Geophysical Research-Atmospheres,* 114, 13pp.

ALEXANDERSSON, H. 1984. A homogeneity test based on ratios and applied to precipitation series. Uppsala, Sweden: Department of Meteorology.

ALEXANDERSSON, H. 1986. A homogeneity test applied to precipitation data. *Journal of Climatology,* 6, 661-675.

ARCTIC PORTAL. 2011. High Temperature in the North – Cold in the south [Online]. Arctic Portal. Available: http://arcticportal.org/features/features-of-2010/high-temperature-in-the-north-cold-in-the-south [Accessed 29.08.2011].

ARKIN, P. A. 1982. The relationship between interannual variability in the 200 mb tropical wind field and the Southern Oscillation. *Monthly weather review,* 110, 1393-1404.

BEYER, H., COSTANZO, C. & HEINEMANN, D. 1996. Modifications of the Heliosat procedure for irradiance estimates from satellite images. *Solar Energy*, 3, 207-212.

BROENNIMANN, S., 2007. Impact of El Niño-Southern Oscillation on European climate. *Reviews of Geophysics*, *45,* 3.

CANO, D., MONGET, J. M., ALBUISSON, M., GUILLARD, H., REGAS, N. & WALD, L. 1986. A method for the determination of the global solar radiation from meteorological satellite data. *Solar Energy,* 37, 31-39.

CHIACCHIO, M. & WILD, M. 2010. Influence of NAO and clouds on long-term seasonal variations of surface solar radiation in Europe. *Journal of Geophysical Research-Atmospheres,* 115, 17pp.

CHU, P.-S. 1991. Brazil's Climate Anomalies and ENSO. *In:* GLANTZ, M. H., KATZ, R. W. & NICHOLLS, N. (eds.) *Teleconnetcions linking wordlwide climate anomlies.* Cambridge: Cambridge University Press.

CLIMATE PREDICTION CENTER INTERNET TEAM. 2011. Pacific North/American (PNA) [Online]. NOAA/National Weather Service. Available: http://www.cpc.ncep.noaa.gov/data/teledoc/pna.shtml [Accessed 03.08.2011].

COMMONWEALTH OF AUSTRALIA.2011. Climate variablity and El Niño [Online]. Australia: Bureau of Meteorology. Available: http://www.bom.gov.au/climate/glossary/elnino/elnino.shtml [Accessed 29.08.2011].

CUBASCH, U. & MEEHL, G. A. 2001. Projections of future climate change. *In:* HOUGHTON, J. T., DING, Y., GRIGGS, D. J., NOGUER, M., VAN DER LINDEN, P. J. & XIAOSU, D. (eds.) *Climate Change 2001, The Scientific Basis.* Cambridge: Cambridge Univ. Press.

CZAJA, A., ROBERTSON, A. W. & HUCK, T. 2003. The role of Atlantic ocean-atmosphere coupling in affecting North Atlantic Oscillation variability. *In:* HURRELL, J. W., KUSHNIR, Y., OTTERSEN, G. & VISBECK, M. (eds.) *The North Atlantic Oscillation: Climatic Significance and Environmental Impact.* Washington: American Geophysical Union.

DEE, D., UPPALA, S., SIMMONS, A., BERRISFORD, P., POLI, P., KOBAYASHI, S., ANDRAE, U., BALMASEDA, M., BALSAMO, G., BAUER, P., BECHTOLD, P., BELJAARS, A., VAN DE BERG, L., BIDLOT, J., BORMANN, N., DELSOL, C., DRAGANI, R., FUENTES, M., GEER, A., HAIMBERGER, L., HEALY, S., HERSBACH, H., HOLM, E., ISAKSEN, L., KALLBERG, P., KOHLER, M., MATRICARDI, M., MCNALLY, A., MONGE-SANZ, B., MORCRETTE, J., PARK, B., PEUBEY, C., DE ROSNAY, P., TAVOLATO, C., THEPAUT, J. & VITART, F. 2011. The ERA-Interim reanalysis: configuration and performance of the data assimilation system. *Quarterly Journal of the Royal Meteorological Society,* 137, 553-597.

DIJKSTRA, H. A. 2006. The ENSO phenomenon: theroy and mechanisms. *Advances in Geosciences,* 6, 3-15.

DUCRE-ROBITAILLE, J., VINCENT, L. & BOULET, G. 2003. Comparison of techniques for detection of discontinuities in temperature series. *International Journal of Climatology,* 23, 1087-1101.

EUMETSAT. 2010. Monitoring weather and climate from space [Online]. Darmstadt: European Organisation for the Exploitation of Meteorological Satellites. Available: http://www.eumetsat.int/Home/Main/Satellites/MeteosatFirstGeneration/index.htm?l=en [Accessed 23.02 2011].

FENG, S., HU, Q. & OGLESBY, R. 2011. Influence of Atlantic sea surface temperatures on persistent drought in North America. *Climate Dynamics,* 37, 569-586.

GLICKMAN, T. S. 2000. Solar radiaton. *In:* SOCIETY, A. M. (ed.) *Glossary of Meteorology.* 2 ed. Cambridge, Massachusetts: American Meteorological Society.

GRAF, H., KIRCHNER, I. & PERLWITZ, J. 1998. Changing lower stratospheric circulation: The role of ozone and greenhouse gases. *Journal of Geophysical Research-Atmospheres,* 103, 11251-11261.

HARTMANN, D. L. 1994. Global Physical Climatology, San Diego, Academic Press.

HASTENRATH, S. & HELLER, L. 1977. Dynamics of climate hazards in Northeast Brazil. *Quaterly journal of the royal meteorological society,* 103, 77-92.

HEINO, R. 1994. Climate in Finland during the period of meteorological observations. Academic dissertation.

HELD, L. 2008. Methoden der statistischen Inferenz - Likelihood and Bayes, Heidelberg, Spektrum Akademischer Verlag.

HUNSLEY, A. 1997. Newton Raphson method pictures [Online]. Available: http://www.tardis.ed.ac.uk/~lard/fc/newton/index.html [Accessed 16.06.2011].

HURRELL, J. W. 1995. Decadal Trends in the North Atlantic Oscillation: Regional Temperatures and Precipitation. *Science,* 269, 676-679.

HURRELL, J. 1996. Influence of variations in extratropical wintertime teleconnections on Northern Hemisphere temperature. *Geophysical Research Letters,* 23, 665-668.

HURRELL, J. & VANLOON, H. 1997. Decadal variations in climate associated with the north Atlantic oscillation. *Climatic Change,* 36, 301-326.

HURREL, J., KUSHNIR, Y., VISBECK, M. 2001. The North Atlantic Oscillation. *Science*, 26, 603-605.

HURRELL, J., KUSHNIR, Y., OTTERSEN, G. & VISBECK, M. 2003. An overview of the North Atlantic oscillation. *In:* HURRELL, J. W., KUSHNIR, Y., OTTERSEN, G. & VISBECK, M. (eds.) *The North Atlantic Oscillation: Climatic Significance and Environmental Impact.* Washington: American Geophysical Union.

HURRELL, J. 2011. Climate Analysis Section [Online]. Boulder: National Center for Atmospheric Research. Available: http://www.cgd.ucar.edu/cas/jhurrell/indices.data.html#naostatmon [Accessed 06.08.2011].

KENYON, J. & HEGERL, G. C. 2010. Influence of modes of climate variabilty on global precipitation extremes. *Journal of Climate,* 23, 6248-6262.

KILADIS, G. N. & MO, K. C. 1998. Interannual and intraseasonal variability in the Southern Hemisphere. *In:* KAROLY, D. J. & VINCENT, D. G. (eds.) *Meteorology of the Southern Hemisphere.* Boston: American Meteorological Society.

KNORR-HELD, L. 2000. Bayesian modelling of inseparable space-time variation in disease risk. *Statist. Med. 2000, 19, 2555-2567.*

LOHMANN, S., SCHILLINGS, C., MAYER, B. & MEYER, R. 2006. Long-term variability of solar direct and global radiation derived from ISCCP data and comparison with reanalysis data. *Solar Energy,* 80, 1390-1401.

MARIOTTI, A., ZENG, N. & LAU, K. 2002. Euro-Mediterranean rainfall and ENSO - a seasonally varying relationship. *Geophysical Research Letters,* 29, 59-1-59-4.

MOBERG, A. & ALEXANDERSSON, H. 1997. Homogenization of Swedish temperature data .2. Homogenized gridded air temperature compared with a subset of global gridded air temperature since 1861. *International Journal of Climatology,* 17, 35-54.

Moesch, M., ZELENKA, A. 2004. Arbeitsbericht: Globalstrahlungsmessung 1981-2000 im ANETZ, Zurich, MeteoSchweiz.

NICHOLSON, S. E. 1983. Sub-Saharan rainfall in the year 1976-1980: Evidence of a continued drought. *Monthly weather review,* 111, 1646-1654.

NULL, J. 2011. El Niño and La Niña Years and Intensities [Online]. Available: http://ggweather.com/enso/oni.htm [Accessed 02.08.2011].

PAPADIMAS, C. D., FOTIADI, A. K., HATZIANASTASSIOU, N., VARDAVAS, I. & BARTZOKAS, A. 2010. Regional co-variability and teleconnection patterns in surface solar radiation on a planetary scale. *International Journal of Climatology,* 30, 2314-2329.

PETERSON, T. & EASTERLING, D. 1994. Creation of homogeneous composite climatological series. *International Journal of Climatology,* 14, 671-679.

PINKER, R., ZHANG, B. & DUTTON, E. 2005. Do satellites detect trends in surface solar radiation? *Science,* 308, 850-854.

PORTIS, D. H., WALSH, J. E., HAMLY, M. E. & LAMB, P. J. 2000. Seasonality of the North Atlantic Oscillation. *J. Climate,* 13, 2069-2078.

POSSELT, R., TRENTMANN, J., STÖCKLI, R. & MÜLLER, R. 2011a. Presentation and Validation of CM SAF's surface radiation climate data record. *Remote Sens.,* 3, 1029-1046.

POSSELT, R., MÜLLER, R., STÖCKLI, R. & TRENTMANN, J. 2011b. Spatial and Temporal Homoegeneity of Solar Surface Irradiance across Satellite Generations. *Remote Sensing, 3,* 1029-1046.

RANDEL, W. & WU, F. 1999. Cooling of the arctic and antarctic polar stratospheres due to ozone depletion. *Journal of Climate,* 12, 1467-1479.

RASMUSSON, E. M. & CARPENTER, T. H. 1983.

Meteorological aspects of the El Niño/Southern Oscillation. *Science,* 222, 1195-1202.

ROBERTSON, A., MECHOSO, C. & KIM, Y. 2000. The influence of Atlantic sea surface temperature anomalies on the north Atlantic oscillation. *Journal of Climate,* 13, 122-138.

ROGERS, J. 1997. North Atlantic storm track variability and its association to the north Atlantic oscillation and climate variability of northern Europe. *Journal of Climate,* 10, 1635-1647.

ROPELEWSKI, C. F. & HALPERT, M. S. 1986. Global and Regional Scale Precipitation Patterns Associated wiht the El Niño/Southern Oscillation. *Monthly weather review,* 115, 1606-1626.

RUE, H. & HELD, L. 2005. Gaussian Markov Random Fields: Theory and Applications*,* Boca Raton, Chapman & Hall/CRC.

SACHS, L & HEDDERICH, J. 2006. Angewandte Statistik: Methodensammlung mit R, Heidelberg, Springer-Verlag.

SCHIBLI, R. 2011. Semester thesis: Global radiation from Meteosat First Generation satellites, Zurich, MeteoSwiss.

SCHMETZ, J., PILI, P., TJEMKES, S., JUST, D., KERKANN, J., ROTA, S. & RATIER, A. 2002. An introduction to Meteosat Second Generation (MSG). *Bulletin of the American Meteorological Society*, 977-992.

SERREZE, M., CARSE, F., BARRY, R. & ROGERS, J. 1997. Icelandic low cyclone activity: Climatological features, linkages with the NAG, and relationships with recent changes in the Northern Hemisphere circulation. *Journal of Climate,* 10, 453-464.

SHINDELL, D., MILLER, R., SCHMIDT, G. & PANDOLFO, L. 1999. Simulation of recent northern winter climate trends by greenhouse-gas forcing. *Nature,* 399, 452-455.

STATE CLIMATE OFFICE OF NORTH CAROLINA. 2011. Global Pattern - Pacific/North American (PNA) [Online]. State Climate Office of North Carolina. Available: http://www.nc-climate.ncsu.edu/climate/patterns/PNA.html [Accessed 15.08.2011 2011].

SUTTON, R. T., NORTON, W. A. & JEWSON, S. P. 2001. The North Atlantic Oscillation - What role for the Ocean? *Atm. Sci. Lett.,* 1, 89-100.

TONIAZZO, T. & SCAIFE A. A. 2006. The influence of ENSO on winter North Atlantic climate, *Geophys. Res. Lett.,* 33, 5pp.

TORETI, A., KUGLITSCH, F., XOPLAKI, E., DELLA-MARTA, P., AGUILAR, E., PROHOM, M. & LUTERBACHER, J. 2011. A note on the use of the standard normal homogeneity test to detect inhomogeneities in climatic time series. *International Journal of Climatology,* 31, 630-632.

TRENBERTH, K.E. 1991. General Characteristics of El Niño-Southern Oscillation. *In:* GLANTZ, M. H., KATZ, R. W. & NICHOLLS, N. (eds.) *Teleconnetcions linking wordlwide climate anomlies.* Cambridge: Cambridge University Press.

ULBRICH, U. & CHRISTOPH, M. 1999. A shift of the NAO and increasing storm track activity over Europe due to anthropogenic greenhouse gas forcing. *Climate Dynamics,* 15, 551-559.

UPPALA, S., KALLBERG, P., SIMMONS, A., ANDRAE, U., BECHTOLD, V., FIORINO, M., GIBSON, J., HASELER, J., HERNANDEZ, A., KELLY, G., LI, X., ONOGI, K., SAARINEN, S., SOKKA, N., ALLAN, R., ANDERSSON, E., ARPE, K., BALMASEDA, M., BELJAARS, A., VAN DE BERG, L., BIDLOT, J., BORMANN, N., CAIRES, S., CHEVALLIER, F., DETHOF, A., DRAGOSAVAC, M., FISHER, M., FUENTES, M., HAGEMANN, S., HOLM, E., HOSKINS, B., ISAKSEN, L., JANSSEN, P., JENNE, R., MCNALLY, A., MAHFOUF, J., MORCRETTE, J., RAYNER, N., SAUNDERS, R., SIMON, P., STERL, A., TRENBERTH, K., UNTCH, A., VASILJEVIC, D., VITERBO, P. & WOOLLEN, J. 2005. The ERA-40 re-analysis. *Quarterly Journal of the Royal Meteorological Society,* 131, 2961-3012.

VAN LOON, H. & SHEA, D.J. 1985. The Southern Oscillation. Part IV: The Precursors South of 15°S to the Extremes of the Oscillation. *Monthly Weather Review*, 113, 2063-2074.

VAN OLDENBORGH, G., BURGERS, G. & TANK, A. 2000. On the El Nino teleconnection to spring precipitation in Europe. *International Journal of Climatology,* 20, 565-574.

WALKER, G. T. 1924. Correlation in seasonal variations of weather, IX: A furtherstudy of world weather. *Memoirs of the Inidan meeorological departement,* 24, 275-332.

WANNER, H., BRONNIMANN, S., CASTY, C., GYALISTRAS, D., LUTERBACHER, J., SCHMUTZ, C., STEPHENSON, D. & XOPLAKI, E. 2001. North Atlantic Oscillation - Concepts and studies. *Surveys in Geophysics,* 22, 321-382.

WILD, M., GILGEN, H., ROESCH, A., OHMURA, A., LONG, C., DUTTON, E., FORGAN, B., KALLIS, A., RUSSAK, V. & TSVETKOV, A. 2005. From dimming to brightening: Decadal changes in solar radiation at Earth's surface. *Science*, 5723, 847-850.

WMO 2011. Guide to Climatological Practices. *In:* ORGANIZATION, W. M. (ed.). Geneva: World Meteorological Organization.

XIE, S. & TANIMOTO, Y. 1998. A pan-Atlantic decadal climate oscillation. *Geophys. Res. Lett.,* 25, 2185-2188.

8 Plagiarism declaration

I declare that this thesis is all my own work and all references contained within it have been correctly cited and the original authors acknowledged.

Zurich, 16.09.2011 _____

9 Appendix

9.1 95% critical significance level for SNHT

n	T95	n	T95	n	T95	n	T95
201	9.553	226	9.628	251	9.702	276	9.752
202	9.556	227	9.631	252	9.704	277	9.754
203	9.559	228	9.634	253	9.706	278	9.756
204	9.562	229	9.637	254	9.708	279	9.758
205	9.565	230	9.64	255	9.71	280	9.76
206	9.568	231	9.643	256	9.712	281	9.762
207	9.571	232	9.646	257	9.714	282	9.764
208	9.574	233	9.649	258	9.716	283	9.766
209	9.577	234	9.652	259	9.718	284	9.768
210	9.58	235	9.655	260	9.72	285	9.77
211	9.583	236	9.658	261	9.722	286	9.772
212	9.586	237	9.661	262	9.724	287	9.774
213	9.589	238	9.664	263	9.726	288	9.776
214	9.592	239	9.667	264	9.728	289	9.778
215	9.595	240	9.67	265	9.73	290	9.78
216	9.598	241	9.673	266	9.732	291	9.782
217	9.601	242	9.676	267	9.734	292	9.784
218	9.604	243	9.679	268	9.736	293	9.786
219	9.607	244	9.682	269	9.738	294	9.788
220	9.61	245	9.685	270	9.74	295	9.79
221	9.613	246	9.688	271	9.742	296	9.792
222	9.616	247	9.691	272	9.744	297	9.794
223	9.619	248	9.694	273	9.746	298	9.796
224	9.622	249	9.697	274	9.748	299	9.798
225	9.625	250	9.7	275	9.75	300	9.8

Table 9.1: Critical 95% significance level for SNHT

The calculation was done by MeteoSwiss according to Alexandersson (1986).

9.2 R-Code for the SNHT

```
f.alexshift2 <- function(dqseries,conf.level=0.95,alex.crit.val=alex95krit,
min.seg.length=12)
{
  ## DESCRIPTION: standard normal homogeneity test for shift developed by
  ##              Alexandersson
  ##
  ##              H0: Z(i) Element N(0,1)
  ##
  ##              HA: Z(i) Element N(mu1,sigma)
  ##                  Z(i) Element N(mu2,sigma)
  ##
  ## The standard deviation of the two parts of Q series (before and after
  ## the break are considered to be the
  ## same but are not equal to 1. This is due to the change of mean.
  ## Difference or quotient series (dqseries) is standardized (testz)
  ## and test quantity (testz5)is calculated. The calculation of the test
  ## value is made according to Anders Moberg (Temperature Variations
  ## in Sweden
  ## Since the 18th Century, Paper B, APPENDIX 4, S. IV,1996.)
  ## MOBERG, A., 1996: Temperature variations in Sweden since
  ## the 18th century.
  ## Doctoral Dissertation 1996 no 5, Department of Physical Geography,
```

```
  ## Stockholm University.
  ## ------------------------------------------------------------------------
  ## ARGUMENTS
  ## Required: dqseries:      difference series
  ##           conf.level:    confidenze level for test (0.9 or 0.95)
  ##           alex.crit.val: vector of critical values for different n
  ##           min.seg.length: if date of break within min.seg.length,
  ##                           a flag (probably edge problem) is set
  ##
  ## ------------------------------------------------------------------------
  ## VALUE: vector containing minstelle, test value, inhomog and critval
  ##    maxalex:     number of the last value of the first segment
  ##    maxtestalex: test value of Alexandersson test
  ##    inhomog:     logical (T,F), depending on significance of test value
  ##    alex.crit.val: critical Alex-test value
  ##    edge.probl:  logical (T,F), depending on min.seg.length
  ## ------------------------------------------------------------------------
  ## other functions needed:
  ## ------------------------------------------------------------------------
  ## DETAILS:
  ## ------------------------------------------------------------------------
  ## Author: W. Bosshard und M. Baudenbacher(SMA/E/KLS), adapted for NORM90
  ##         by Marianne Giroud and Michael Begert (NORM90)
  ## Modified for ENSEMBLES 4.11.2005, M. Begert

  nm <- length(dqseries)

  ## There are no critical values for less than 10 values
  if (nm < 10) {
    stop("critical values for less than 10 input values not defined")
  }

  ## normalization of q-qdqseries
  testz <- (dqseries - mean(dqseries))/((var(dqseries))^0.5)

  ## calculation  of testvalue
  testz3 <- cumsum(testz[1:length(testz)])
  testz4 <- sum(testz) - testz3
  testz5 <- (-2)*length(testz)*
  log(sqrt((length(testz)-1-(testz3[1:length(testz)]^2/c(1:length(testz))
      + testz4[1:length(testz)]^2/c(length(testz):1)))/length(testz)))-1

  maxtestalex <- max(testz5,na.rm=T)
  # position of change point
  maxalex <- (1:length(testz5))[testz5 == maxtestalex]
  edge.probl <- F

 if(maxtestalex > alex.crit.val[nm]){
    inhomog <- T
    if((maxalex >= min.seg.length) & ((nm-maxalex) >= min.seg.length)){
      edge.probl <- F
    } else{
      edge.probl <- T
    }
  } else {
    inhomog <- F
  }

return(list(maxalex=maxalex,maxtestalex=maxtestalex,krit.val=inhomog,alex.c
rit.val[nm],edge.probl=edge.probl))
}
```

9.3 R-Code for Spatial Test

9.3.1 Model 1

Precision matrix

```
fun.matQ.mod1 <- function(b,c,f,rown,coln,n,m){
#n number of pixels: n <- rown*coln
#m number of points in time
#b,f parameters of spatial and temporal precision matrix
#k parameter of precision matrix

matB <- matrix(0,nrow=coln*rown,ncol=rown*coln) # Matrix B

# vectorized version
rxc <- rown*coln

# 1D kernel of 4 spatial corner points centered at position 0
krow <- rep(c(-1,0,0,1),times=rxc)
kcol <- rep(c(0,-1,1,0),times=rxc)

# 1D index of rows and columns
irow <- rep(rep(seq(1:rown),times=coln),each=4)
icol <- rep(rep(seq(1:coln),each=rown),each=4)

rtmp <- irow + krow
ctmp <- icol + kcol

idx <- which ((ctmp >= 1) & (ctmp <= coln) & (rtmp >= 1) & (rtmp <= rown))

r2 <- irow[idx] + (icol[idx] - 1) * rown
c2 <- rtmp[idx]  + (ctmp[idx] - 1) * rown

matB[r2 + (c2-1) * rxc] <- b

matC <- matrix(0,m,m) # Matrix C for Kronecker product
# vectorized version
idx <- seq(1:(m-1))
matC[idx + idx*m] <- 1
matC[idx + 1 + (idx-1)*m] <- 1

temp <- kronecker(diag.spam(m),-as.spam(matB)) -
kronecker(as.spam(matC),(diag.spam(n)*f)) # I %x% -B + C %x% -f*I ### add
as.spam
diag(temp) <- 1

return( (temp)*c )
}

library(spam)
source("MA/spatialtest/prec.matrix/matQ.mod1.r")
```

Spatial Test under H0

```
test.H0 <-
function(y,mu1,b,c,f,rown,coln,n=coln*rown,m=nrow(y),Rstruct=NULL,...) {
    f.b <- function(b) {
      0.49-(0.5/0.29)*b
    }
    if (!is(Rstruct, "spam.chol.NgPeyton")) {
      Q <- fun.matQ.mod1(b,c,f,rown,coln,n,m)
        if (!is.spam(Q))
```

```
          stop("'Covariance' should return a spam object.")
          Rstruct <- chol.spam(Q,...)
    }

    neg2loglikelihood <- function(fulltheta,...) {
      if(fulltheta[n+3] < f.b(fulltheta[n+1])) {

      resid <- c(t(y)-fulltheta[1:n])
      Q <- fun.matQ.mod1(fulltheta[n+1],fulltheta[n+2],fulltheta[n+3],
rown,coln,n,m)
      cholS <- update.spam.chol.NgPeyton(Rstruct,Q,...)

      return(n * m * log(2 * pi) - 2 *
c(determinant.spam.chol.NgPeyton(cholS)$modulus)+sum(resid*(Q%*%(resid))))
      }
      else {
      return(1e10)
      }
    }

    return(optim(c(mu1,b,c,f), neg2loglikelihood, method = "L-BFGS-B",
                lower=c(rep(-5,n),1e-5,1e-5,1e-
5),upper=c(rep(25,n),0.29,1000,0.49,control=list(reltol=1e-4))))
}
```

Spatial Test under H1

```
test.H1<-function(y,mu1,a,tb,b,c,f,
rown,coln,n=coln*rown,m=nrow(y),Rstruct=NULL,...) {
    f.b <- function(b) {
    0.49-(0.5/0.29)*b
    }

    if (!is(Rstruct, "spam.chol.NgPeyton")) {
      Q <- fun.matQ.mod1(b,c,f,rown,coln,n,m)
      if (!is.spam(Q))
      stop("'Covariance' should return a spam object.")
    Rstruct <- chol.spam(Q,...)
    }

    neg2loglikelihood <- function(fulltheta,...) {
      if(fulltheta[n+3] < f.b(fulltheta[n+1])) {
      resid1 <- t(y[1:tb,])-fulltheta[1:n]
      mu2 <- fulltheta[1:n]+fulltheta[(n+4)]
      resid2 <- t(y[(tb+1):m,])-mu2
      resid <- c(cbind(resid1,resid2))
      Q <- fun.matQ.mod1(fulltheta[n+1],fulltheta[n+2], fulltheta[n+3],
rown,coln,n,m)
      cholS <- update.spam.chol.NgPeyton(Rstruct,Q,...)

      return(n * m * log(2 * pi) - 2 *
c(determinant.spam.chol.NgPeyton(cholS)$modulus)+sum(resid*(Q%*%(resid))))

      }
      else {
      return(1e10)
      }
    }

    return(optim(c(mu1,b,c,f,a), neg2loglikelihood, method = "L-BFGS-B",
                lower=c(rep(-1,n),1e-5,1,1e-5,-
2),upper=c(rep(25,n),0.29,1000,0.49,2,control=list(reltol=1e-4))))
}
```

Data Simulation

```
sim.data <- function(mu0,b,c,f,rown,coln,m,...) {
    # m: number of points in time
    mu <- rep(mu0,m)
    Q <- fun.matQ.mod1(b,c,f,rown,coln,n=rown*coln,m)
    return( t(array(rmvnorm.prec(1,mu=mu,Q=Q,...),c(rown*coln,m))))
}
```

9.3.2 Model 2

Precision matrix

```
fun.matQ.mod2 <- function(b,c,f,rown,coln,n,m){
#n number of pixels: n <- rown*coln
#m number of points in time
#b,f parameters of spatial and temporal precision matrix
#c parameter of precision matrix
matB <- matrix(0,nrow=n,ncol=n) # Matrix B
for(i in (rown+1):n) {
matB[(i-rown),i] <- b
matB[i,(i-rown)] <- b
}
for(i in 2:n) {
matB[(i-1),i] <- b
matB[i,(i-1)] <- b
}
for(i in 1:(coln-1)) {
matB[(i*rown+1),(i*rown)] <- 0
matB[(i*rown),(i*rown+1)] <- 0
}

matC <- matrix(0,m,m) # Matrix C for Kronecker product
for(i in 1:(m-1)) {
matC[i,i+1] <- 1
matC[i+1,i] <- 1
}
temp <- kronecker(diag.spam(m),-as.spam(matB)) -
kronecker(as.spam(matC),(diag.spam(n)*f)) # I %x% -B + C %x% -f*I ### add
as.spam
diag(temp) <- diff(temp@rowpointers)

return( (temp)*c )
}
```

Spatial Test under H0

```
test.H0 <-
function(y,mu1,b,c,f,rown,coln,n=coln*rown,m=nrow(y),Rstruct=NULL,...) {
    f.b <- function(b) {
    -2.110491*(b^4)+4.975194*(b^3)-4.548725*(b^2)+0.642487*b + 1.94
    }

    if (!is(Rstruct, "spam.chol.NgPeyton")) {
      Q <- fun.matQ.mod2(b,c,f,rown,coln,n,m)
      if (!is.spam(Q))
      stop("'Covariance' should return a spam object.")
      Rstruct <- chol.spam(Q,...)
    }
```

```
    neg2loglikelihood <- function(fulltheta,...) {
      if(fulltheta[n+3] < f.b(fulltheta[n+1])) {
      resid <- c(t(y)-fulltheta[1:n])
       Q <- fun.matQ.mod2(fulltheta[n+1],fulltheta[n+2],fulltheta[n+3],
rown,coln,n,m)
      cholS <- update.spam.chol.NgPeyton(Rstruct,Q,...)

      return(n * m * log(2 * pi) - 2 *
c(determinant.spam.chol.NgPeyton(cholS)$modulus)+sum(resid*(Q%*%(resid))))

      }
      else {
        resid <- c(t(y)-fulltheta[1:n])
        bb <-  seq(0,1.29,by=0.01)
        ff <- f.b(bb)
        dd <- rep(NA,length(bb))
        for(i in 1:length(bb)) {
        dd[i] <- dist(rbind(c(fulltheta[n+1],fulltheta[n+3]),
c(bb[i],ff[i])))
        }
        ii <- which.min(dd)
        Q <- fun.matQ.mod2(bb[ii],fulltheta[n+2],ff[ii],rown,coln,n,m)
        cholS <- update.spam.chol.NgPeyton(Rstruct,Q,...)
        r1 <- n * m * log(2 * pi) - 2 *
c(determinant.spam.chol.NgPeyton(cholS)$modulus) + sum(resid*(Q%*%(resid)))
        return((dd[ii]*10)+r1)
      }
    }
    return(optim(c(mu1,b,c,f), neg2loglikelihood, method = "L-BFGS-B"
    ,lower=c(rep(-1,n),1e-5,1e-5,1e5),upper=c(rep(5,n),1.29,1000,1.9)))
}
```

Spatial Test under H1

```
test.H1 <- function(y,mu1,a,tb,b,c,f,rown,coln, n=coln*rown, m=nrow(y),
Rstruct=NULL,...) {
    f.b <- function(b) {
    -2.110491*(b^4)+4.975194*(b^3)-4.548725*(b^2)+0.642487*b + 1.94
    }

    if (!is(Rstruct, "spam.chol.NgPeyton")) {
      Q <- fun.matQ.mod2(b,c,f,rown,coln,n,m)
      if (!is.spam(Q))
      stop("'Covariance' should return a spam object.")
      Rstruct <- chol.spam(Q,...)
    }

    neg2loglikelihood <- function(fulltheta,...) {
      if(fulltheta[n+3] < f.b(fulltheta[n+1])) {

      resid1 <- t(y[1:tb,])-fulltheta[1:n]
      mu2 <- fulltheta[1:n]+fulltheta[(n+4)]
      resid2 <- t(y[(tb+1):m,])-mu2
      resid <- c(cbind(resid1,resid2))
      Q <- fun.matQ.mod2(fulltheta[n+1],fulltheta[n+2],fulltheta[n+3],
rown,coln,n,m)
      cholS <- update.spam.chol.NgPeyton(Rstruct,Q,...)

      return(n * m * log(2 * pi) - 2 *
c(determinant.spam.chol.NgPeyton(cholS)$modulus) +
sum(resid*(Q%*%(resid))))

      }
```

```
      else {
        resid1 <- t(y[1:tb,])-fulltheta[1:n]
        mu2 <- fulltheta[1:n]+fulltheta[(n+4)]
        resid2 <- t(y[(tb+1):m,])-mu2
        resid <- c(cbind(resid1,resid2))
        bb <-  seq(0,1.29,by=0.01)
        ff <- f.b(bb)
        dd <- rep(NA,length(bb))
        for(i in 1:length(bb)) {
        dd[i] <- dist(rbind(c(fulltheta[n+1],fulltheta[n+3]),
        c(bb[i],ff[i])))
        }
        ii <- which.min(dd)
        Q <- fun.matQ.mod2(bb[ii],fulltheta[n+2],ff[ii],rown,coln,n,m)
        cholS <- update.spam.chol.NgPeyton(Rstruct,Q,...)
        r1 <- n * m * log(2 * pi) - 2 *
      c(determinant.spam.chol.NgPeyton(cholS)$modulus) +
      sum(resid*(Q%*%(resid)))
       return((dd[ii]*10)+r1)

     }
   }
   return(optim(c(mu1,b,c,f,a), neg2loglikelihood, method = "L-BFGS-B"
   ,lower=c(rep(-1,n),1e-5,1,1e-5,-2),upper=c(rep(5,n),1.29,1000,1.9,2)
,control=list(maxit=200)))
}
```

Data Simulation

```
sim.data <- function(mu0,b,c,f,rown,coln,m,...) {
    # m: number of timepoints
    mu <- rep(mu0,m)
    Q <- fun.matQ.mod2(b,c,f,rown,coln,n=rown*coln,m)
    return( t(array(rmvnorm.prec(1,mu=mu,Q=Q,...),c(rown*coln,m))))
}
```

9.3.3 Model 3

Precision matrix

```
fun.matQ.mod3 <- function(b,c,f,rown,coln,n,m){
#n number of pixels: n <- rown*coln
#m number of points in time
#b,f parameters of spatial and temporal precision matrix
#c parameter of precision matrix

matB <- matrix(0,nrow=coln*rown,ncol=rown*coln) # Matrix B

# vectorized version
rxc <- rown*coln

# 1D kernel of 4 spatial corner points centered at position 0
krow <- rep(c(-1,0,0,1),times=rxc)
kcol <- rep(c(0,-1,1,0),times=rxc)

# 1D index of rows and columns
irow <- rep(rep(seq(1:rown),times=coln),each=4)
icol <- rep(rep(seq(1:coln),each=rown),each=4)

rtmp <- irow + krow
ctmp <- icol + kcol
```

```
idx <- which ((ctmp >= 1) & (ctmp <= coln) & (rtmp >= 1) & (rtmp <= rown))

r2 <- irow[idx] + (icol[idx] - 1) * rown
c2 <- rtmp[idx]  + (ctmp[idx] - 1) * rown

matB[r2 + (c2-1) * rxc] <- b

matC <- matrix(0,m,m) # Matrix C for Kronecker product
# vectorized version
idx <- seq(1:(m-1))
matC[idx + idx*m] <- 1
matC[idx + 1 + (idx-1)*m] <- 1

temp <- kronecker(diag.spam(m),-as.spam(matB))-
kronecker(as.spam(matC),(diag.spam(n)*f))    #  I %x%  -B + C %x% -f*I    ###
add as.spam
tmp <- diff(temp@rowpointers)
temp@entries <-
temp@entries*tmp[rep(1:(n*m),tmp)]^.5*tmp[temp@colindices]^.5
diag(temp) <- tmp

return( (temp)*c)
}

return(optim(c(mu1,b,c,f,a), neg2loglikelihood, method = "L-BFGS-B",
               lower=c(rep(-1,n),1e-5,1,1e-5,-
2),upper=c(rep(25,n),0.29,1000,0.49,2,control=list(reltol=1e-4))))
}
```

Spatial Test under H0

```
test.H0 <-
function(y,mu1,b,c,f,rown,coln,n=coln*rown,m=nrow(y),Rstruct=NULL,...) {
    f.b <- function(b) {
    0.49-(0.5/0.29)*b
    }

    if (!is(Rstruct, "spam.chol.NgPeyton")) {
      Q <- fun.matQ.mod3(b,c,f,rown,coln,n,m)
      if (!is.spam(Q))
      stop("'Covariance' should return a spam object.")
      Rstruct <- chol.spam(Q,...)
    }

    neg2loglikelihood <- function(fulltheta,...) {
      if(fulltheta[n+3] < f.b(fulltheta[n+1])) {
      resid <- c(t(y)-fulltheta[1:n])
      Q <-
fun.matQ.mod3(fulltheta[n+1],fulltheta[n+2],fulltheta[n+3],rown,coln,n,m)
      cholS <- update.spam.chol.NgPeyton(Rstruct,Q,...)



      return(n * m * log(2 * pi) - 2 *
c(determinant.spam.chol.NgPeyton(cholS)$modulus)+sum(resid*(Q%*%(resid))))

      }
      else {
       return(1e10)
      }
    }
```

```
return(optim(c(mu1,b,c,f), neg2loglikelihood, method = "L-BFGS-B",
                lower=c(rep(-5,n),1e-5,1e-5,1e-
5),upper=c(rep(25,n),0.29,1000,0.49,control=list(reltol=1e-4))))

}
```

Spatial Test under H1

```
test.H1 <-
function(y,mu1,a,tb,b,c,f,rown,coln,n=coln*rown,m=nrow(y),Rstruct=NULL,...)
{
    f.b <- function(b) {
    0.49-(0.5/0.29)*b
    }

    if (!is(Rstruct, "spam.chol.NgPeyton")) {
      Q <- fun.matQ.mod3(b,c,f,rown,coln,n,m)
      if (!is.spam(Q))
      stop("'Covariance' should return a spam object.")
      Rstruct <- chol.spam(Q,...)
    }

    neg2loglikelihood <- function(fulltheta,...) {
      if(fulltheta[n+3] <     f.b(fulltheta[n+1])) {
      resid1 <- t(y[1:tb,])-fulltheta[1:n]
      mu2 <- fulltheta[1:n]+fulltheta[(n+4)]
      resid2 <- t(y[(tb+1):m,])-mu2
      resid <- c(cbind(resid1,resid2))
      Q <-
fun.matQ.mod3(fulltheta[n+1],fulltheta[n+2],fulltheta[n+3],rown,coln,n,m)
      cholS <- update.spam.chol.NgPeyton(Rstruct,Q,...)

      return(n * m * log(2 * pi) - 2 *
c(determinant.spam.chol.NgPeyton(cholS)$modulus)+sum(resid*(Q%*%(resid))))

      }
      else {
      return(1e10)
      }
    }

    return(optim(c(mu1,b,c,f,a), neg2loglikelihood, method = "L-BFGS-B",
                lower=c(rep(-1,n),1e-5,1,1e-5,-
2),upper=c(rep(25,n),0.29,1000,0.49,2,control=list(reltol=1e-4))))
}
```

Data Simulation

```
sim.data <- function(mu0,b,c,f,rown,coln,m,...) {
    # m: number of timepoints
    mu <- rep(mu0,m)
    Q <- fun.matQ.mod3(b,c,f,rown,coln,n=rown*coln,m)
    return( t(array(rmvnorm.prec(1,mu=mu,Q=Q,...),c(rown*coln,m))))
}
Pacific / North American Oscillation
```

9.4 Pacific/North American Oscillation

9.4.1 Overview

The PNA teleconnection pattern is a prominent climate feature of low-frequency variability in the Northern Hemisphere and consists of anomalies in the geopotential height fields over the western and eastern United States. It is usually described through the geopotential height at 500mb (for cold air mass the height is typically lower and for warm air masses it is higher). The positive phase is characterized by above-average geopotential heights over the western U.S. and Canada and below-average geopotential heights over the south-eastern U.S. and in the south of the Aleutian State (State Climate Office of North Carolina, 2011). This situation and the corresponding sea surface temperatures are shown in Figure 9.1.

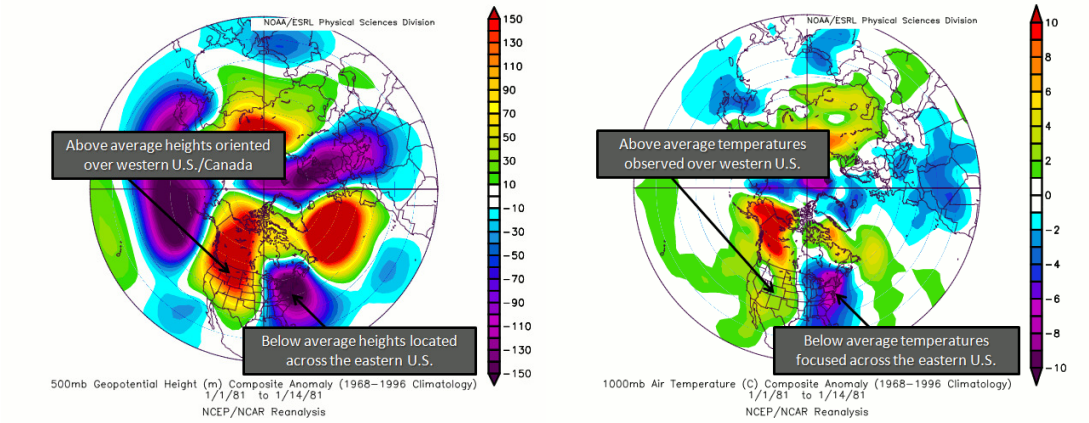

Figure 9.1: Positive phase of PNA (State Climate Office of North Carolina, 2011)

There are above-average geopotential heights over the western U.S. and Canada and below-average geopotential heights over the south-eastern U.S.

During the negative phase, low geopotential heights are observed over the western United States and higher geopotential heights over the south-eastern United States. This is again presented with the sea surface temperatures in Figure 9.2 (State Climate Office of North Carolina, 2011).

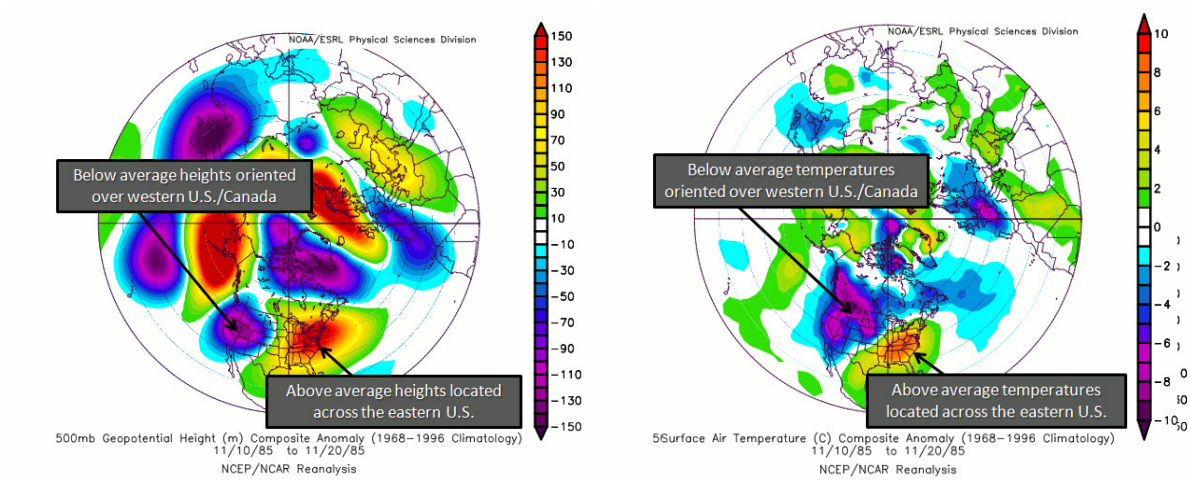

Figure 9.2: Negative phase of PNA (State Climate Office of North Carolina, 2011)

There are above-average geopotential heights over the south-eastern U.S and below-average geopotenial heights over the western United States.

The PNA is influenced by the ENSO phenomenon. During El Niño the positive PNA phase is more distinct and La Niña is associated with the negative phase of the PNA (Climate Prediction Center Internet Team, 2011).

9.4.2 Methods

The PNA Index was taken from NOAA (Climate Prediction Center Internet Team, 2011). The analyses were done on the basis of monthly indexes. Again the course of the PNA Index from 1983 to 2005 is shown in Figure 9.3.

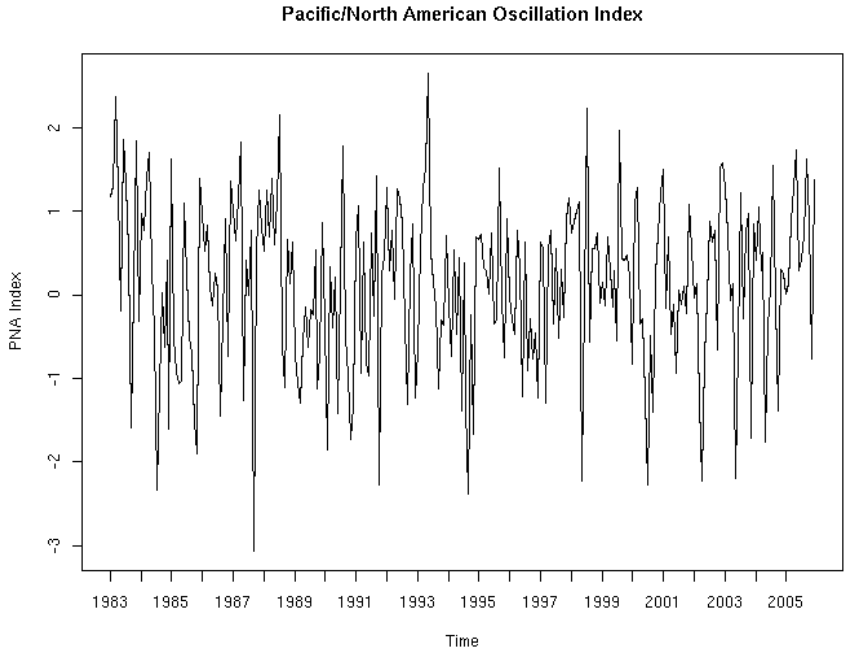

Figure 9.3: Pacific North American Oscillation Index

Course of the PNA Index between 1983 and 2005.

For the first analysis, where one extreme positive and one extreme negative PNA event were compared, the months from December to February were taken because the PNA pattern is most expansive in winter.

Although the PNA is located in the northern Pacific and does not have a great influence on the weather in Europe and Africa, a short overview of the found patterns is given. The analyses are less detailed than for ENSO and the NAO.

9.4.3 Results

As for the other two oscillations, the deseasonalized SIS and the deseasonalized cloud index are plotted in an extreme positive (2003) and extreme negative (1989) PNA winter (Figure 9.4). Winter months were taken, because then the PNA, similar to the NAO, is most pronounced. Differences between the two years were detectable at different locations of the visible disc. Even over Europe, SIS and cloud index behaved inversely during the positive and negative PNA phase. Further, over the western Atlantic and over South America, patterns were found. Over Africa, the relation was less clear.

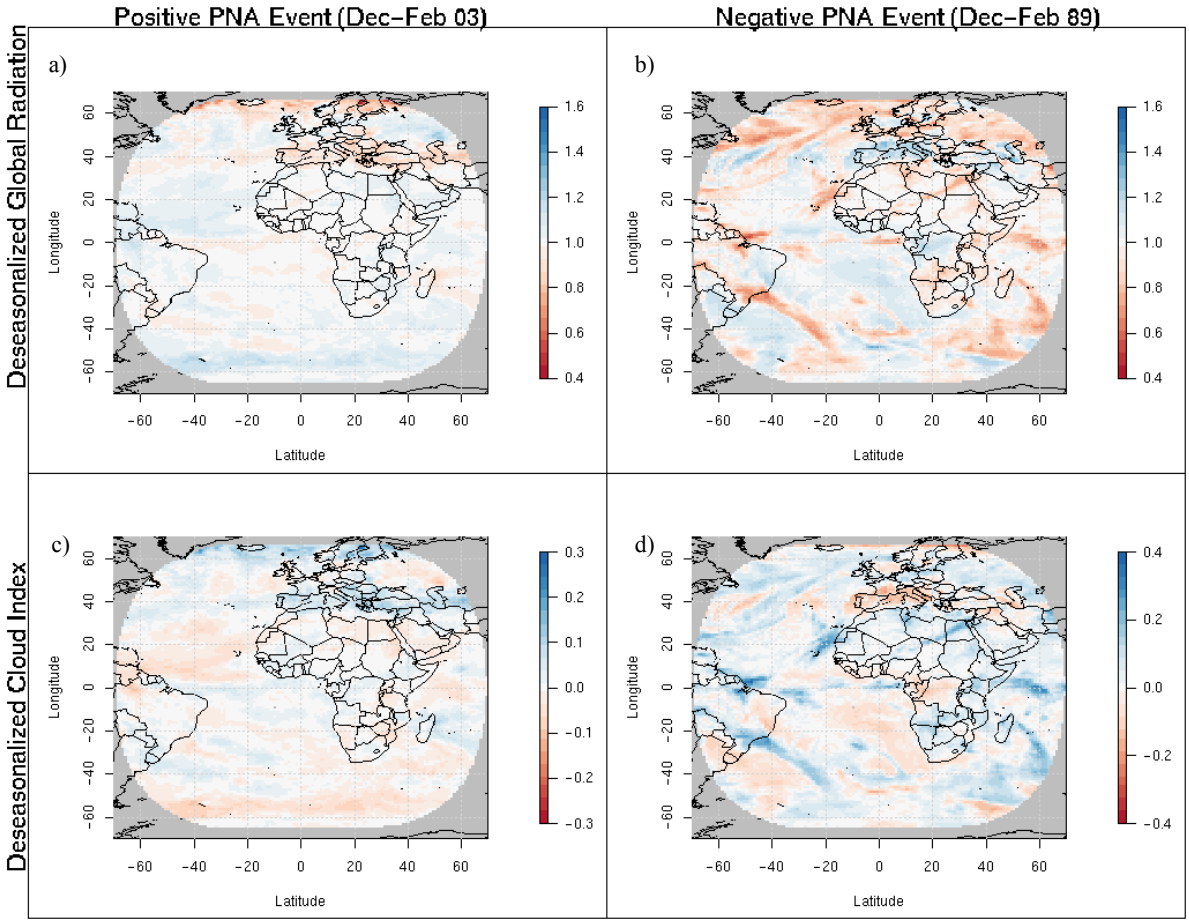

Figure 9.4: Deseasonalized SIS and deseasonalized CI for a typical positive and negative PNA Event

a) Deseasonalized SIS at a positive PNA event. b) Deseasonalized SIS at a negative PNA event.
c) Deseasonalized cloud index at a positive PNA event. d) Deseasonalized cloud index at a negative PNA event.

In Figure 9.5, the significant correlation over the whole time period between the PNA Index and the deseasonalized SIS as well as the deseasonalized cloud index is plotted.

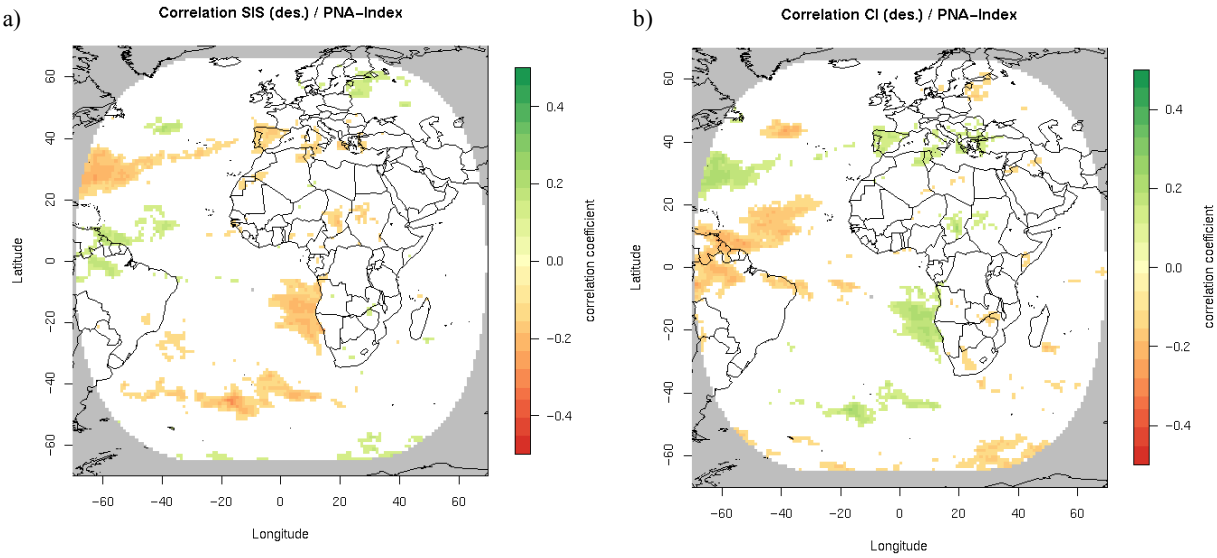

Figure 9.5: Correlation of deseasonalized SIS and deseasonalized CI with PNA Index

a) Correlation between deseasonalized SIS and PNA Index.
b) Correlation between deseasonalized cloud index and PNA Index.
Only significant correlations are presented.

It can be seen that the PNA has much less influence on the visible disc of Meteosat than the other two oscillations. However, in the southeast of Brazil, in the northern and southern Atlantic similar patterns as for the ENSO were found.

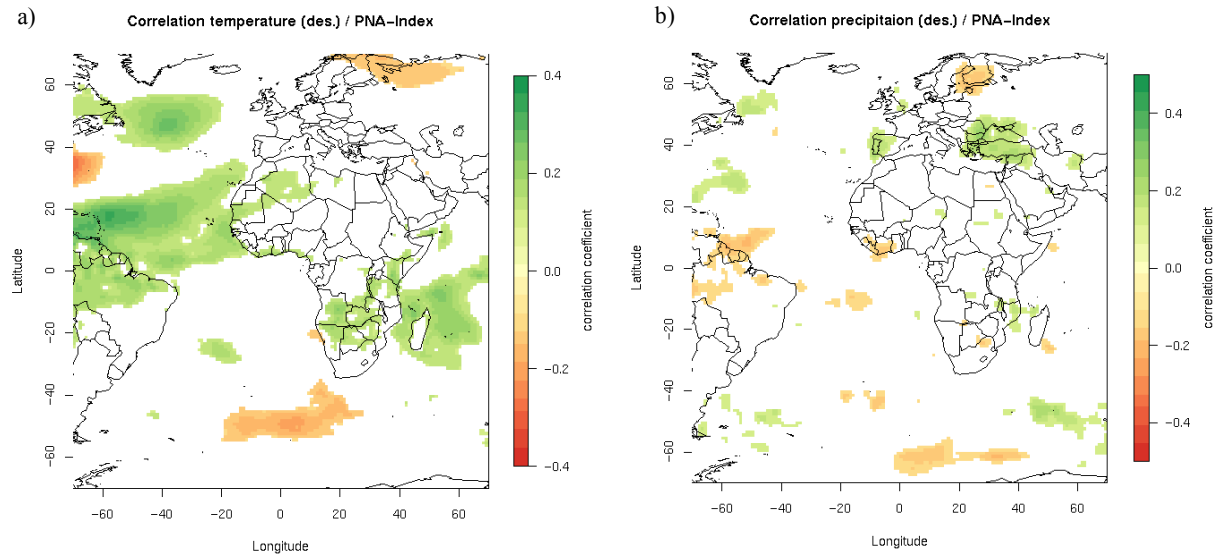

Figure 9.6: Correlation of deseasonalized temperature and deseasonalized precipitation with PNA Index

a) Correlation between deseasonalized temperature and PNA Index
b) Correlation between deseasonalized precipitation and PNA Index
Only significant correlations are presented.

The correlation between the deseasonalized precipitation and the PNA Index (Figure 9.6) was very similar to the cloud index plot. In contrast, the temperature showed more distinct patterns, especially over the Atlantic between 0-20°N and between 40-60°N.

9.4.4 Discussion

Within the visible disc of Meteosat only few patterns have been detected. As the PNA is located over the northern Pacific, it is not surprising that few significant correlations were found. The PNA affects the weather mostly in western Canada, in the western United States, and the in south-central and south-eastern U.S (Climate Prediction Center Internet Team, 2011).

Several studies have been conducted in order to investigate the influence of the PNA on the weather in North America (e.g. Feng et al., 2011). To my best knowledge, over Europe, Africa and the Atlantic little is known concerning the relation between the PNA and weather conditions. However, in the south of Brazil and at few locations over the Atlantic, significant correlations between the PNA Index and SIS or cloud index were detected in this study. Reason for these patterns is the link between PNA and ENSO (Kiladis and Mo, 1998). More exactly, the PNA is related to changes in the tropical Pacific sea surface temperatures associated with ENSO. Hence, convection in the tropics also influences higher latitudes. According to Kiladis and Mo (1998) the PNA pattern can be seen as the extra tropical arm of ENSO. This is confirmed by the patterns found in this study. The same patterns over the north Atlantic, the south Atlantic and in the south of Brazil were found for ENSO and PNA.

9.5 Climate analyses for ENSO

9.5.1 Pattern 1

Pattern 1 is located in the northern Atlantic. Figure 9.7 shows the differences of the cloud index, SIS, precipitation and temperature between the positive, neutral and negative phase of ENSO. Note that all variables are deseasonalized. As expected from Figure 5.6, cloud index and precipitation were higher during El Niño and lower during La Niña while both SIS and temperature were low during negative phases of ENSO and high during positive phases.

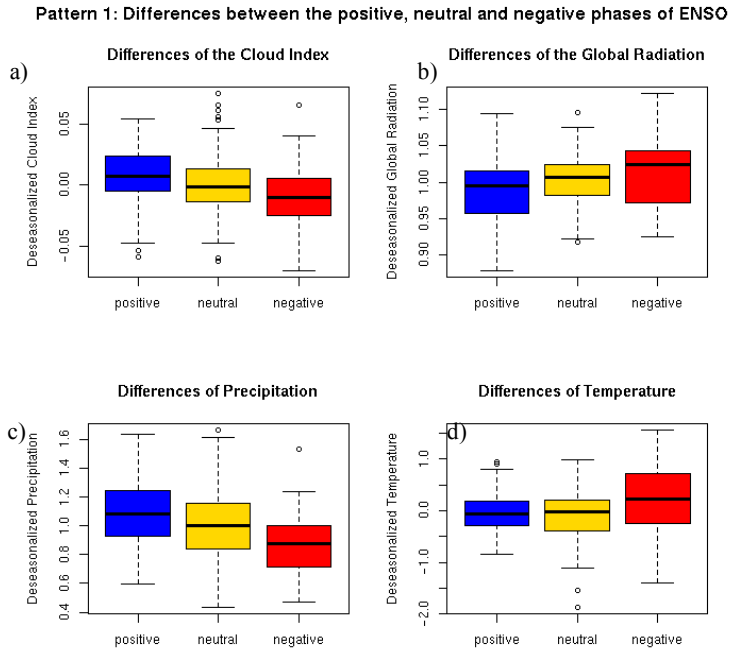

Figure 9.7: Differences between positive, neutral and negative phases of ENSO for pattern 1

a) Differences of deseasonalized cloud index. b) Differences of deseasonalized SIS.
c) Differences of deseasonalized precipitation. d) Differences of deseasonalized temperature.

Table 9.2 shows the means for each variable as well as the result of the ANOVA and the pairwise comparisons.

All four variables had significant differences in the mean for the three phases. The significance mainly occurred from the difference of the negative phase to the other two phases. El Niño phases were for no variable significantly different from the neutral phases.

Pattern 1		Cloud Index	Global Radiation	Precipitation	Temperature
Means	Mean pos	0.01	0.99	1.08	-0.04
	Mean neut	0.0005	1.00	1.01	-0.07
	Mean neg	-0.01	1.01	0.88	0.20
	Global F value	10.389***	14.98***	26.933***	7.0953**
Pairwise tests	Pos/neut	n.s.	n.s.	n.s.	n.s.
	Pos/neg	***	***	***	**
	Neut/neg	**	n.s.	**	**

Table 9.2: Descriptives of pattern 1

N_{pos}=85, N_{neut}=130, N_{neg}=61, * p<.05, ** p<.01, *** p<.001

In addition, a specific time period with an extreme El Niño and an extreme La Niña and a neutral year were investigated. Here, absolute values were taken, as the course of one year from June to May is analyzed.

The differences of the three phases were not as distinct as in the Figure above. However, it can be seen that the cloud index and precipitation were lower during La Niña, especially during the strongest La Niña months from September to November the difference to the other two phases was quite pronounced. The largest difference was found for precipitation. In average, precipitation between September and November amounted to 3.78 mm/h during the neutral phase and 2.96 mm/h during La Niña, which is a reduction of 22.5%. SIS reaches higher values between September and November during La Niña but no deviation was visible for temperature even during the strong phase of La Niña.

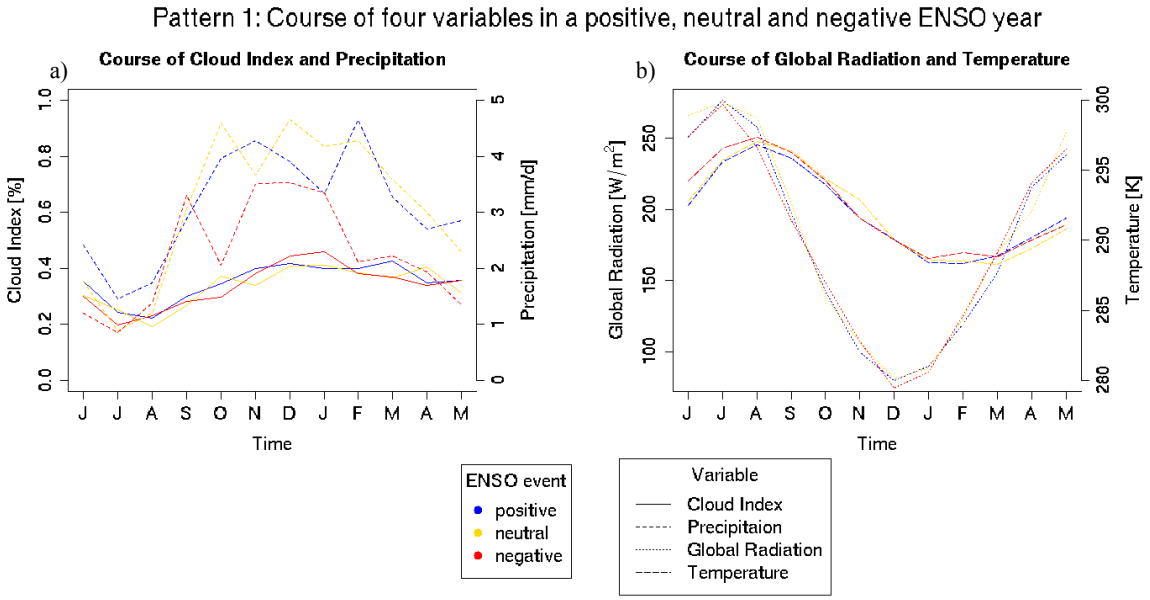

Figure 9.8: Specific positive, neutral and negative ENSO year for pattern 1

a) Course of absolute cloud index and precipitation in a positive (97/98), neutral (96/97) and negative (88/89) ENSO year.
b) Course of absolute SIS and temperature in a positive (97/98), neutral (96/97) and negative (88/89) ENSO year.

These outcomes underline the results from the pairwise t-tests above: it is primarily the negative phase of ENSO that caused different weather conditions while the neutral and positive phase were quite similar.

In summary, the region in pattern 1 was characterized by a high cloud index and a low SIS during El Niño and a low cloud index and a high SIS during La Niña. The negative ENSO was much more distinct than the positive.

9.5.2 Pattern 2

Pattern 2 is situated in the northeast of Brazil and was characterized by a positive correlation between SIS and ENSO Index and a negative correlation between cloud index and ENSO Index. There were fewer clouds and thus more radiation reaching the earth's surface during El Niño phases and the opposite happened during La Niña phases. This can be seen in Figure 5.6 as well as in Figure 9.9. Also, precipitation and temperature behaved as expected; they corresponded well to the cloud index and to SIS, respectively.

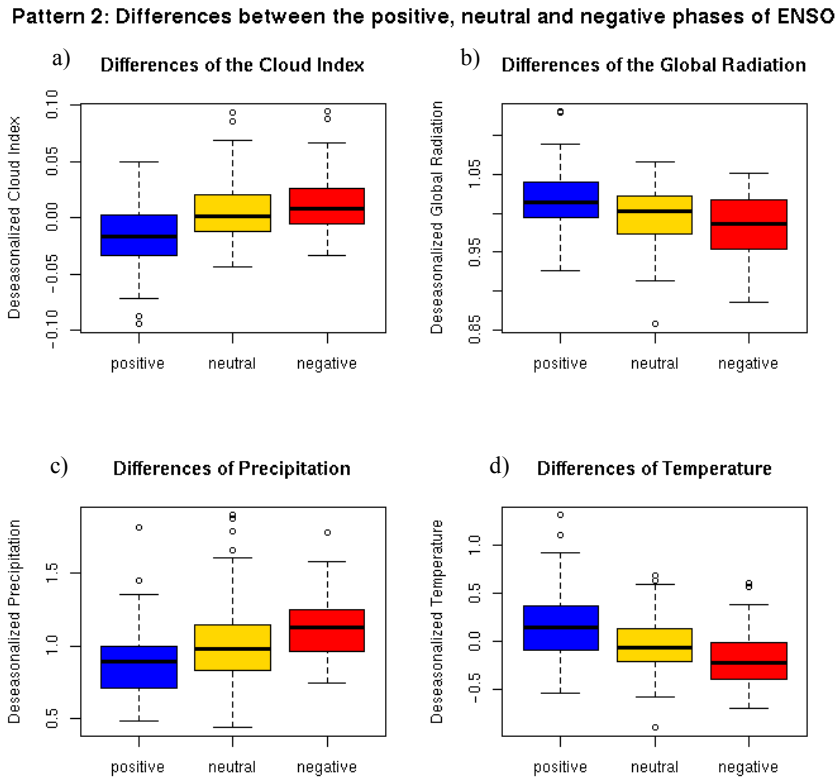

Figure 9.9: Differences between positive, neutral and negative phases of ENSO for pattern 2

a) Differences of deseasonalized cloud index. b) Differences of deseasonalized SIS.
c) Differences of deseasonalized precipitation. d) Differences of deseasonalized temperature.

For all four variables significant differences were found (Table 9.3). The means for each phase and each variable as well as the results from the pairwise comparison are listed too.

There was only a slightly significant difference or no difference between the neutral and negative phase of ENSO. On the other hand, the positive phase (El Niño) caused quite different weather conditions compared to the neutral and negative phase in the region of pattern 2. These differences were significant for all 4 variables.

Pattern 2		Cloud Index	Global Radiation	Precipitation	Temperature
Means	Mean pos	-0.0156	1.0165	0.8811	0.179
	Mean neut	0.0044	0.9968	1.0218	-0.0263
	Mean neg	0.0123	0.9838	1.1192	-0.1933
	Global F value	23.625***	30.22***	34.287***	52.946***
Pairwise tests	Pos/neut	***	***	***	***
	Pos/neg	***	***	***	***
	Neut/neg	n.s.	n.s.	*	**

Table 9.3: Descriptives of pattern 2

N_{pos}=85, N_{neut}=130, N_{neg}=61, * p<.05, ** p<.01, *** p<.001

All four variables showed differences between the positive (97/98), neutral (96/97) and negative (88/89) year (Figure 9.10). Both, cloud index and SIS during the neutral phase, were almost

everywhere between the respective values of the negative and positive phase. Over the whole time period, precipitation was 1.86 mm/h or 50.61 % higher during La Niña than during El Niño. The cloud index amounted 0.22 during El Niño and 0.29 during La Niña, which was an increase of 32%. Great differences were also found for SIS. It was on average 246.8 W/m^2 and 222.4 W/m^2 for El Niño and La Niña, respectively. This was a decrease of 10% for the La Niña year in comparison with the El Niño year. The temperature was 1° Kelvin (or 0.33%) lower in the La Niña year compared to the El Niño year.

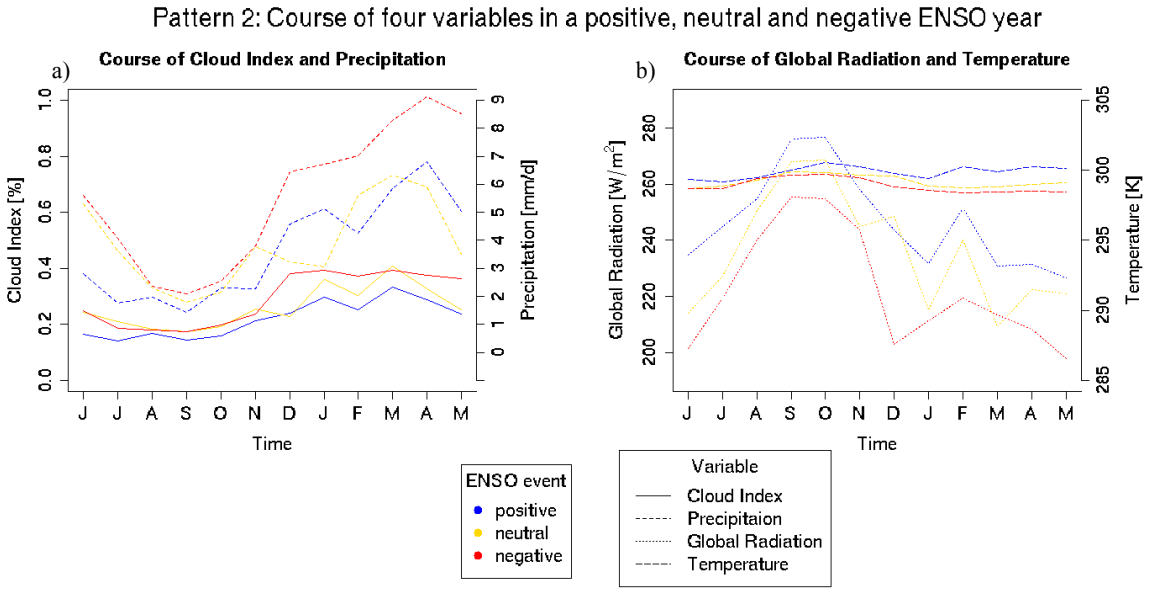

Figure 9.10: Specific positive, neutral and negative ENSO year for pattern 2

a) Course of absolute cloud index and precipitation in a positive (97/98), neutral (96/97) and negative (88/89) ENSO year.
b) Course of absolute SIS and temperature in a positive (97/98), neutral (96/97) and negative (88/89) ENSO year.

Thus, the region in the north-eastern Brazil showed very clear patterns for the three phases of ENSO. Differences were identifiable for all four variables. Especially, SIS is characterized by very distinct anomalies in the years 97/98, 96/97 and 88/89.

9.5.3 Pattern 3

Pattern 3 corresponds to the region located in south-eastern Brazil. As in pattern 1, this region was characterized by low values of SIS and high values of the cloud index during El Niño and high values of SIS and low values of the cloud index during La Niña phases. A first glance at Figure 9.11 shows that cloud index, SIS as well as precipitation were different whereas temperature didn't seem to differ during the three phases of ENSO.

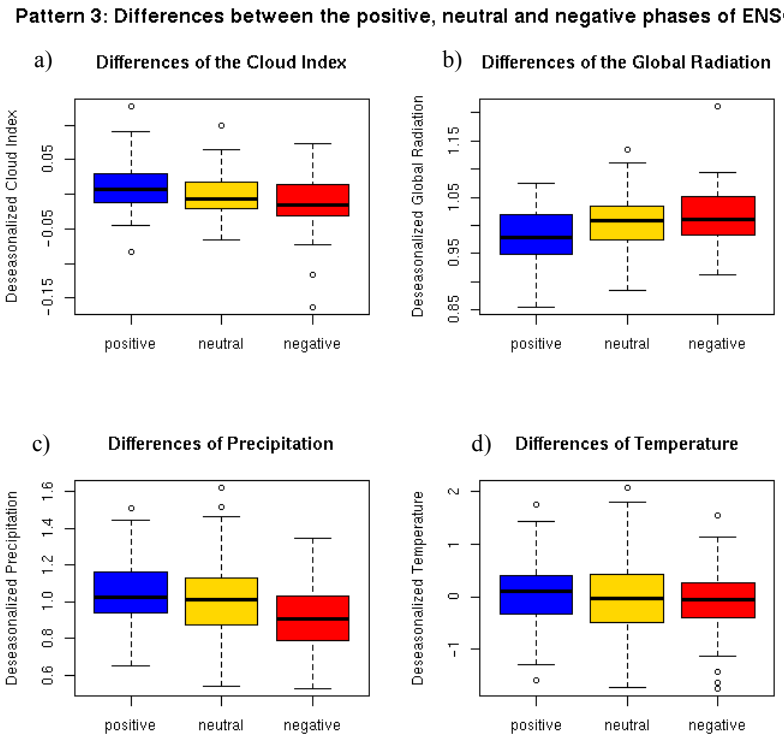

Figure 9.11: Differences between positive, neutral and negative phases of ENSO for pattern 3

a) Differences of deseasonalized cloud index. b) Differences of deseasonalized SIS.
c) Differences of deseasonalized precipitation. d) Differences of deseasonalized temperature.

The differences are significant for the cloud index, SIS and precipitation. Particularly, the pairwise test showed significant results for the difference of the positive and negative phase.

Pattern 3		Cloud Index	Global Radiation	Precipitation	Temperature
Means	Mean pos	0.0119	0.9803	1.0575	0.0915
	Mean neut	-0.0022	1.006	1.0032	-0.0099
	Mean neg	-0.0119	1.0147	0.9129	-0.1063
	Global F value	19.752***	20.162***	19.044***	3.2034
Pairwise tests	Pos/neut	**	***	n.s.	n.s.
	Pos/neg	***	***	***	n.s.
	Neut/neg	n.s.	n.s.	**	n.s.

Table 9.4: Descriptives of pattern 3

N_{pos}=85, N_{neut}=130, N_{neg}=61, * p<.05, ** p<.01, *** p<.001

By comparing again the three years, very similar results were obtained for the cloud index and precipitation (Figure 9.12). Over the whole considered time period the cloud index is in average 0.065 or 19% higher during El Niño and 0.019 or 5.6% lower during La Niña year than in the neutral years. The corresponding numbers for the precipitation are: increase of 0.320 mm/h or 8% during El Niño and decrease of 0.749 mm/h or 19% during La Niña.

SIS showed a very clear anomaly for the La Niña phase, especially between September and December. Over the whole time period, SIS was 1.929 W/m^2 or 1 % higher during El Niño and 15.166 W/m^2 or 8% lower during La Niña.

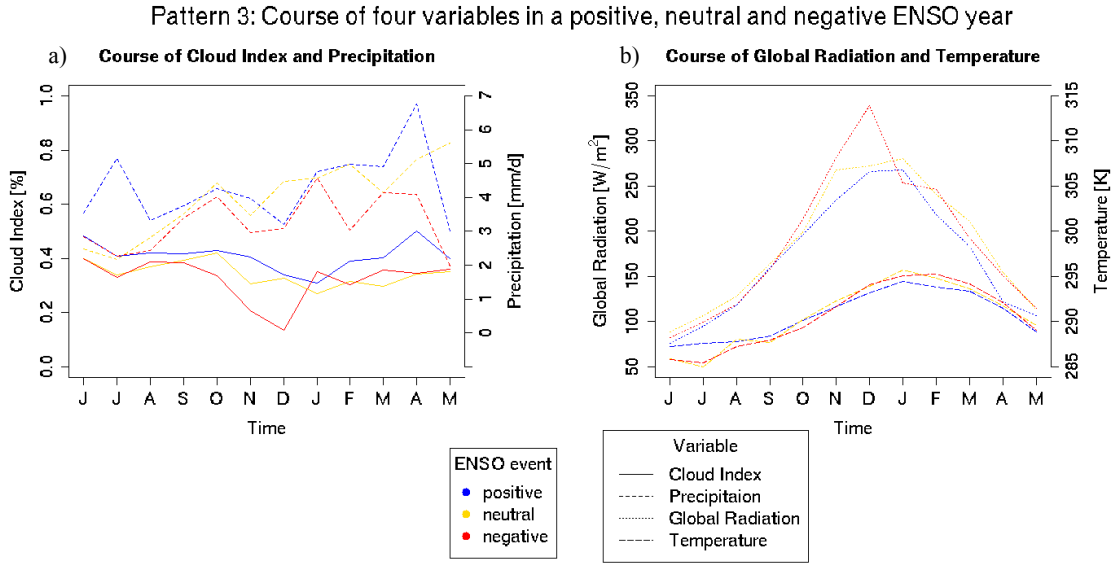

Figure 9.12: Specific positive, neutral and negative ENSO year for pattern 3

a) Course of absolute cloud index and precipitation in a positive (97/98), neutral (96/97) and negative (88/89) ENSO year.
b) Course of absolute SIS and temperature in a positive (97/98), neutral (96/97) and negative (88/89) ENSO year.

In general, there was a negative correlation between SIS and the ENSO and a positive correlation between the cloud index and the ENSO. Significant differences for pattern 3 were obtained for the cloud index, SIS and precipitation while no significant results were achieved for temperature.

9.5.4 Pattern 5

The trends for pattern 5 which is located in southern Africa was again quite clear (Figure 9.13). During El Niño's less cloudiness and less precipitation was observable; on the other hand more SIS reached the surface. Also the differences in temperature were very remarkable.

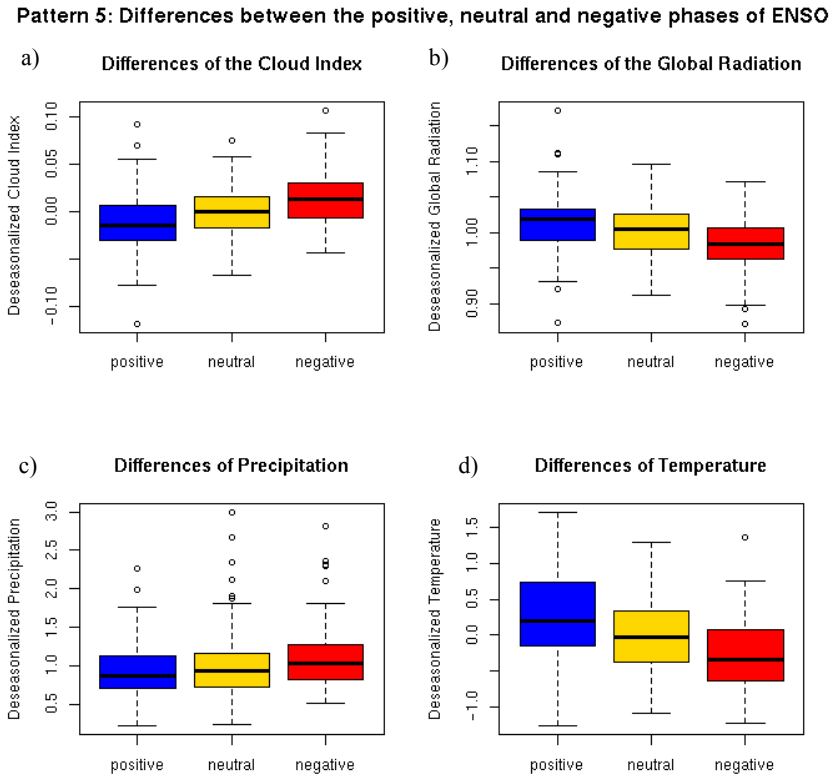

Figure 9.13: Differences between positive, neutral and negative phases of ENSO for pattern 5

a) Differences of deseasonalized cloud index. b) Differences of deseasonalized SIS.
c) Differences of deseasonalized precipitation. d) Differences of deseasonalized temperature.

Table 9.5 shows that for all variables the differences between the three phases were significant. Positive and neutral phases were more similar as the neutral and negative phases. As expected from Figure 9.13, the temperature had the highest F-value.

Pattern 5		Cloud Index	Global Radiation	Precipitation	Temperature
Means	Mean pos	-0.0105	1.0126	0.9310	0.2269
	Mean neut	0.0002	1.0004	0.9769	-0.0163
	Mean neg	0.0142	0.9817	1.1453	-0.2814
	Global F value	25.102***	22.001***	8.1732**	31.491***
Pairwise tests	Pos/neut	*	n.s.	n.s.	**
	Pos/neg	***	***	**	***
	Neut/neg	**	**	*	**

Table 9.5: Descriptives of pattern 5

N_{pos}=85, N_{neut}=130, N_{neg}=61, * p<.05, ** p<.01, *** p<.001

For the selected El Niño and La Niña years the same trends were seen. In the years 97/98 (El Niño) the cloud index amounted 0.187 and in the years 88/89 (La Niña) 0.203. This was an increase of 8%. The precipitation was on average 2.21 mm/h in the year 97/98 and 2.53 in the year 88/89, which corresponds to 15% more precipitation during the La Niña year. SIS decreased by 1.8% and temperature by 0.3% during La Niña.

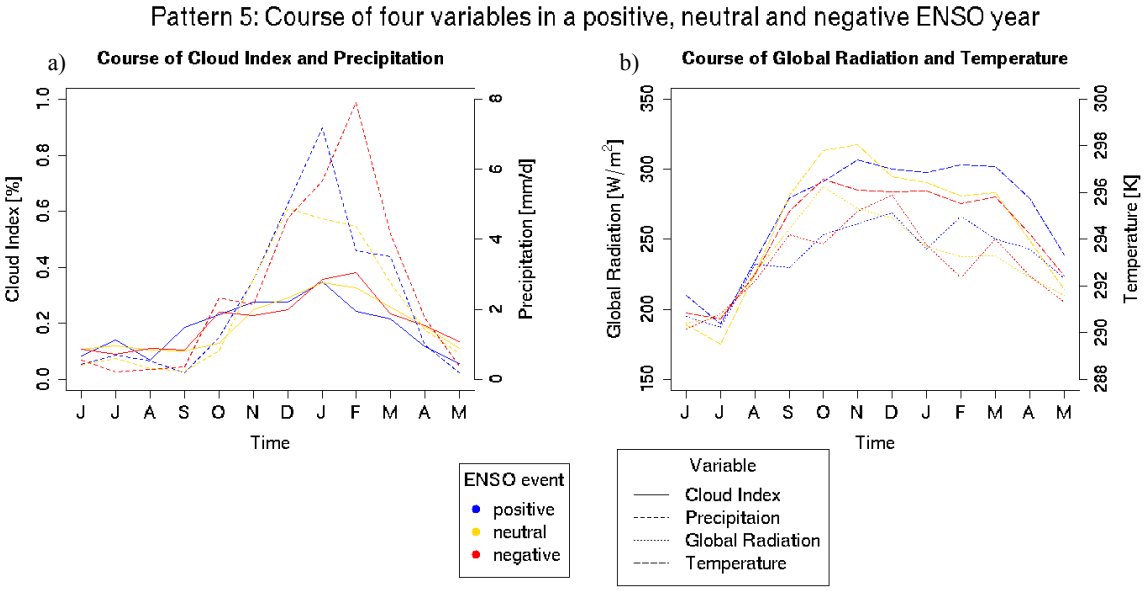

Figure 9.14: Specific positive, neutral and negative ENSO year for pattern 5

a) Course of absolute cloud index and precipitation in a positive (97/98), neutral (96/97) and negative (88/89) ENSO year.
b) Course of absolute SIS and temperature in a positive (97/98), neutral (96/97) and negative (88/89) ENSO year.

In summary, the region in southern Africa is characterized by quite different weather condition during positive and negative phases of ENSO. The area was drier and warmer during El Niño's and was characterized by a lower cloud index and thus more solar irradiance.

Veröffentlichungen der MeteoSchweiz

87 Bischof, M: 2011, Ensemble Simulations of Convective Storms, 120pp, CHF 84.-

86 Walker, D: 2010, Cloud effects on erythemal UV radiation in a complex topography, 106pp, CHF 81.-

85 Ambühl, J: 2010, Neural interpretation of ECMWF ensemble predictions, 48pp, CHF 68.-

84 Ambühl, J: 2010, Customer oriented warning systems, 91pp, CHF 78.-

83 Ceppi, P: 2010, Spatial characteristics of gridded Swiss temperature trends: local and large-scale influences, 82pp, CHF 76.-

82 Blanc, P: 2009, Ensemble-based uncertainty prediction for deterministic 2 m temperature forecasts, 90pp, CHF 78.-

81 Erdin R: 2009, Combining rain gauge and radar measurements of a heavy precipitation event over Switzerland: Comparison of geostatistical methods and investigation of important influencing factors, 109pp, CHF 81.-

80 Buzzi M: 2008, Challenges in Operational Numerical Weather Prediction at High Resolution in Complex Terrain, 186pp, CHF 103.-

79 Nowak D: 2008, Radiation and clouds: observations and model calculations for Payerne BSRN site, 101pp, CHF 80.-

78 Arpagaus M, Rotach M, Ambrosetti P, Ament F, Appenzeller C, Bauer H-S, Bouttier F, Buzzi A, Corazza M, Davolio S, Denhard M, Dorninger M, Fontannaz L, Frick J, Fundel F, Germann U, Gorgas T, Grossi G, Hegg C, Hering A, Jaun S, Keil C, Liniger M, Marsigli C, McTaggart-Cowan R, Montani A, Mylne K, Ranzi R, Richard E, Rossa A, Santos-Muñoz D, Schär C, Seity Y, Staudinger M, Stoll M, Vogt S, Volkert H, Walser A, Wang Y, Werhahn J, Wulfmeyer V, Wunram C and Zappa M: 2009, MAP D-PHASE: Demonstrating forecast capabilities for flood events in the Alpine region. Report of the WWRP Forecast Demonstration Project D-PHASE submitted to the WWRP Scientific Steering Committee, 65pp, CHF 73.-

77 Rossa AM: 2007, MAP-NWS – an Optional EUMETNET Programme in Support of an Optimal Research Programme, 67pp, CHF 73.-

76 Baggenstos D: 2007, Probabilistic verification of operational monthly temperature forecasts, 52pp, CHF 69.-

75 Fikke S, Ronsten G, Heimo A, Kunz S, Ostrozlik M, Persson PE, Sabata J, Wareing B, Wichura B, Chum J, Laakso T, Säntti K and Makkonen L: 2007, COST 727: Atmospheric Icing on Structures Measurements and data collection on icing: State of the Art, 110pp, CHF 83.-

74 Schmutz C, Müller P und Barodte B: 2006, Potenzialabklärung für Public Private Partnership (PPP) bei MeteoSchweiz und armasuisse Immobilien, 82pp, CHF 76.-

73 Scherrer SC: 2006, Interannual climate variability in the European and Alpine region, 132pp, CHF 86.-

72 Mathis H: 2005, Impact of Realistic Greenhouse Gas Forcing on Seasonal Forecast Performance, 80pp, CHF 75.-

71 Leuenberger D: 2005, High-Resolution Radar Rainfall Assimilation: Exploratory Studies with Latent Heat Nudging, 103pp, CHF 81.-

70 Müller G und Viatte P: 2005, The Swiss Contribution to the Global Atmosphere Watch Programme – Achievements of the First Decade and Future Prospects, 112pp, CHF 83.-

69 Müller WA: 2004, Analysis and Prediction of the European Winter Climate, 115pp, CHF 34.

68 Bader S: 2004, Das Schweizer Klima im Trend: Temperatur- und Niederschlagsentwicklung seit 1864, 48pp, CHF 18.-

Frühere Veröffentlichungen und Arbeitsberichte finden sich unter
www.meteoschweiz.ch » Forschung » Publikationen

Arbeitsberichte der MeteoSchweiz

235 Weusthoff T: 2011, Weather Type Classification at MeteoSwiss - Introduction of new automatic classification schemes, 38pp, CHF 66.-

234 Hächler P, Burri K, Dürr B, Gutermann T, Neururer A, Richner H, Werner R: 2011, Der Föhnfall vom 8. Dezember 2006 – Eine Fallstudie, 47pp, CHF 68.-

233 Wüthrich C, Scherrer S, Begert M, Croci-Maspoli M, Marty C, Seiz G, Foppa N, Konzelmann T, Appenzeller C: 2010, Die langen Schneemessreihen der Schweiz - Eine basisklimatologische Netzanalyse und Bestimmung besonders wertvoller Stationen mit Messbeginn vor 1961, 33pp, CHF 64.-

232 Willi, M: 2010, Gridding of Daily Sunshine Duration by Combination of Station and Satellite Data, 92pp, CHF 78.-

231 Scherrer, S: 2010, Die Niederschlagstotalisatoren der Schweiz –Eine basisklimatologische Netzanalyse und Bestimmung besonders wertvoller Stationen, 32pp, CHF 64.-

230 Michel, D, MW Rotach, R Gehrig, R Vogt: 2010, Experimental investigation of micrometeorological influences on birch pollen emission, 37 pp, CHF 56.-

229 Philipona R, Levrat G, Romanens G, Jeannet P, Ruffieux D and Calpini B, 2009: Transition from VIZ / Sippicanto ROTRONIC - A new humidity sensor for the SWISS SRS 400 Radiosonde, 37pp, CHF 66.-

228 MeteoSchweiz: 2009, Klimabericht Kanton Graubünden, 40pp, nur als .pdf erhältlich

227 MeteoSchweiz, 2009, Basisanalysen ausgewählter klimatologischer Parameter am Standort KKWLeibstadt, 135pp, CHF 88.-

226 MeteoSchweiz, 2009, Basisanalysen ausgewählter klimatologischer Parameter am Standort KKW Mühleberg, 136pp, CHF 88.-

225 MeteoSchweiz, 2009, Basisanalysen ausgewählter klimatologischer Parameter am Standort KKW Gösgen, 136 pp, CHF 88.-

224 MeteoSchweiz, 2009, Basisanalysen ausgewählter klimatologischer Parameter am Standort KKW Beznau, 135pp, CHF 88.-

223 Dürr B: 2008, Automatisiertes Verfahren zur Bestimmung von Föhn in den Alpentälern, 22pp, CHF 62.-

222 Schmutz C, Arpagaus M, Clementi L, Frei C, Fukutome S, Germann U, Liniger M und Schacher F: 2008, Meteorologische Ereignisanalyse des Hochwassers 8. bis 9. August 2007, 29pp, CHF 64.-

221 Frei C, Germann U, Fukutome S und Liniger M: 2008, Möglichkeiten und Grenzen der Niederschlagsanalysen zum Hochwasser 2005, 19pp, CHF 62.-

220 Ambühl J: 2008, Optimization of Warning Systems based on Economic Criteria, 79pp, CHF 75.-

219 Ceppi P, Della-Marta PM and Appenzeller C: 2008, Extreme Value Analysis of Wind Observations over Switzerland, 43pp, CHF 67.-

218 MeteoSchweiz (Hrsg): 2008, Klimaszenarien für die Schweiz – Ein Statusbericht, 50pp, CHF 69.-

217 Begert M: 2008, Die Repräsentativität der Stationen im Swiss National Basic Climatological Network (Swiss NBCN), 40pp, CHF 66.-

216 Della-Marta PM, Mathis H, Frei C, Liniger MA and Appenzeller C: 2007, Extreme wind storms over Europe: Statistical Analyses of ERA-40, 80pp, CHF 75.-

Frühere Veröffentlichungen und Arbeitsberichte finden sich unter
www.meteoschweiz.ch » Forschung » Publikationen